

SCANNING EXCIMER LASER ABLATION OF POLY(ETHYLENE TEREPHTHALATE) (PET) AND ITS APPLICATION TO RAPID PROTOTYPING OF CHANNELS FOR MICROFLUIDICS

THÈSE N° 2264 (2000)

PRÉSENTÉE AU DÉPARTEMENT DE MICROTECHNIQUE

ÉCOLE POLYTECHNIQUE FÉDÉRALE DE LAUSANNE

POUR L'OBTENTION DU GRADE DE DOCTEUR ÈS SCIENCES

PAR

Frank Rüdiger WAGNER

Diplom-Physiker, Georg-August-Universität Göttingen, Allemagne
de nationalité allemande

acceptée sur proposition du jury:

Dr P. Hoffmann, directeur de thèse
Prof. P. Dyer, rapporteur
Prof. H. Girault, rapporteur
Prof. A. Wokaun, rapporteur

Lausanne, EPFL
2000

Abstract

Excimer Laser Ablation is a micro-machining method which has undergone an important breakthrough in the last twenty years. In contrast with most literature studies, dealing with Static Ablation, this PhD work focuses on the study of *Scanning Ablation* of poly(ethylene terephthalate) (PET) at 193 nm, using relatively high fluences of about 1 J/cm^2 . Here, Static Ablation means that the substrate is fixed with respect to the laser beam. In this way, the size of the machined area per set of pulses does not exceed a few mm^2 . Moving the substrate under the laser beam during the irradiation, i.e. using Scanning Ablation, enables to machine more easily and with a better quality bigger surfaces. This is particularly interesting for micro-channel prototyping in PET (typical cross-section of the channels: $40 \times 40 \mu\text{m}^2$, length: $>1.5 \text{ cm}$), which was the aimed application of this work.

The surface properties of the ablated micro fluidic channels were studied, comparing Static Ablation to Scanning Ablation with different parameters. For this purpose SEM, TEM, XPS, water condensation experiments and electroosmotic flow measurements in laminated micro-channels were carried out. The properties of the ablated surfaces were shown to be modified, in terms of chemical properties and in terms of morphology.

In order to explain the modified surface properties after Scanning Ablation, the angle between the irradiated ramp, forming under the beam, and the non irradiated surface was shown to be one key-parameter, the shape of the laser spot on the substrate being the other one.

The *chemical composition* of the ablated surfaces depends on the nature and amount of redeposited debris. There are two types of debris:

- Indirect debris, which is produced by collision of the ejected material with the ambient atmosphere. After ablation in air, this debris is hydrophilic due to the oxygen and nitrogen content. The geometry of the debris covered area, and thus the amount of indirect debris in the micro channels, depends on the geometry of the irradiated area.
- Direct debris, which is produced by a mechanism very similar to Pulsed Laser Deposition, is only possible in Scanning Ablation. It is directly ejected in the direction of the channel surface and it is less influenced by the surrounding atmosphere. Condensation experiments proved it to be more hydrophobic than indirect debris.

In Static Ablation, only indirect debris is present, and the debris affected surfaces are therefore hydrophilic. In Scanning Ablation, the amount of direct and indirect debris vary differently with the ramp angle and the shape of the irradiated spot. When increasing the ramp angle from 0° to 45° , a maximum electroosmotic flow velocity is measured around 4.3° , which is explained by a maximum of the ratio indirect / direct debris for this angle.

Electroosmotic flow velocity measurements in channels of the same width but with different depths (polyethylene laminated), combined with a numerical implementation of an analytical

ABSTRACT

formula for the flow velocity profile, enabled to calculate the ζ -potentials of the ablated the surfaces for different ramp angles and the ζ -potential of the lamination.

Besides the chemical composition, Scanning Ablation also changes the *morphology* of the ablated surfaces. At high ramp angles, the surface structure of the channel floor is determined by the direct debris redeposition leading to a nanometric roughness. The micrometric roughness, which is known to develop in stretched polymer substrates upon Laser Ablation, depends on the ramp angle ϑ during channel fabrication.

As the ramp is the only irradiated surface in scanning ablation, it was studied in detail. Three different structures were observed on ramps in stretched polymer substrates, each in one of three distinct ranges of ramp angles. On the basis of a vector decomposition of the fabrication induced stresses in the polymer, the different structures can be understood as a step wise suppression of the Static Structure formation on the ramps. The stress component normal to the irradiated surface acts as an inhibitor of the Static Structure formation. At ramp angles lower than 10° , the structure on the ramps is identical to the structure on statically ablated surfaces. At $10^\circ < \vartheta < 30^\circ$ the structure changes but is still present. At ramp angles higher than 30° the ramps are smooth.

As the micrometric structure on the channel floor is given by the structure on the lower part of the irradiated ramp, the channel floor structure is of the same type as the structure on the ramp. However, it is not possible to obtain a smooth channel floor.

The angle ranges for the different structures do not depend on the laser fluence but vary from one substrate material to another. The presence and the orientation of the micrometric structure only have negligible influence on the electroosmotic flow in the micro channels.

In conclusion, the message of this work is that Scanning Ablation modifies drastically the ablated surface properties. This must be taken into account when thinking about fabricating devices for which properties such as wettability, adhesion, ζ -potential or micro/nano-roughness are important.

Résumé

L'ablation laser est une méthode de micro-usinage qui connaît un grand essor depuis une vingtaine d'année. Contrairement à la plupart des travaux de la littérature ayant trait à l'*ablation statique* de matériaux, ce travail de thèse concerne l'étude de l'*ablation scannée* du polyéthylène téréphthalate (PET) à 193 nm, avec des fluences assez élevées (de l'ordre de 1 J/cm^2). En ablation statique, le substrat est fixe par rapport au laser, et la taille des surfaces usinées par une série de pulses successifs n'excède pas quelques mm^2 . L'ablation scannée permet elle d'usiner plus aisément des surfaces plus grandes avec une meilleure qualité, en bougeant le substrat par rapport au laser. Ceci est particulièrement intéressant pour le prototypage de micro-canaux en PET (section typique des canaux: $40 \times 40 \mu\text{m}^2$, longueur $>1.5 \text{ cm}$), qui est l'application visée pour ce travail.

Les propriétés de surfaces des canaux micro-fluidiques produits ont été étudiées, en comparant l'ablation statique et l'ablation scannée avec différents paramètres. Des mesures de SEM, TEM, XPS, des expériences de condensation d'eau et des mesures de flux électroosmotique dans des micro-canaux laminés ont été réalisées dans ce but. Il a été montré que les propriétés des surfaces ablatées sont modifiées, à la fois en termes de propriétés chimiques et en termes de morphologie.

L'angle entre la rampe irradiée (qui se forme sous le faisceau laser) et la surface non irradiée a été identifié comme l'un des paramètres clé our expliquer la modification des propriétés de surface après ablation scannée, l'autre étant la forme du spot laser sur le substrat.

La *composition chimique* des surfaces ablatées dépend de la nature et de la quantité de débris qui sont redéposés. Il existe deux types de débris:

- Les débris indirects, provenant de la collision des produits éjectés avec l'atmosphère ambiante. Pour une ablation dans l'air, ces débris sont hydrophiles car ils incorporent de l'azote et de l'oxygène. La géométrie de la surface sur laquelle ces débris se redéposent, et donc la quantité de débris indirects présents dans le micro-canal, dépend de la géométrie de la surface irradiée.
- Les débris directs, provenant d'un mécanisme similaire à la "*Pulsed Laser Deposition*" n'existent que pour l'ablation scannée. Ils sont éjectés directement dans la direction de la surface du canal et sont donc moins influencés par l'atmosphère ambiante que les débris indirects. Des expériences de condensation ont montré qu'ils sont plus hydrophobes que ces derniers.
- En ablation statique, seuls les débris indirects sont présents, rendant les surfaces où ils se redéposent hydrophiles. En ablation scannée, les quantités de débris directs et indirects varient différemment avec l'angle de la rampe et avec la forme de la surface irradiée. En augmentant l'angle de rampe de 0° à 45° , on observe un maximum pour la valeur du flux

RÉSUMÉ

électroosmotique vers 4.3° , expliqué par un maximum du rapport débris indirects/débris directs pour cet angle-là.

Des mesures de flux électroosmotique moyens dans des canaux de même largeur mais de profondeur différente (couverts d'une lamination en polyéthylène), combinées à l'implémentation numérique d'une formule analytique décrivant le profil de flux ont permis de déterminer les potentiels ζ des surfaces ablatées avec différents angles de rampe ainsi que le potentiel ζ de la lamination.

En plus de la composition chimique, l'ablation scannée modifie aussi la *morphologie* des surfaces ablatées. Pour des angles de rampe élevés, la structure de la surface des canaux est déterminée par la redéposition des débris directs, qui génèrent une rugosité nanométrique. La rugosité micrométrique, dont on sait qu'elle se développe par ablation laser dans les polymères étirés, dépend de l'angle de rampe durant la fabrication des canaux.

Etant donné que la rampe est la seule surface irradiée en ablation scannée, sa structure a été étudiée en détails. Trois différentes structures ont été observées sur les rampes dans des polymères étirés, correspondant chacune à une gamme d'angle de rampe. Les changements d'une structure à l'autre ont été expliqués par une décomposition vectorielle du stress existant dans le polymère. Il a été montré que la composante du stress normale à la surface irradiée agit comme un inhibiteur de formation de la structure statique. Pour des angles inférieurs à 10° , la structure de la rampe est identique à celle d'une surface ablatée statiquement. Pour des angles de rampes compris entre 0° et 30° , il existe toujours une structure, mais modifiée par rapport à la précédente. Pour des angles de rampe supérieurs à 30° , la rampe est lisse.

Comme la structure micrométrique du fond du canal provient de la structure de la partie inférieure de la rampe, le fond du canal à la même structure que la rampe. A la différence près que l'on ne peut pas obtenir un fond de canal lisse.

Les gammes d'angles dans lesquelles on obtient les différentes structures ne sont pas affectées par la fluence, mais varient d'un matériau à l'autre. La présence et l'orientation de la microstructure n'ont qu'une influence négligeable sur le flux électroosmotique dans les micro-canaux.

En conclusion, le message de ce travail est que l'ablation scannée et ses paramètres modifient considérablement les propriétés des surfaces ablatées. Ceci doit être impérativement pris en compte dans l'optique de la fabrication de devices pour lesquels les propriétés telles la mouillabilité, l'adhésion, le potentiel ζ , la micro-rugosité, etc. sont importantes.

Table of contents

I.	Introduction	1
II.	State of the art	3
II.1	Laser Ablation	3
II.1.1	Fundamentals.....	3
II.1.2	Problems in multiple pulse ablation	5
II.2	Surface modification	7
II.2.1	Chemical surface composition.....	7
II.2.2	Structure formation.....	9
II.3	Ablation Products	13
II.3.1	Expansion of ablation products	13
II.3.2	Redeposition of ablation products - debris formation	14
II.3.3	Surface modification by debris.....	16
II.4	Wetting of liquids on solids.....	19
II.4.1	Fundamentals.....	19
II.4.2	Inhomogeneities.....	20
II.5	Electroosmosis.....	23
II.5.1	Fundamentals.....	23
II.5.2	Applications in microfluidics	25
II.5.3	Composite channels	26
III.	Experimental	29
III.1	Laser Ablation.....	29
III.1.1	The ablation setup	29
III.1.2	Static Ablation.....	31
III.1.3	Scanning Ablation	31
III.1.4	Ramp ablation	33
III.1.5	Angle and ablation rate measurements.....	34
III.2	Surface characterization	35
III.2.1	Topography	35
III.2.2	Chemistry	36
III.3	Samples	39
III.3.1	Biaxially stretched PET samples.....	39
III.3.2	Production of uniaxially stretched PET samples.....	40
III.3.3	poly(ethylene naphthalate) samples	41
III.4	Micro fluidic channel production.....	43
III.4.1	Channel types	43
III.4.2	Channels in thin substrates	44
III.4.3	Channels in thick substrates	44
III.5	Electroosmotic flow measurements	47
III.5.1	The current monitoring method.....	47
III.5.2	Data treatment	48
IV.	Scanning Ablation versus Static Ablation	49
IV.1	The geometry of the channels	49
IV.2	Redeposition - Debris	51
IV.2.1	Redeposited debris distribution due to scanning.....	51

IV.2.2	Enhanced redeposition due to self PLD.....	52
V.	Structure changes due to Scanning Ablation	55
V.1	Static Ablation.....	55
V.1.1	Unstretched PET.....	55
V.1.2	Uniaxially stretched PET.....	56
V.1.3	Biaxially stretched PET.....	56
V.1.4	Biaxially stretched PEN.....	57
V.2	Ramp ablation and Scanning Ablation.....	59
V.2.1	Suppression of the structure formation.....	59
V.2.2	The general case.....	64
V.2.3	Material dependence of the limiting angles.....	65
V.2.4	The structure on the beginning ramp.....	67
V.3	The channel floor.....	69
V.4	The debris contribution.....	71
V.4.1	Debris in Static Ablation.....	71
V.4.2	Debris in Scanning Ablation.....	72
V.5	Chapter summary.....	75
VI.	Chemical surface composition and microfluidics	77
VI.1	Chemical composition of the ablated area.....	77
VI.1.1	Transmission Electron Microscopy.....	77
VI.1.2	X-ray Photoelectron Spectroscopy.....	79
VI.2	Interaction of debris and water.....	87
VI.2.1	Contact angle measurement in a channel.....	87
VI.2.2	Condensing experiment.....	88
VI.3	Electroosmotic flow control.....	93
VI.3.1	Experimental results.....	93
VI.3.2	Explanation of the optimum.....	97
VI.4	Zeta potential determination.....	101
VI.4.1	Experiments.....	101
VI.4.2	Electroosmotic flow in laminated channels.....	101
VI.4.3	Linking model and experiment (approximations).....	103
VI.4.4	Fit results.....	105
VI.4.5	Discussion.....	107
VI.5	Chapter summary.....	109
VII.	Conclusion and outlook	111
Appendix A: Development of the Static Structure with the number of pulses		
A.1	As observed by Static Ablation.....	115
A.2	As observed by Scanning Ablation.....	115
Appendix B: Numerical implementation of Eq. 9 and Eq. 11		
B.1	The implemented equations (approximations).....	117
B.2	Numerical tests, convergence and precision.....	118
B.3	Software.....	119

Appendix C: Linearity of Eq. 9 at constant channel cross section

C.1 Explicit form of $\text{const}_1(l_x, l_y)$ and $\text{const}_2(l_x, l_y)$ in Eq. 24.....	121
---	-----

Appendix D: List of symbols and abbreviations

D.1 Symbols used (alphabetical order)	123
D.2 Abbreviations (alphabetical order).....	126

Bibliography	127
---------------------	-----

TABLE OF CONTENTS

I. Introduction

Excimer Laser Ablation was first described in 1982 [1,2]. In the following years, the research activities in the field were rapidly growing because of the possibility to produce high quality structures of micrometric dimensions in all kinds of materials. Today, a lot of fundamental and practical knowledge is available on Laser Ablation, and it is more and more widely used in the prototyping of micro devices [3].

If the whole micro device is bigger than the laser beam area, which is determined by the necessary intensity for machining, the best solution is often to scan the substrate or the beam, in order to cover the whole micro device area. One domain of active research where such micro devices are needed, is the micro fluidics research, which should once result in the fabrication of so-called *micro-total-analysis-systems* (μ -TAS) [4]. The use of these systems would be profitable in many ways. For example, they would allow for massively parallel processing of analyses, one of the aims of the pharmacological industry, in order to manage the big number of different experiments associated with combined active substances in one medicine and also the human genome project. Another advantage of μ -TAS would be the low consumption of solvents and other reagents per analysis. Using Excimer Laser Ablation as the standard mass production method for the microfluidic chips would naturally be far too expensive. Other methods like injection molding or hot embossing are much more adapted. However, for the *rapid prototyping* of those micro channels, Excimer Laser Ablation is very advantageous because of its high flexibility compared to other methods.

The micro channels in these micro fluidic devices usually have a diameter of some tens of microns and a length of some centimeters. In order to produce them by Laser Ablation, one has to choose between step by step fabrication (static irradiation) and scanning methods (irradiation with continuous motion). Scanning methods result in higher quality of the final device, because no care needs to be taken for perfect joints between two statically produced parts of the structure. Moreover, Rossier *et al.* [5] mentioned recently a drastic increase in the hydrophilicity of ablated micro channels in poly(ethylene terephthalate) (PET) after Scanning Ablation, with respect to Static Ablation.

Hydrophilicity and other surface properties are important in these devices, because usually aqueous solutions are injected, pumped, separated and eventually analyzed by electrochemical means. Methods which allow for controlling the surface properties of the micro channels are particularly interesting, because they enable for an optimization of the final device [4,6]. Based on a *localized* control of the surface properties, one could also imagine new devices combining chromatographic with electrophoretic separation.

Hence, based on the observation of Roberts and Rossier *et al.* [3,5], and in collaboration with a research group at the Laboratory of Electrochemistry (EPFL), *the aim of this work was to find out about the particularities of Scanning Excimer Laser Ablation, concerning the surface properties of the ablated surfaces.*

I. INTRODUCTION

The experimental results can be separated into two chapters:

A first part deals with changes in surface topography, occurring upon Scanning Ablation of stretched poly(ethylene terephthalate) (PET) [7-9].

The second part is dedicated to the variations of the chemical composition of the ablated surfaces and the control of electroosmotic flow in the micro channels [10-12].

The importance of the results of the present investigation is not restricted to the field of μ -TAS prototyping. The message of this work is that both, the surface topography and the chemical composition of the ablated surfaces, are dependent on the ablation mode and the scanning ablation parameters. In consequence, anybody who is concerned about the surface properties of the ablated surfaces (wettability, adhesion, roughness, conductivity) should mention if the sample was scanned or not.

II. State of the art

II.1 Laser Ablation

Laser Ablation is localized and controlled removal of a substrate material by high light intensities. The material removal occurs only if a certain threshold in light intensity is exceeded. For the wavelength and the materials investigated in this work (poly(ethylene terephthalate) (PET) and poly(ethylene naphthalate) (PEN)), the empirical theory, based on Beer's absorption law at high intensities and the existence of an ablation threshold, gives satisfactory fits to the experimentally measured ablation rate curves as a function of the laser intensity. Some questions concerning multiple pulse ablation are subject to actual re-search and the phenomena are not yet completely understood.

II.1.1 Fundamentals

Removal of substrate material by light, without important heat induced damage in the non irradiated zones, is called *Laser Ablation* or sometimes also *Ablative Photo Decomposition (APD)*. To induce Laser Ablation, a high amount of light energy has to be deposited in a small volume of the substrate material. Because of energy transport in the substrate, especially heat diffusion, this is only possible if the energy is deposited within a short time. For the ablation of most polymers, nanosecond UV-lasers are well adapted for this purpose. When staying in the nanosecond regime for the pulse duration of the lasers, it is more convenient to speak of *fluence* instead of *intensity*. Here, *fluence* is defined as the intensity integrated over the whole pulse duration, i.e. energy per pulse per area.

The successive stages following the irradiation of a polymer substrate with intense, ultrashort UV-pulses can be imagined roughly as follows (Figure II.1-1):

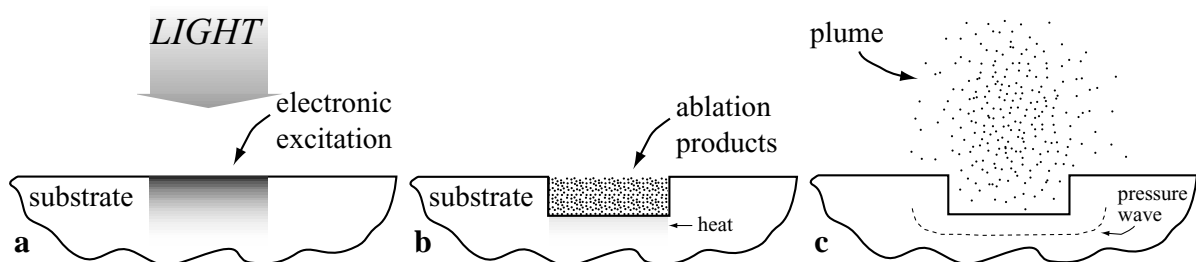


Figure II.1-1: Schematic showing the different stages of the Laser Ablation process: (a) The light is absorbed and generates electronic excitation. (b) Bond breaking took place, leaving gaseous products at high pressure. (c) The ablation products expand.

1. The *light is absorbed* in the substrate. At UV-wavelengths this leads in polymers to electronic excitation of the molecules.
2. A part of the electronic excitation relaxes, and is converted into heat. The heat induces phase changes, and finally *bond breaking*, evaporation and desorption of the resulting small molecules or atoms (“thermal” mechanism). The other part of the electronic excitation

results directly, without the generation of heat, in bond breaking, evaporation and desorption (“photonic” mechanism). The relative importance of the two possible decomposition pathways, was and is discussed controversially. Nevertheless, it is sure that the relative importance of the two decomposition mechanisms differs for different materials and wavelengths.

3. The high pressure generated by the decomposition of the substrate, causes the *removal of the ablation products*. They expand into the vacuum or the ambient atmosphere.
4. At the same time, the recoil pressure sends a *pressure wave into the substrate*.
5. If the expansion of the ablation products takes place into an ambient atmosphere, a *shock or blast wave is formed*.

If nanosecond pulses are used instead of ultrashort pulses, the removal of the ablation products begins within the duration of the laser pulse. Hence, the “plume” of ablation products absorbs light, which complicates the situation somewhat.

As mentioned, the ablation mechanism depends on the substrate material, the laser wavelength and the pulse duration, just to quote the most important parameters. Nevertheless the experimental *ablation curve*, i.e. the ablated depth per pulse h as a function of fluence Φ , shows two general features (Figure II.1-2a).

1. The existence of a threshold value in fluence Φ for ablation to occur (Φ_0).
2. The ablation rate h increases with increasing fluence Φ .

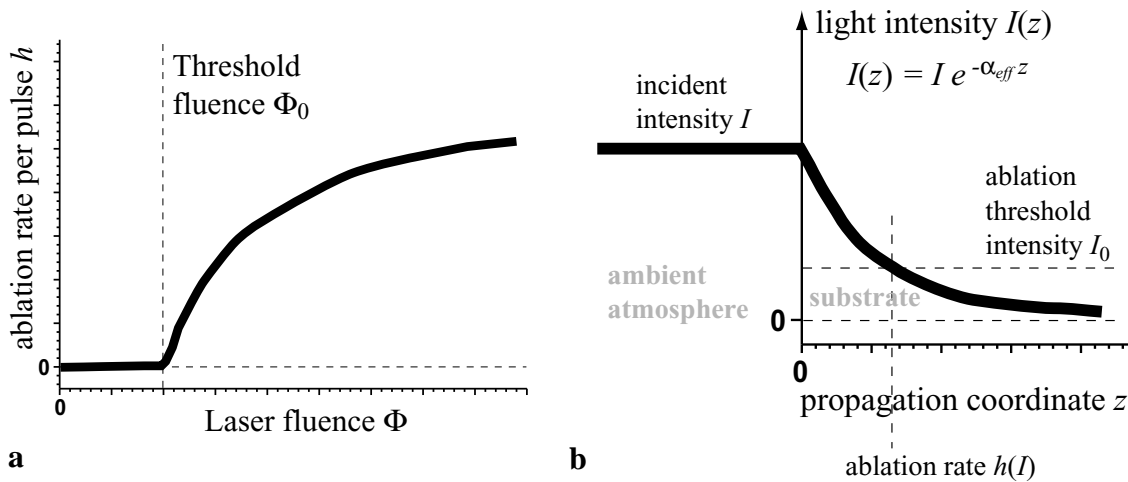


Figure II.1-2: (a) Schematic of a generalized ablation curve, showing the typical features: ablation threshold and increasing ablation rate with laser fluence. (b) Schematic showing Beer’s absorption law applied to Laser Ablation (The reflectivity of the sample is neglected). ($z < 0$ corresponds to the ambient atmosphere, $z > 0$ to the substrate.)

The simplest possibility to fit ablation curves of highly absorbing polymers is based on Beer’s absorption law (with the effective high intensity absorption coefficient α_{eff}) and on the existence of an ablation threshold (at fluence Φ_0) [13, p. 223]. When considering that material is only ablated if $\Phi(z) \geq \Phi_0$, one finds with Beer’s law (Figure II.1-2b):

$$\Phi_0 = \Phi \times e^{-\alpha_{\text{eff}} \times h(\Phi)} \quad (1)$$

Hence, the expression for the ablation curve $h(\Phi)$ is:

$$h(\Phi) = \frac{1}{\alpha_{\text{eff}}} \ln(\Phi) - \frac{1}{\alpha_{\text{eff}}} \ln(\Phi_0) \quad (2)$$

This expression correctly describes the ablation curves of the substrates that were used in this work for not too high fluences. At high fluences the measured ablation curves (section III.3) saturate because of shadowing effects caused by the ejected material [14]. In fact, in this case the measured incident fluence Φ is no longer equivalent to the fluence deposited in the substrate material.

Modeling of the ablation curves $h(\Phi)$ is one of the possible ways to determine the detailed mechanism, how the deposited energy causes finally the bond breaking, and a lot of work focussed on this subject in the past years. Today, the “thermal” approach [15] or a “mixed” approach [13, p. 209] seems to be better for the description of most substrate-wavelength combinations than the early “photonic” proposition [16] of decomposition by direct bond breaking. A newer fundamental approach, mostly powered by the interest in nano particle formation, are molecular dynamics calculations [17], which do not need macroscopic information on the material at high temperatures (heat conductivity etc.). The thermal models assume that the absorbed energy is first transposed to the lattice, then eventually phase changes happen, and finally desorption or phase explosion removes the particles from the bulk material.

Laser Ablation of PET at 193 nm is expected to follow a mainly thermal decomposition scheme [18,19].

II.1.2 Problems in multiple pulse ablation

Some aspects of multiple pulse ablation are not completely understood to the best of my knowledge.

A study on the influence of the pulse repetition rate f on the ablation rate h was published [15]. The authors show that the ablation rate of high absorbing polymers (polyimide PI, PET, PEN) is insensitive to variations of the pulse repetition rate f up to some kHz. However, for low absorbing polymers like poly(methyl methacrylate) (PMMA), they measured already an ablation rate enhancement of approximately 30% at $f = 300$ kHz with respect to $f = 10$ Hz.

The sensitivity of the ablation process to the pulse repetition rate is however dependent on the form of the substrate (rather bulky, thin film, etc.). For example Bahners *et al.* irradiated PET fabric, and found macroscopic melting already at $f = 30$ Hz [20]. For our 100 μm thick samples, no differences in the surface topography could be observed in the accessible range of $1 \text{ Hz} \leq f \leq 50 \text{ Hz}$.

An important topic of multiple pulse ablation, that is not yet completely understood, is the development of the borders of the ablated structures with the pulse number. Related works are published on the drilling of deep holes at high laser fluences [21]. Nevertheless, a theory allowing to predict the wall angle of a structure of width w , ablated with n pulses at fluence Φ in material x is not yet available.

II.1 LASER ABLATION

A frequent problem in scanning ablation, the formation of “stairways” instead of smooth ramps (section IV.1), was recently solved by Braun *et al.* [22,23]. They use special masks, which cause a sharp intensity distribution transversal to the scanning direction and a smooth intensity distribution in the direction of the scanning. In this way, the resulting structure shows well defined borders, as with a standard binary mask, but no stairway at the beginning and the end.

II.2 Surface modification

Laser Ablation results in a chemically and physically modified surface after ablation. Especially for PET, a decrease in the O/C atomic ratio and an increased hydrophobicity were detected by X-ray Photoelectron Spectroscopy and contact angle measurements respectively. Moreover, the laser modified layer is amorphous. A variety of topographical structures were also observed on irradiated PET surfaces. In the order of increasing fluence, the structures appearing are: (i) LIPSS, which are caused by interferences. (ii) Dendrites, developing after irradiation under pre-vacuum. (iii) Cones, originate from shielding effects. (iv) Finally, the Nap-type and Wall-type Structures, which appear only upon irradiation of stretched polymers. The orientation of the Wall-type Structure is perpendicular to the stretching direction. In this work the Nap-type and Wall-type Structures will be referred to as "Static Structure".

In Figure II.1-2b it is visible that a part of the energy is deposited in layers of the substrate, which will not be ablated. This is the main reason why Laser Ablation leads to a modified surface of the substrate after ablation. The observed modifications are of both physical and chemical nature. For PET they can be divided into two categories, i.e. modifications of the *chemical surface composition* and modifications of the *topography* of the ablated surfaces.

The following sections summarize the literature reports on surface modifications of the clean ablated surfaces, i.e. with negligible redeposited material (debris) on the surfaces. The available information on the debris and debris covered surfaces are summarized in section II.3. The review focuses on PET, but reports on other polymers are mentioned as well, if no sufficient information was available on PET.

II.2.1 Chemical surface composition

Laser modified layer As PET is a thermoplastic polymer, a liquid layer exists during the Laser Ablation process [24]. Rapid cooling of the surface after the pulse results in an amorphous surface layer, with lower molecular weight and lower density than the bulk polymer.

The thickness of the amorphous layer formed was measured to be 85 nm by ellipsometry of PET surfaces irradiated with one pulse at $\lambda = 193$ nm at different fluences [25]. The conversion of the ellipsometrical angles into layer thicknesses was performed according to a single layer theoretical model. Also, TEM images of cross sections of the irradiated surface, show a dark layer at the surface [25]. The TEM measurement however, does not prove the modified layer to be really amorphous, because the same kind of contrast results from the difference of oriented crystalline domains and unoriented crystalline domains (section VI.1.1). On the contrary, spectroscopic measurements show that the intensities of the IR absorption bands corresponding to crystalline PET decrease and the intensities of the bands corresponding to amorphous PET increase after Laser Ablation at 248 nm [26,27], proving that the observed contrast in TEM originates from amorphization and not from reorientation of crystallites.

II.2 SURFACE MODIFICATION

The material in the laser modified layer is not only amorphous, but the polymer chains are also of lower molecular weight compared to the bulk polymer, as concluded from a dissolution experiment of a PET surface ablated at $\lambda = 193$ nm [28].

“Surface” Modifications of the “surface” of the polymer are frequently probed by *X-ray Photoelectron Spectroscopy (XPS)*. The sampling depth of this method at usual electron take-off-angles is approximately 5 nm in polymers. Mostly, the results are expressed as the development of the Oxygen to Carbon atomic ratio (O/C-ratio) of the surface after ablation, with respect to the initial polymer surface.

Nearly all authors found a decrease of the O/C-ratio, i.e. a carbonization of the PET surface after ablation [26,28-33]. This can be explained by mass spectroscopic measurements, which show that, already before ablation takes place, CO and CO₂ are released from the irradiated surface [18]. The same conclusion can be drawn from Attenuated Total Reflection Infrared Spectroscopy (ATR-IR) measurements [34]. The extend of the decrease differs from publication to publication, what may be explained by the dependency of the decrease in O/C-ratio on the laser fluence [26,29], on the electron take-off-angle [26] and on the irradiation wavelength [33]. Common to all publications, speaking of an O/C-ratio decrease, is that the irradiations were carried out on a static substrate. Knittel *et al.*, who reported twice an increase in the O/C-ratio, on the contrary, scanned the substrate under the beam [19,27]. Due to the scanning, they measured most probably an at least partially debris determined surface (see also section IV.2).

XPS measurements are often paralleled by contact angle measurements, which give information sensitive to the upper 7 atomic surface layers [35]. Usually, only water contact angles are measured. Contact angle measurements on ablated PET are difficult, because of the possible important roughness (section II.2.2).

Lazare *et al.* reported in a first paper increasing “equilibrium” contact angles γ after Laser Ablation of rough PET from 70° to 110° [28]. However, in a second paper advancing γ_a and receding γ_r contact angles of rough and smooth ablated PET are given [36]. Assuming that the angles published in the first paper are advancing contact angles on rough surfaces, the results are consistent. The measurement of the advancing and receding contact angles on smooth ablated PET, which gives indications on the chemical nature of the surface remaining after ablation, shows only a slight increase in γ_a from 71° to 79° and a more distinct decrease in γ_r from 57° to 38°. Watanabe *et al.* tested the hydrophilicity relative to untreated PET by a dynamic wettability measurement, which indicated a hydrophilic surface for single pulse irradiation with fluences below the ablation threshold, and a hydrophobic surface, if the fluence was above the ablation threshold [26]. They also measured “equilibrium” contact angles by the sessile drop method, giving the additional information, that the surface becomes hydrophobic after more than 10 pulses at low fluence. Finally, Lippert *et al.* reported a decrease of the polar surface energy component and an increase of the dispersive surface energy component after Laser Ablation, as concluded from advancing and receding contact angle measurements [33]. The contact angle measurements thus confirm the XPS results that the polarity and hence hydrophilicity of the *ablated* surfaces is lower than for the untreated samples.

Information on the functional groups at the surface is obtained from the fact that crystalline PET surfaces show a different chain orientation than amorphous PET, and thus exposes other functional groups at the surface [33]. This conformational change upon amorphization results in a decrease of the number of OH-groups at the surface, and thus hydrophobicity increases.

UV laser irradiation of polymers also influences the adhesion properties of metal films to the polymer substrates. Heitz *et al.* showed that irradiation of PET at $\lambda = 248$ nm, below and slightly above the ablation threshold, drastically increased the adhesion of electron beam evaporated metal films [37]. Niino *et al.* enabled for the metallization of poly(tetrafluoroethylene) (PTFE) and a co-polymer by irradiating at $\lambda = 193$ nm with fluences below the ablation threshold in reactive hydrazine atmosphere. After the irradiation the surface was activated, and finally electroless nickel plating was carried out [38,39].

Remarks All of the above mentioned surface modifications are also present in other polymers, but quantitative and sometimes also qualitative differences exist even if the chemical structure of the polymers is quite similar. For example the modified layer of PEN is cross-linked (amorphous, high molecular weight, high density), whereas the modified layer of PET is of low molecular weight [40]. The carbonization of the surface was also observed on PI [41]. Special to PI is the fact that irradiation with fluences around the ablation threshold extremely enhances the surface conductivity [42]. This effect can even be used for the production of conducting lines [43].

When considering applications of the modified polymer surface, one should always keep in mind that the treated polymer surfaces may be subject to important aging effects. Strobel *et al.* studied aging effects of PET and poly(propylene) (PP) after air-corona treatment, and found that PET surfaces show particularly fast aging compared to PP [44]. According to the authors, the main reason is the combination of the ester-groups in PET with the relatively high chain mobility. In consequence, the polar groups, that are generated by the surface treatment, can diffuse into the bulk in order to minimize the surface energy of the PET. The resulting decrease in wettability was partially reversible by storing the already aged PET for one week in water. This recovery of the formerly induced hydrophilicity of the surface is consistent with observations on the ablated micro channels [45].

II.2.2 Structure formation

Since the very beginning of research in Excimer Laser Ablation there has been interest in structure formation occurring in polymers upon Laser Ablation [2,46]. PET, being a frequently used polymer where structures develop in a wide fluence range, was investigated in detail by many authors. For PET, four types of polymer ablated surface structures are reported in literature:

LIPSS (Laser Induced Periodic Surface Structures) Although this kind of structure is not the only laser induced periodic surface structure, this name is used for a special kind of coherent structures, having a periodicity of the order of the irradiation wavelength. LIPSS formation occurs in a relatively small fluence window below the ablation threshold, $\Phi = 3\text{-}5$ mJ/cm² for irradiation of PET at 193 nm [47], which depends on the polarization of the laser light [48]. They

develop due to the interference of a surface scattered wave with the incident wave, and the resulting structures are regular over surfaces, which are much larger than the spatial coherence of the laser beam [48]. The structure formation itself is due to periodic melting and resolidification of the material at the locations of constructive interference and thermocapillarity [47]. Characteristic for LIPSS is, besides their wavelength, the dependency of the wavelength on the angle of incidence of the light. Further, different orientations of the structures with respect to the plane of incidence and different wavelengths are possible [13, section 28.2]. Finally, the material properties of the irradiated substrate and the pulse length of the laser determine which kind of LIPSS structure will develop [49]. With increasing pulse number $n \leq 1000$, the amplitude of LIPSS increases until approximately 80 nm, and decreases again at $n > 1000$ [47].

Dendrites At fluences around the ablation threshold, fractal dendrite like structures develop when the irradiation is carried out in ambient pressures ranging from 10^{-2} mbar to 100 mbar, depending on the used ambient gas [50,51]. The structures grow laterally at velocities of approximately 100 nm/h during annealing at approximately 60° after the irradiation, and are less than 60 nm high. Their growth can be stopped by evaporation of a thin metallic film on the substrate [51] or by storage at temperatures of less than 4°C [52]. The arms of the dendrites can reach a length of up to 30 μm . First, crystallization of the laser induced amorphous layer was discussed as the driving force of the dendrite growth [51], but more recent results indicate that debris is also important, at least for the nucleation of the structures [52]. The dendrites get the most pronounced if not more than three laser pulses are used, at higher pulse numbers other surface structures are predominant [50].

Cones Cone like surface structures appear upon laser ablation with moderate fluences above the ablation threshold, if the ablation is not carried out in vacuum. The cones can be as high as the depth of the ablated hole, and their symmetry axes coincide with the direction of the incident laser [13, p. 506]. Cones formation is due to shielding effects of debris [53], which redeposit onto the irradiated surface, or impurities in the material [54]. For the shielding to be effective, the ablation threshold of the debris, or of the impurities, needs to be higher than the ablation threshold of the substrate and higher than the applied fluence. For PET, cone formation was observed at high pulse numbers at fluences below 300 mJ/cm^2 by irradiating a surface of 1 mm^2 (Figure V.4-2a).

Nap-type and Wall-type Structures Finally, for fluences higher than the ablation threshold, a “Nap-type” or “Wall-type” Structure develops in stretched PET films, depending on the pre-treatment of the polymer films. The typical lateral structure sizes Λ range from $\Lambda = 1 \mu\text{m}$ [20] to $\Lambda = 8 \mu\text{m}$ [55] (see also Figure V.1-4a). The orientation of the Wall-type Structure, which develops in uniaxially stretched substrates, is perpendicular to the stretching direction of the films or filaments [56,57] (Figure V.1-1a). The Nap-type Structure (Figure V.1-4a) develops if biaxially stretched substrates are used [56]. The lateral size and the height of the structures increases logarithmically with increasing pulse number and increasing fluence [55,58-60] (see also Appendix A). On the contrary, the lateral size of the structure decreases with increasing absorption coefficient of the substrate [61]. Further, it was shown that in PET fibers, the period of

the structure also depends on the extent of stretching of the fibers [55]. Nap and Wall-type Structures can superpose in biaxially stretched substrates, if the stretching is different in the two stretching directions. The appearance of the structure is then similar to aligned mountain chains (Figure V.1-2a and Figure V.1-3a). The structures are observed with identical features after nanosecond and femtosecond excimer laser ablation [49]. All above described variations of the Nap-type Structure, the Wall-type Structure and superpositions of both will be summarized in this work under the name “*Static Structure*”, because it is the structure, that is observed after Static Ablation.

A detailed investigation of the Static Structure was given by Hopp *et al.* [58]. Among other effects, they examined the structure changes occurring by variation of the angle of incidence of the light. They found that the polygon borders, separating the naps, became longer in the direction of the incident light when the angle of light incidence exceeded 70° . For angles below 70° , only minor structural changes were observed. The observed changes of the structure could be explained by shadowing effects.

The reason for the Static Structure formation was discussed controversially in literature. Andrew *et al.* [46] and some other authors [36,62-64] proposed an explanation based on selective etching of amorphous and crystalline domains in the polymer. However, for the explanation of the Static Structure formation in PET the theory revealed wrong, even if differences in the ablation behavior of crystalline and amorphous PET could be measured [63]. Arenholz *et al.* ablated unstretched PET samples with crystallinities from 4% to 35% and could not identify structures larger than $0.1 \mu\text{m}$ [56]. Complementary to this, Kesting *et al.* observed the Static Structure on stretched poly(m-phenylene-2,2-bis[4-(3,4-dicarboxy-phenoxy)]phenylpropanimide) (PEI) fibers, a polymer which stays amorphous upon stretching [65]. Thus, it is confirmed that, independently of the crystallinity, stretching of the polymer is necessary for the structure formation to occur. Bahners *et al.* developed a synergetic model, which is based on Marangoni convection in the liquid layer during ablation, in order to explain the structure formation [66]. The borders between the Naps, which are visible by both SEM (Figure II.2-1) and AFM [58], are consistent with a self organizing mechanism, for which such polygonal structure shapes are characteristic. Nevertheless, a model using a liquid layer cannot be valid for all materials, because Arenholz *et al.* observed the same kind of structures also in PI, a material that cannot melt [60].

A “*Stress Release Model*”, which describes qualitatively the Static Structure formation in melting and non-melting polymers, has been proposed by Arenholz *et al.* in order to explain all observed features of the Static Structure formation [13, p. 509,59]. The stresses that develop under the influence of the rapid laser induced heating and cooling play an important role in this model. The frozen stresses in the material, induced by substrate stretching prior to irradiation, only determine the direction of the crazes, which appear in order to release the total stress in the surface layer. The depth of the forming crazes is governed by the equilibrium between the decrease of potential energy during the stress release, and the increase in surface energy by the formation of new surfaces in the crazes. The results of a more fundamental theory, which can be applied to laser irradiation of polymers, fit quite well with the Stress Release Model. In this work we

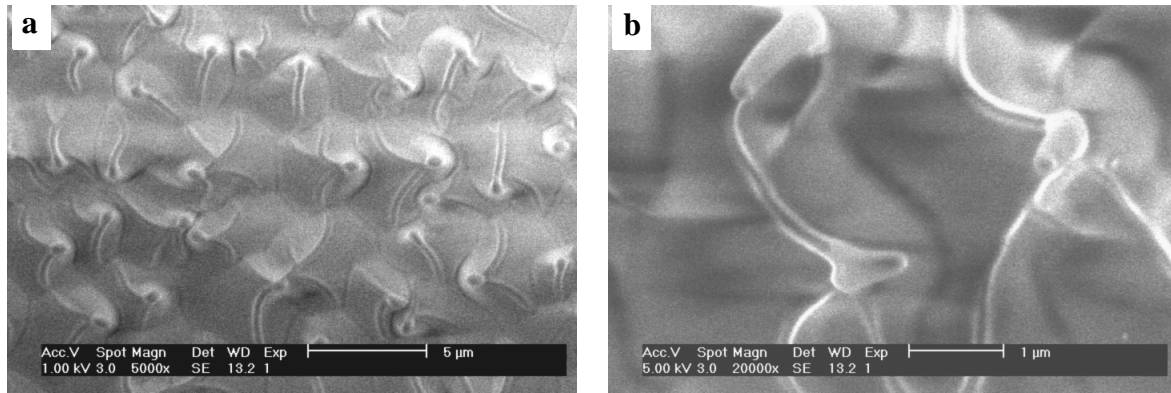


Figure II.2-1: Static Ablation of commercial biaxially stretched PET with 200 pulses at (a) $\Phi = 75 \text{ mJ/cm}^2$ (b) $\Phi = 300 \text{ mJ/cm}^2$. The black line in the middle of figure (b) is one of the polygon shaped borders separating the naps (figure (a)).

will use the name “*Defect - Deformation Model*” for this theory, which was developed by V. I. Emel’yanov [67]. The application of the Defect - Deformation Model to the Static Structure formation yields the right behavior of the structure periods with variations of the absorption coefficient of the substrate [61]. (The higher the absorption coefficients the smaller the structures.) Moreover, it predicts the right order of magnitude for the periods of the Static Structure, but based on some roughly estimated numerical values, which are necessary for obtaining quantitative information from the theory formulas. There is no obvious contradiction between the two models, and hence the Defect - Deformation Model may describe the fundamental physical processes, which leads to the self organization of the defects, and finally the crazes, developing with the successive laser pulses as described by the Stress Release Model.

Remarks As already mentioned, most of the described structures are not limited to Laser Ablation of PET, but can be observed in a variety of other polymers and other materials. For example, besides in the already mentioned polymers (PET, PI and PEI), the Nap and Wall type Structures (Static Structures) were observed in poly(amid) (PA66) [20], poly(ethylene 2,6-naphthalate) (PEN) [40], and a long series of other polymers [65]. LIPSS are known since the first laser experiments and were first discovered on semiconductors [13, p. 482]. (The usage of the name LIPS(S) in literature is not strictly limited to the definition used in this work.) Moreover, the above list of structure formation in polymers is not complete, because laser induced swelling of surfaces at fluences around the ablation threshold was not mentioned [68]. In other materials other structure formation processes are possible upon excimer laser irradiation. For example the up to 30 μm high tips, that develop upon laser irradiation of silicon [69,70].

II.3 Ablation Products

The strong forward peaking of the density distribution of the ejected ablation products in vacuum is even more pronounced for large irradiated surfaces. The ablation products, with initial velocities in the range of km/s, slow rapidly down, when the ablation is carried out in an ambient atmosphere. This causes a shock/blast wave in the ambient medium, and particulates form out of the ablation products. The drag forces of the shock wave cause redeposition of the particulate ablation products, called debris. The amount of debris can be up to 43% of the ablated material (per shot). The extent of the sideways expansion of the debris is higher, if more light molecules are produced, and can be modelled. Debris is difficult to remove and can be used as a surface modification. It consists mainly of amorphous and graphitic carbon, and is, depending on the atmosphere during ablation, charged, partially oxidized, hydrophilic and includes nitrogen moieties.

II.3.1 Expansion of ablation products

After the decomposition of the substrate material, the gaseous ablation products expand into the vacuum or the ambient atmosphere forming the so-called *plume* (Figure II.1-1c). The primary decomposition products can only be observed under vacuum, because the confinement of the ablation products to a small volume by the influence of the ambient pressure, and chemical reactions with the ambient atmosphere, influence the plume composition. Many publications are available on the expansion of the ablation plume, because the controlled recondensation of the ablation products on a support in front of the ablated target, opens new possibilities for thin film production. The domain of Pulsed Laser Deposition (PLD) is today probably the biggest and most active field of research in Laser Ablation.

According to Dyer *et al.*, the ablation products of PET at low fluence (90 mJ/cm^2) are mostly CO, CO₂, C₆H₆, C₂H₂ and C₂H₄ [18]. Watanabe *et al.* stated a decrease of the ethylene yield at higher fluences [30]. Small carbon clusters, mainly C₂, are frequently detected by Laser Induced Fluorescence (LIF) [71]. If the ablation is carried out in presence of oxygen, the CO yield decreases and more CO₂ is produced, as it was shown explicitly for PI [72]. At high fluences, as used in this study (1000 mJ/cm^2), polymer fragments are also expected to be ablated [30,71,73]. In general, the ablation products depend strongly on the ablated substrate, the laser fluence, the ambient atmosphere and the laser wavelength.

The results on the density distribution and the velocity distribution of the ejected particles can more easily be generalized. Lazare *et al.* [74] measured the angular density distribution $\rho(\varphi)$ of the ablation products after ablation of several polymers, and found that the experimental data could be fitted independently of the angle of light incidence by:

$$\rho(\varphi) = \rho_0 \times \cos^p(\varphi). \quad (3)$$

Where φ is the solid angle measured from the normal of the surface (Figure IV.2-2a). The parameter p , describing the directionality of the plume, depends on the applied fluence. For the

combination PET / 193 nm, the parameter p ranges from 7 to approximately 30 when increasing the fluence from 90 mJ/cm² to 1200 mJ/cm². Thus, the angular density distribution is strongly forward peaked, when the irradiation is carried out in vacuum (5×10^{-5} mbar). The rotational symmetry of Eq. 3 is only found for the ablation of a circular or point like surface. For the ablation of rectangular surfaces the density distribution of the particles can also be described by Eq. 3, but the parameter p is different for the two different axes. The sideways expansion of the plume is more important in the direction of the short side of the irradiated rectangle, resulting in a 90° rotation of the shape of the deposited films with respect to the laser spot [75,76].

The velocity distribution of the particles can be measured by LIF [73] or Time Of Flight Mass Spectrometry (TOF-MS) [77]. Two or three groups of molecules are detected [71,77]. The maximum of the measured velocity distributions is in the range of 1 km/s to 10 km/s, i.e. highly supersonic, for all molecule groups. The velocity distributions can be fitted by different models: (i) Usually the experimental data show deviations from the classical Maxwell-Boltzmann fit [73,77]. (ii) Often, a Maxwell-Boltzmann fit with a single stream velocity, as in the case of supersonic beams, is used [77]. However, these data analysis results in different “temperatures” for the fit of the axial velocity distribution and the transversal velocity distribution. (iii) A better modification of the Maxwell-Boltzmann distribution takes into account a whole range of stream velocities, corresponding to molecules ejected from different depths in the polymer. The advantage of this method is, that the temperatures resulting from fits of the axial and the transversal velocity distributions are nearly identical [78].

When the ablation is carried out under ambient atmosphere, the formation of particles is enhanced, and the ejected molecules and particles slow rapidly down as they leave the surface [71]. The shock between the ejected molecules and the ambient gas results in the formation of a shock wave [79], which might develop to a blast wave if the ambient pressure is not too high [71]. After ablation with very high fluences, the blast wave can contain up to 80% of the energy of the laser pulse [80]. Mainly because the shocked gas is ionized and the plasma absorbs the laser radiation, which drives the blast wave by this means. The pressures at the surface of the ablated substrate, right after the pulse, are in the range of 150 bar to 200 bar [80,81].

II.3.2 Redeposition of ablation products - debris formation

As mentioned, particulate products, also named “ejecta” [82], are formed if the ablation is carried out in ambient atmosphere. This results in a separation of the ablation products into fast molecules, responsible for the formation of the shock/blast wave, and slow particulate products, which might redeposit onto the substrate [82]. The drag forces, generated by the blast wave, cause the redeposition of the slow particulate ablation products on the substrate, which are then called *debris*. The fate of the particulate ablation products, which are not redeposited onto the substrate as debris, depends on the gas flow over the substrate [72].

The blast wave model was proposed in 1987 by Koren *et al.*, in order to explain the strong decrease of the etch depth per pulse with increasing ambient pressure [83]. Küper *et al.* measured then the debris ring around an ablated surface of 1 mm diameter as a function of the ambient gas type and ambient gas pressure, and could perfectly explain their data by the blast wave theory

[81]. By dividing the 3D-problem of the debris redeposition into a 2D-problem, i.e. the sideways expansion of the particulate ablation products, and a 1D-problem, i.e. the redeposition of the particles on the substrate, Kelly *et al.* could calculate approximately which amount of the ablation products redeposits on the substrate [84]. They concluded that preferentially large molecules are redeposited, and that up to 43% of the material ablated by one pulse redeposits. (28% after 600 ns, with a pulse duration of 20 ns.) The sideways expansion of the particulate products, was described by a numerical simulation of a gas reservoir of the form of the ablated surface, which expands into vacuum. In spite of the approximations, the results describe well the debris patterns, observed around ablated surfaces. Figure II.3-1 shows the example of a rectangular irradiated zone, which is relevant for this work [75,84,85].

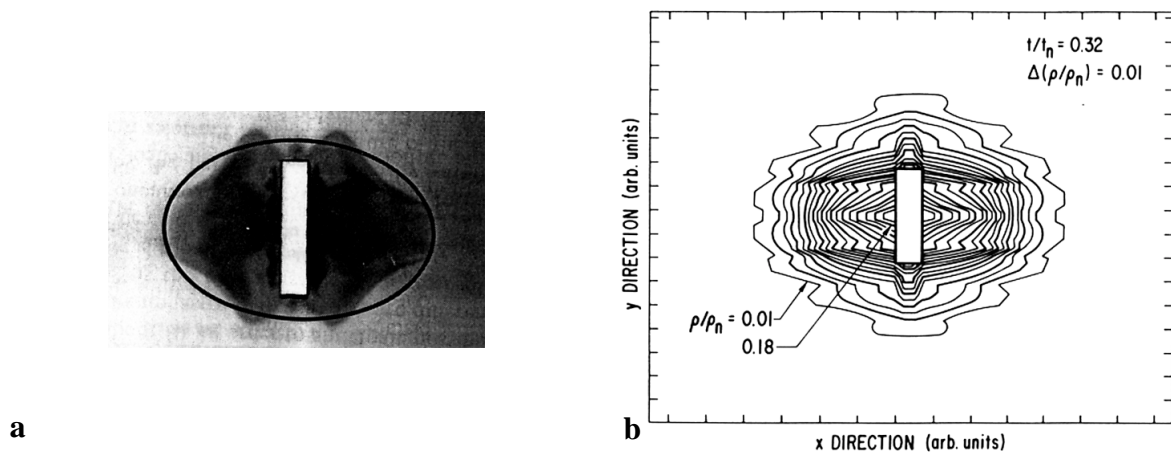


Figure II.3-1: (a) Experimentally observed debris pattern around a rectangular ablated surface in PI. (b) Calculated normalized density contours for the 2D-expansion of a rectangular gas reservoir. (Both from [85].)

The results of these calculations, as well as the experiments, indicate that debris expands more in the direction of the short dimension of the rectangle, than in the long one (Figure II.3-1). Thus the quantity of debris which redeposits near *one* side of the irradiated rectangle depends on the length of the other side.

Nearly all published work on debris is done in PI, because Laser Ablation of PI leads to strong debris redeposition, near the ablated area. Fast photographs of the expanding particulate products have shown important differences between different polymers [82]. In PI, the particulate products stay very close to the surface, and show a strong sideways expansion. In poly(methyl methacrylate) (PMMA) however, the particulate products expand mainly normal to the surface. This difference could be correlated to the different yields of production for light molecules and particulates upon ablation of the two materials. In the case of PI, 96% of the ablated mass results in light particles, which hinder the expansion of the particulates normal to the surface. For PMMA the light particles sum up to only 24% of the ablated mass [82]. (Singleton et al. report 82% of light products for PI [72].) In the case of PET, no fast photographs with the right time delay, or values for the yield of light molecule production compared to particulates are published to the best of my knowledge. On the basis of its high absorption coefficient, the decomposition of PET is expected to be more similar to PI than to PMMA, although it does not show

such an important debris redeposition as PI. On the basis of the polymer properties however, PET is more similar to PMMA than to PI, which cannot melt but decomposes upon heating. Another point is that the debris often decreases with increasing fluence [86], and thus the applied fluence in the literature reports has to be considered for comparisons.

The debris quantity, which redeposits onto the substrate, depends on the size of the irradiated region. This was shown directly for the debris redepositing on the ablated area, which causes cone formation [53] (section II.2.2). In the case of large area ablation, the evacuation of the ablation products is more difficult. It is essentially 1-dimensional, compared to 2.5-dimensional for small ablated spots. In consequence, the ablation products in the center of the plume are confined to a small volume during a “long” time, which favors particle formation and redeposition. Another factor, influencing the particulate production yield, is the nature of the ambient atmosphere. It was shown for PI that the particulate yield decreases drastically, when ablating in pure oxygen atmosphere instead of air [72]. This can be explained by the particle formation competing with chemical reactions of the primary ablation products with the ambient atmosphere.

II.3.3 Surface modification by debris

In micro fabrication, debris is mostly seen as dirt, and strategies to remove it, or to avoid the deposition, were developed. However, removing debris is not easy, because, once deposited, debris is well adherent to the substrate. Knittel *et al.* reported that rinsing with organic solvents does not completely remove the debris layer [19]. (Hiraoka *et al.* state on the contrary, that debris is removed by water spraying and drying from PI [87].) In the case of well adherent debris, laser cleaning seems to be successful on PI [88]. More frequently, one tries to avoid debris redeposition. This is possible by ablation under vacuum (Figure V.4-2b and c), but ablation in atmospheres or streams of light gases as H₂ or He is also successful [81]. In vacuum, the formation of the shock wave is avoided, and in He or H₂, the properties of the shock wave are modified, because of the low mass and the high speed of sound in these gasses. Another strategy is impregnation of the substrate by solvents prior to irradiation [19]. Ablation in reactive atmospheres also decreases or avoids debris [72]. Finally, debris can efficiently be collected on plate electrodes placed on the polymer surface. At transversal field strengths of more than 300 kV/m no more debris is observed on the polymer surface [89].

Because of its good adherence, debris can be regarded as a surface modification, which might be useful. The chemical composition of debris was analyzed by various research groups: It has for sure a high carbon content, as was concluded for PI from the absence of a measurable IR-spectrum [73]. Lippert *et al.* measured the composition of debris after laser ablation of PI by raman spectroscopy, and found it to be carbon with some crystalline graphitic features [41]. Another observation, that debris after laser ablation of polymers is electrically conducting, also indicates the graphitic nature of debris [19,89,90]. In the case of PET, cyclic oligomers were detected at high fluence [30], but not at rather low fluence [27]. All this indicates that debris determined surfaces, should be hydrophobic [19].

The influence of the ambient atmosphere reactivity on the production yield of particulate ablation products proves however, that the chemical composition of particulates is influenced by the

ambient gas [72]. The observation of CN upon Laser Ablation of PET in air also shows that the molecules of the ambient atmosphere can penetrate the plume of expanding ablation products [71]. Rossier *et al.* reported that the capacitive currents of their carbon electrodes, made out of debris of laser patterned poly(styrene) (PS), depends on the ambient atmosphere during the ablation process [90]. Significantly higher capacitive currents were observed after ablation in air, compared to argon and nitrogen, indicating a higher surface in contact with the electrolyte and/or a higher surface charge in the case of ablation in air. These observations all point to hydrophilic debris determined surfaces, as they were observed on PI by Hiraoka *et al.* [87], and mentioned on PET by Rossier *et al.* [5]. Another observation, that was used for metal plating of polymer substrates, is the charge of the remaining surface. After Scanning Ablation at 308 nm, Niino *et al.* measured a net positive surface charge on PET with an electrostatic voltmeter [91]. The charge is induced by redeposited debris. In order to explain their finding, they measured the yield for positive and negative ions when ablating in vacuum, and found an excess of positive ions [92]. On the contrary, von Gutfeld *et al.* state that they collected approximately the same amount of debris on anode and cathode, which were placed on the polymer surface [89]. XPS studies on debris determined surfaces are rare. Niino *et al.* mentioned a nitrogen signal on PET, ablated in air or nitrogen atmosphere, but do not report on the O/C-ratio of their XPS measurements [92]. Knittel *et al.* probably measured a debris determined surface and found the O/C-ratio to increase [19]. The deconvolution of their spectra has to be interpreted with caution, because their pure PET spectrum does not look like the spectrum in reference [93]. Some studies were performed in order to identify functional groups at the surface after Laser Ablation [65,94,95, ch. 3]. In all cases selective color tests or other selective binding methods are applied. The results are not very reproducible, but the authors agree, that, among others, COOH-groups and OH-groups are present on the PET surface after Laser Ablation.

II.3 ABLATION PRODUCTS

II.4 Wetting of liquids on solids

The interaction of liquids with a solid surface leads to the formation of a contact angle, depending on the interfacial energies of the three interfaces: solid-vapor, solid-liquid, and liquid-vapor. The contact angle is sensitive to the chemical composition of the uppermost atomic layers. Measuring contact angles of different liquids on a solid, allows for an estimation of the total surface energy of the solid, and its polar and dispersive components. Spreading of the liquid appears preferentially on high energy surfaces. On chemically heterogeneous or rough surfaces the advancing and the receding contact angles are different. On very rough surfaces the liquid is not in contact with the narrow “valleys” between the “hills”. In this case the contact angle hysteresis is low, and the behavior of such surfaces is similar to the behavior of smooth surfaces hardly interacting with the liquid.

II.4.1 Fundamentals

The term “wetting” or “wetting properties” describes the shape that a liquid volume assumes, when placed on a solid. Thus, the wetting properties describe the interaction of the liquid with the solid. The fundamental reason for wetting is the fact that a substance of given volume has more potential energy if it has a higher surface. In consequence, liquid volumes change their shape, in order to minimize the potential energy of the total system, composed of liquid, solid and vapor. A simple atomistic reasoning for existence of interfacial energies is illustrated in Figure II.4-1. In order to bring a particle out of the liquid bulk to the interface, work has to be done against the resulting force acting on a particle at the surface (Figure II.4-1).

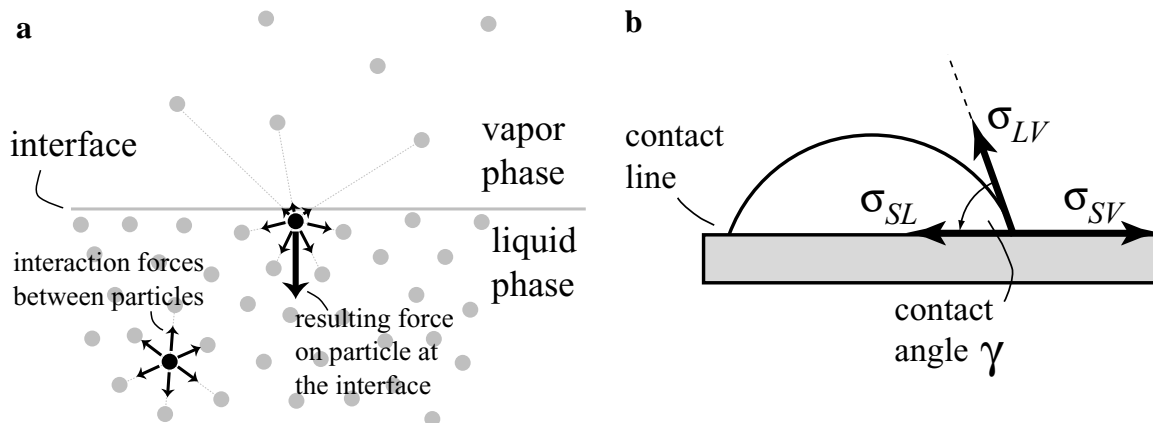


Figure II.4-1: (a) Scheme illustrating a simple atomistic reasoning for the existence of interfacial energies: because the interaction forces between two particles decrease with the distance of the particles, a force directed to the bulk of the liquid acts on particles at the interface [96]. (b) Scheme of a cross section of a liquid drop placed on a surface.

In the case of the interface between a liquid and its vapor, the interfacial energy σ per surface area is also called *surface tension*. Interfacial energies or surface tensions σ are expressed in unities of $\text{J} / \text{m}^2 = \text{N} / \text{m}$.

When placing a liquid volume on a solid, three different interfaces meet at the contact line, i.e. the border of the drop and the solid (Figure II.4-1b). The interfacial energies for solid-vapor, solid-liquid and liquid-vapor are named σ_{SV} , σ_{SL} , and σ_{LV} respectively. The equilibrium contact angle γ is given by Youngs equation [97]:

$$\sigma_{SV} - \sigma_{SL} = \sigma_{LV} \times \cos \gamma \quad (4)$$

Naturally, the contact angle γ cannot become smaller than 0° , corresponding to a thin film of liquid on the solid, even if $\sigma_{SV} - \sigma_{SL} > \sigma_{LV}$. For the cases, where $\cos \gamma < 1$ one says the liquid is *partially wetting* the solid, whereas in the case of $\sigma_{SV} - \sigma_{SL} > \sigma_{LV}$ one speaks of *spreading* of the liquid on the surface.

Often surfaces and liquids are separated into two categories, depending on their surface energies in vacuum (σ^0) [98]. Compounds with high intermolecular forces, often ionic or polar materials, have a high σ^0 and their surfaces are called *high energy surfaces*. Correspondingly, compounds with low intermolecular forces, like hydrocarbons, exhibit *low energy surfaces*. Often, low energy liquids spread on high energy solids (and liquids), for example fuel on water, and high energy liquids only partially wet low energy surfaces, for example water on most polymers.

For the case of partial wetting it is clear from Youngs equation (Eq. 4), that varying the chemical composition of liquid or solid affects the contact angle. By measuring the contact angle $\gamma(\sigma_{LV})$ on a certain solid, using different liquids with known σ_{LV} , it is then possible to conclude on properties of the solid. For low energy surfaces the points on a “Zisman-plot”, i.e. a plot of $\cos \gamma$ as a function of σ_{LV} , all lie in a narrow rectilinear band [98]. (For a homologous series of liquids it is a straight line.) The lower value of the interval in σ_{LV} , where the band cuts the value $\cos \gamma = 1$, is the “critical surface tension”, which is commonly used to estimate the surface energy σ^0 of the solid. Using other plots, and knowing the dispersive and polar contribution to σ_{LV} , allows even for a separation of the polar and the dispersive component of the surface energy of the solid [99].

Thus, contact angle measurements yield valuable information on the chemical composition of the solid surface. Additionally they are sensitive to the chemical composition of only the first 7 layers of atoms, thus being superior, in this sense, to many surface analysis methods [35].

II.4.2 Inhomogeneities

A drop of any liquid easily slides on a chemically homogeneous, atomically flat solid surface [97]. No energy is necessary for “close-to-equilibrium” motion (slow motion, negligible friction). However it is difficult to prepare such surfaces. Usual surfaces exhibit a certain degree of chemical heterogeneities and/or a certain surface roughness. Both kinds of heterogeneities are equivalent with the existence of “preferred sites” for the contact line on the surface [100]. Upon sliding of the drop an activation energy has to be overcome for going from one preferred site to the next. In other words, the heterogeneities cause “pinning” of the contact line, and thus the advancing and receding contact angles, γ_a and γ_r respectively, are no longer identical (Figure II.4-2a). The effect of different advancing and receding contact angles is called contact angle hysteresis [101].

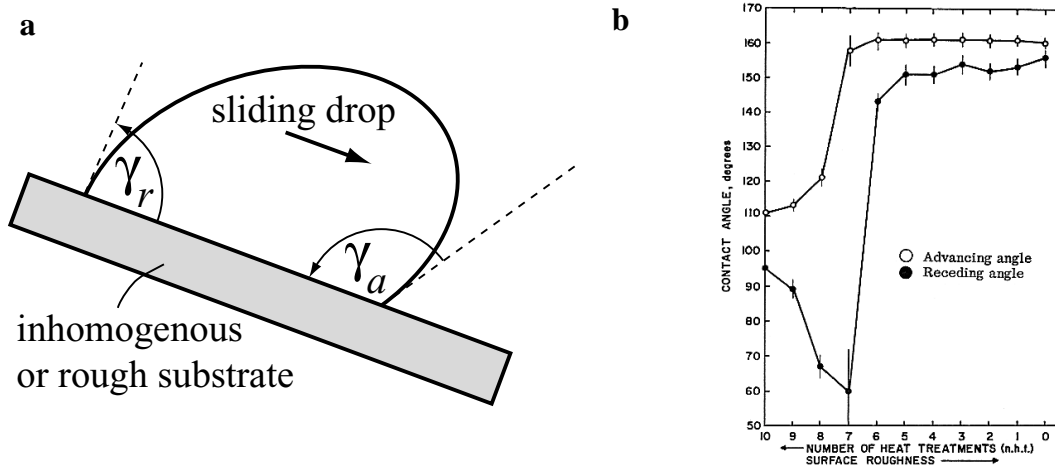


Figure II.4-2: (a) Schematic cross section of a sliding drop on an heterogeneous surface. (b) Measured advancing and receding water contact angles on Tetrafluoroethylene-methanol telomer wax surfaces of different roughness [102].

Special to roughness as surface heterogeneity is the fact, that the liquid is no longer in contact with the whole surface, if the surface roughness is very high. The liquid stays on the top of the “hills” and the vapor phase is found in the “valleys”. This occurred in the experiments of Dettre *et al.* for less than 6 smoothing heat treatments of their wax surface (Figure II.4-2b) [102]. In this case both, advancing and receding contact angles, are very high, similar to a homogenous surface having very little interaction with the liquid. The preparation of this kind of surfaces is subject to actual research [103], and economically interesting, because of, for example, the “self cleaning effect” of these surfaces.

The fact that only a small number of surfaces are as smooth and as chemically homogeneous as it is required for the absence of contact angle hysteresis implies that measurements of the equilibrium contact angle γ are nearly always affected by the way the drop is placed on the solid. The range of possible measured values of the equilibrium contact angle γ is the interval $[\gamma_a, \gamma_r]$. In conclusion, the measurement of γ_a and γ_r gives in practice much more information on the surface, than simply the value of the equilibrium contact angle γ [103].

II.5 Electroosmosis

Electroosmotic flow is caused by the movement of a thin charged layer of mobile solvated ions close to the channel walls under the action of an electrical field in the channel direction. The necessary charged layer (diffuse double layer) builds up when an electrolyte is in contact with a charged surface. The layer thickness is typically less than 10 nm. The transversal electrical potential in this layer, at the position of the moving ions closest to the channel wall, is called ζ -potential. If all walls are made out of the same material, the electroosmotic flow velocity is constant over the whole channel cross section except in the electrical double layer. In channels using different wall materials (composite channels) the flow velocity profile is more complicated. Electroosmotic flow is important in present micro fluidics analytic devices research, where the constant flow velocity over the whole channel cross section is required for high separation efficiency.

II.5.1 Fundamentals

Electroosmotic flow is based on the electrical double layer, which builds up when an electrolyte solution is in contact with a charged surface. The charged surface attracts electrostatically the counterions in the solution. Diffusion is the counter acting force, avoiding a complete charge separation.

Usually*, two qualitatively different layers of ions build up when an electrolyte solution is in contact with a surface of electrical potential Ψ_{-1} [104,105]. Both layers consist of solvated counter ions:

1. In the first layer, the solvated counter ions are electrostatically attracted by the charge of the surface and do not move under the influence of an external electrical field \vec{E}_z . This *outer Helmholtz layer* acts like a capacitor, and the variation of the potential $\Psi(x)$ is linear between the charged surface and the *outer Helmholtz surface* (Figure II.5-1). (Here x is the coordinate perpendicular to the surface.) The typical layer thickness is half the diameter of the solvated ions, i.e. 0.3 nm [104].
2. In electroosmosis, this first layer is often neglected because the ions cannot move, and only the second one, the *diffuse double layer* is considered [6]. It builds up due to the balance of electrostatic attraction and diffusion. This causes an exponential variation of $\Psi(x) = \Psi_0 \times \exp(-\kappa x)$ [6] (Figure II.5-1). Where Ψ_0 is the potential at the outer Helmholtz surface and κ the inverse Debye length.

A part of the ions forming this layer is only weakly bound and thus mobile under the influence of an electric field \vec{E}_z parallel to the charged surface. This movement is called elec-

* In cases where specific adsorption of partially solvated ions to the electrode surface is possible, a third layer exists. It is called the *inner Helmholtz layer* and is mainly composed of negatively charged ions, even for negatively charged surfaces [104]. The potential $\Psi(x)$ varies linearly between the charged surface and the *inner Helmholtz surface*. The thickness of this layer typically is half the diameter of the non solvated ions, i.e. 0.1 nm [104].

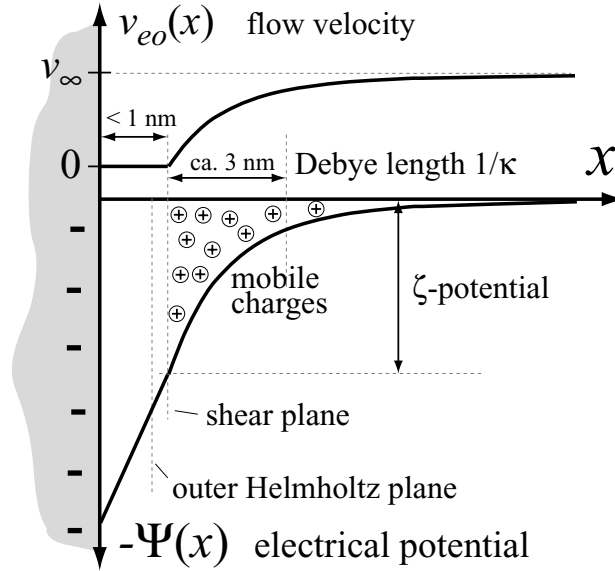


Figure II.5-1: Schematic of the electrical double layer.

trosmotic flow. The potential at the *shear plane*, separating the mobile from the immobile ions, is the ζ -potential (Figure II.5-1). Thus, the potential, in the mobile part of the diffuse double layer, which is important for the description of electroosmotic flow, is given by $\Psi(x) = \zeta \times \exp(-\kappa x)$.

The parameter κ describes how fast the potential near the charged surface reaches the bulk potential of the buffer solution. For a mono-monovalent buffer, it is given by

$$\kappa = \sqrt{\frac{2[\text{ion}]e_0^2}{\epsilon_r \epsilon_0 k_B T}} \quad [106]. \quad (5)$$

Here [ion] designs the number density, or concentration, of the ions, e_0 is the electron charge, ϵ_0 the dielectric vacuum permittivity, ϵ_r the relative dielectric permittivity of the electrolyte, and k_B the Boltzmann constant. The parameter $1/\kappa$ is called the *Debye length*, i.e. the 1/e-thickness of the diffuse double layer. Typical values for $1/\kappa$ range from 0.3 nm for ion concentrations of 100 mMol/l to 9 nm for 1 mMol/l.

As mentioned above, electroosmotic flow is driven by the movement of the mobile part of the diffuse double layer under the influence of an electric field \vec{E}_z parallel to the charged surface. In the case of capillary electrophoresis, the charged surface is the capillary wall, and the ζ -potential thus describes the charge density δ of the shear plane in front of the capillary wall, and indirectly the charge density of the capillary wall itself, both at the pH of the electrolyte solution. δ can be expressed as:

$$\delta = \kappa \epsilon_0 \epsilon_r \zeta \quad [6]. \quad (6)$$

Counteracting to the electrostatic force on the ions in the diffuse double layer is the viscosity η of the buffer solution in the capillary. For pure electroosmotic flow in a capillary of homogeneous chemical wall composition, the flow velocity $v_{eo}(x)$ is nearly independent of the radial po-

sition x in the capillary. The electroosmotic flow velocity profile $v_{eo}(x)$ approaches its saturation value v_∞ exponentially

$$v_{eo}(x) = \frac{\delta E_z}{\kappa\eta} \times \left(1 - e^{-\kappa x}\right) \quad (7)$$

with the same constant κ as the decay of the potential $\Psi(x)$ [6]. Hence the flow velocity in the whole channel, except the 10 nm regions near the channel walls, has the value

$$v_\infty = \frac{\delta E_z}{\kappa\eta} = \frac{\epsilon_0\epsilon_r\zeta E_z}{\eta} \quad (\text{Schmoluchowsky equation}). \quad (8)$$

(In Eq. 7 and Eq. 8 $E_z = \left|\vec{E}_z\right|$ is the absolute value of the external electrical field \vec{E}_z neglecting the direction of the flow.)

In the case of a homogenous chemical composition of the channel walls, v_∞ is approximately identical to the average electroosmotic flow velocity $\langle v_{eo} \rangle$ or simply v_{eo} , which can be measured. However, this approximation is only valid, if the channel dimensions allow to neglect the 20 nm zone where the flow velocity varies exponentially.

In order to distinguish the flat electroosmotic velocity profile from the parabolically shaped velocity profile of pressure driven flow, the electroosmotic velocity profile is often designed as *plug-profile*.

II.5.2 Applications in microfluidics

Electroosmotic flow is frequently used for the manipulation of small liquid volumes in the domain of micro fluidics. The main advantage is the easy implementation of two electrodes compared to a micro pump. A possible disadvantage is the influence of the relatively high electric fields (tens of kV/m) on other parts of the micro fluidic system.

Capillary *electrophoresis* is another domain where electroosmotic flow plays an important role [107]. Electrophoresis is an analytical separation method for electrolyte solutions, which is based on the different mobility of solvated particles exhibiting different charge (ζ -potential) and/or different size. The electrophoretic motion of particles in an electrical field is always superseded by the electroosmotic motion of the solvent. The high separation efficiency of capillary electrophoresis [108] is based on short separation times and the plug like shape of the electroosmotic flow velocity profile (section II.4.1) [6]. Short separation times minimize the diffusion induced broadening of the group of a certain type of particles which was in the sample solution. The plug like shape of the flow velocity minimizes the broadening of such a group of particles due to the absence of differences in the flow velocity at different radial positions in the channel. The principal types of flow velocity dispersion, diffusion-induced-dispersion and Taylor-dispersion, are thus minimized in capillary electrophoretic separations in homogeneous channels.

Hence, using electrokinetic effects allows for the simple fabrication of micro fluidic systems allowing for efficient manipulation, separation and detection of electrolyte sample solutions [108,109].

II.5.3 Composite channels

As explained before, the plug shape of the electroosmotic flow velocity profile is a key factor for the high separation efficiency of electrophoresis. However, the shape of the electroosmotic flow velocity profile $v_{eo}(x, y)$ in composite channels, i.e. channels where different wall materials are used, is no longer plug like [11,106,110]. Herr *et al.* investigated experimentally the flow in round channels, where the first part of the channel was a pure fused silica capillary (high ζ -potential), and the second part was a polymer coated fused silica capillary (low ζ -potential) [110]. Hence, they worked with a channel showing an *axial* difference in ζ -potential. In order to avoid edge effects, the measurement was performed “far” away from the ends of the channel and “far” away from the joint between the two parts of the channel. Their measurements confirmed former theoretical investigations, that the flow velocity profile in this case is described by a parabola superposed to the plug profile. In other words, the axial difference in ζ -potential induces a “negative pressure” in the part of the channel, having the higher ζ -potential, and a “positive pressure” in the part of the channel, having the lower ζ -potential. This influence of the chemical composition of the micro channel downstream or upstream on the flow velocity profile at the actual position, is mainly induced by the conservation of the flow volume in the process. Thus the use of such channels introduces Taylor-dispersion to the system, which may become the limiting factor for the resolution of the device [11].

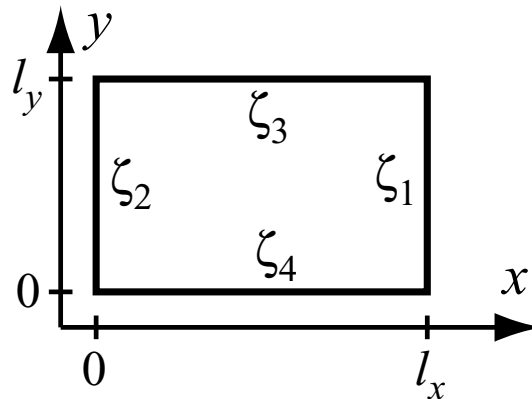


Figure II.5-2: Schematic of the cross section of a rectangular channel composed of walls with different ζ -potentials. The schematic defines the nomenclature of Eq. 9. (The channel dimensions l_x and l_y are measured from shear plane to shear plane.)

The use of different materials for the different walls of rectangular micro channel is another possibility of an heterogeneous ζ -potential distribution. Andreev and co-workers published in 1997 an analytical expression describing the electroosmotic flow velocity profile $v_{eo}(x, y)$ in rectangular channels, where each channel wall may have a different ζ -potential [106]. Based on the channel geometry presented in Figure II.5-2, the flow velocity profile in such channels is:

$$\begin{aligned}
 v_{eo}(x, y) = & -\frac{4b_0^2}{\pi} \times \sum_{k=0}^{\infty} \left\{ \frac{\sin(p_k y)}{2k+1} \left(\zeta_1 \left[\frac{\sinh(p_k x)}{\sinh(p_k l_x)} - \frac{\sinh(q_k x)}{\sinh(q_k l_x)} \right] + \zeta_2 \left[\frac{\sinh(p_k(l_x - x))}{\sinh(p_k l_x)} - \frac{\sinh(q_k(l_x - x))}{\sinh(q_k l_x)} \right] \right) \right. \\
 & \left. + \frac{\sin(m_k x)}{2k+1} \left(\zeta_3 \left[\frac{\sinh(m_k y)}{\sinh(m_k l_y)} - \frac{\sinh(n_k y)}{\sinh(n_k l_y)} \right] + \zeta_4 \left[\frac{\sinh(m_k(l_y - y))}{\sinh(m_k l_y)} - \frac{\sinh(n_k(l_y - y))}{\sinh(n_k l_y)} \right] \right) \right\}
 \end{aligned} \quad (9)$$

Here, p_k , q_k , m_k and n_k are simple functions of the sum counter k (Eq. 10), and $b_0^2 = (\epsilon_r \epsilon_0 E_z) / \eta$.

$$\begin{aligned}
 p_k &\equiv \frac{\pi(2k+1)}{l_y} & q_k &\equiv \sqrt{p_k^2 + \kappa^2} \\
 m_k &\equiv \frac{\pi(2k+1)}{l_x} & n_k &\equiv \sqrt{m_k^2 + \kappa^2}
 \end{aligned} \quad (10)$$

The micro channels produced by Laser Ablation are composed of three ablated walls and a lamination (section III.4), and the flow velocity profile is thus non-uniform, as described by Eq. 9. The experimentally important measurable value is the average electroosmotic flow velocity $\langle v_{eo} \rangle$:

$$\langle v_{eo} \rangle = \frac{1}{l_x l_y} \times \int_0^{l_x} \int_0^{l_y} v_{eo}(x, y) dy dx. \quad (11)$$

The electroosmotic flow profile $v_{eo}(x, y)$ in channels corresponding to the laser ablated channels, will be analyzed in section VI.4.2, according to Andreev's formula. The data given by Andreev *et al.* concentrates on large channels, where the side walls have little influence (l_x high, l_y low). In this case, the flow velocity $v(l_x/2, y)$ varies nearly linearly in the y -direction (except at the borders) [106].

III. Experimental

III.1 Laser Ablation

A standard mask projection setup is used, where the sample is mounted on a computer controlled translation stage. “Static Ablation” means ablation without sample movement during the irradiation. It is difficult to produce high quality micro fluidic channels by Static Ablation. “Scanning Ablation” means ablation where the sample is moved during the irradiation. Scanning Ablation leads to high quality channels with ramps at both ends. Ramps can also be ablated by other methods: Opening Mask Ablation, Closing Mask Ablation, Static Grey-Level-Mask Ablation and Diffractive Mask Ablation. The angle of inclination of a given ramp with respect to the not irradiated surface can be determined directly by a stylus profilometer, or it can be calculated knowing the relevant experimental parameters and the ablation curve $h(\Phi)$.

III.1.1 The ablation setup

The standard ablation setup, which was used for Static and Scanning Ablation is shown schematically in Figure III.1-1. The installation is integrated in the Center of Microtechnology of the EPFL and is installed in a class 100 clean room (Figure III.1-2b).

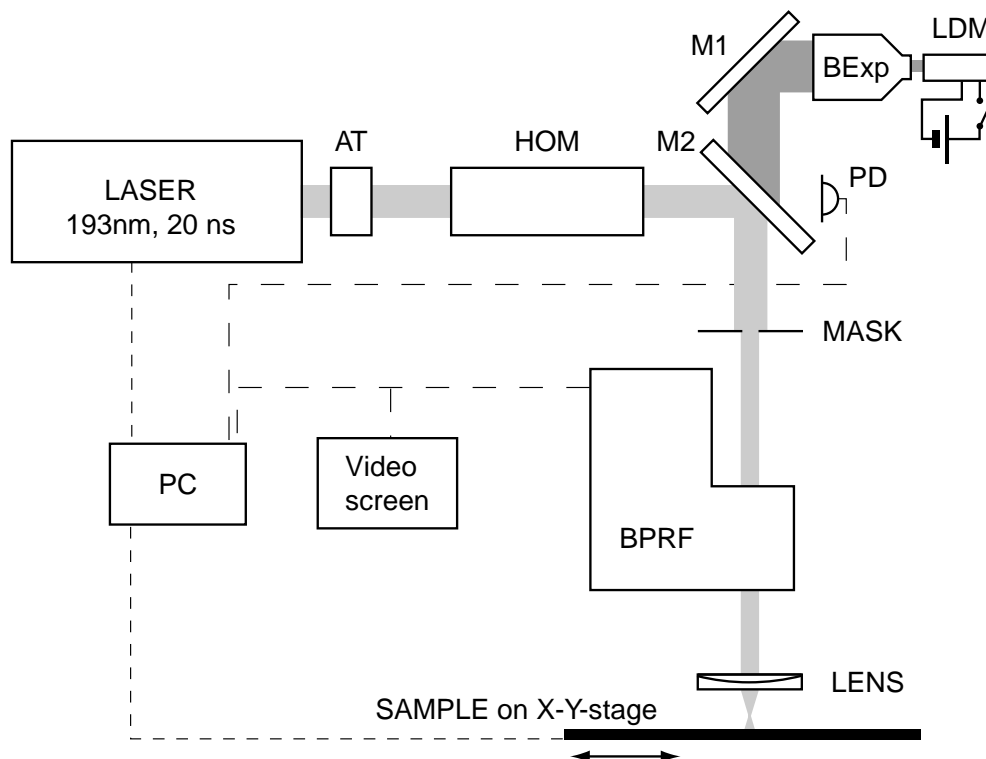


Figure III.1-1: Schematic of the standard setup, which is used for Static and Scanning Ablation. M1: Aluminium mirror; BExp: Beam expander; LDM: Laser diode module (visible); AT: attenuator; HOM: beam homogenizer; M2: dielectric mirror (HR 193nm); PD: photo diode; PC: The computer triggers the laser, drives the X-Y-stage and serves also for beam profile analysis; BPRF: beam profiler.

III.1 LASER ABLATION

The laser is a standard ArF excimer laser from Lambda Physik (Germany, model: LPX 205) emitting pulses of about 20 ns pulse length at a wavelength of 193 nm in the deep UV. The laser pulses are triggered by the computer and the maximum pulse repetition rate is 50 Hz. The attenuator (Excitech, England) directly after the laser output window serves to adjust pulse energy in order to obtain the desired fluence on the sample. The following beam homogenizer (Excitech, England) has two tasks: (i) it shapes the beam into a quadratic form and (ii) it creates a flat-top intensity distribution on the mask. We usually use 50 μm thick freestanding molybdenum masks, which were high precision laser cut with a home made Nd:YAG-slab laser running in fundamental mode [111]. The mask is imaged onto the substrate by a refractive projection lens (Excitech, England). The scaling of the mask projection is 10:1, and the resolution of the image, in terms of edge definition, is about 3 μm (Figure III.1-2a).

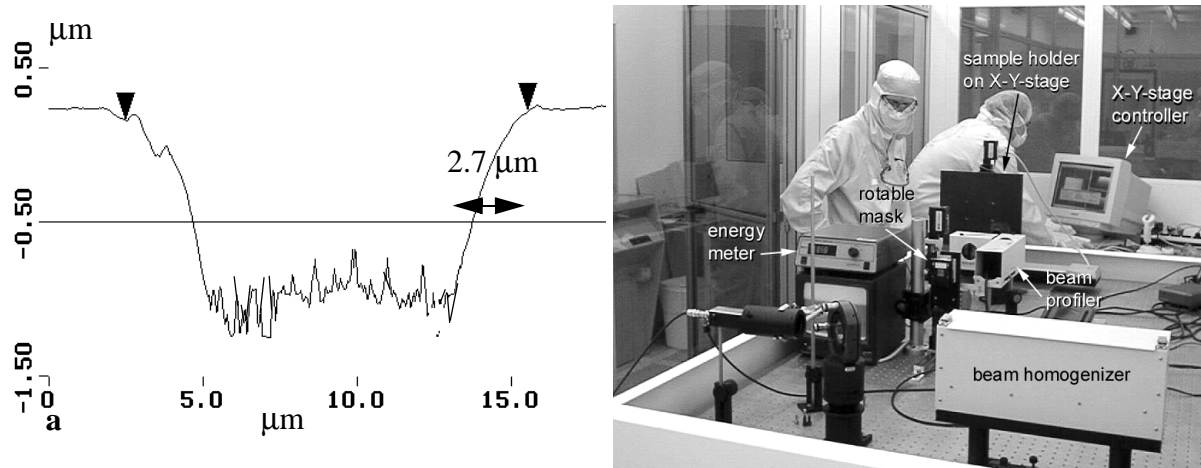


Figure III.1-2: (a) Cross section through an AFM image of a hole ablated with 3 pulses at $\Phi = 1200 \text{ mJ/cm}^2$ in commercial PET. (b) Photo of the setup, attenuator and laser are on the right, out of the image.

The sample holder is mounted on a computer controlled high precision X-Y-stage (Physik Instrumente, Germany). For adjustment, there are also a beam profiler, showing the intensity distribution in the mask plane, and a photodiode, which triggers the beam profiler. The computer also enables for spatial beam profile analysis.

The fluence was determined by inserting a 1 cm^2 mask and measuring the energy with a pyroelectric joule meter (Gentec, Canada) directly after the projection lens, i.e. approximately 5 cm in front of the sample. When the pulse energy was too low to trigger the display of the joule meter, the calibrated beam profiler was used for the energy measurement. The investigated fluences Φ ranged from 37 mJ/cm^2 to 1500 mJ/cm^2 , leading to ablation rates per pulse $h(\Phi)$ up to 0.21 μm . The ablation curves for the used substrates are presented together with the substrate description in section III.3.

As the micro fluidic channels, that are produced with the setup, are up to 40 μm deep, one is also interested in other features, i.e. the depth of focus of the mask projection and the material response to multiple shot ablation. These two properties were evaluated in the following experiment: A rectangular surface was statically ablated with 200 pulses at 1200 mJ/cm^2 on a sample

inclined of 45° with respect to the incident beam (Figure III.1-3a). The region of good structure quality, i.e. good edge definition, was measured by SEM imaging to be $70\ \mu\text{m}$ long (Figure III.1-3b). Thus, for an optimum structure quality, the sample position in the direction of light propagation has to be controlled within $\pm 25\ \mu\text{m}$ ($= 35\ \mu\text{m} \cos(45^\circ)$) prior to each ablation experiment.

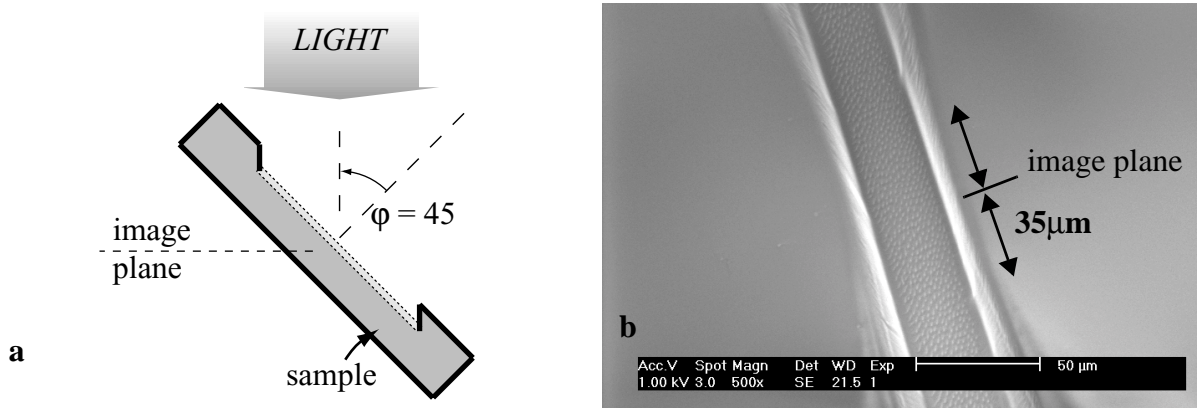


Figure III.1-3: Determination of the depth of focus. (a) Schematic of the experiment. (b) SEM image of the obtained channel (Static Ablation, $\phi = 45^\circ$, 200 pulses, $1200\ \text{mJ}/\text{cm}^2$).

III.1.2 Static Ablation

Most ablation experiments reported in literature are performed in the “*Static Ablation*” mode, i.e. the sample is not moved during the irradiation.

The micro channel production in this mode can be described by a cyclic repetition of the steps: (i) Fire n pulses on the substrate. (ii) Move the sample by the length of the irradiated spot a , such that the next hole will be produced in contact with the previous one.

The resulting depth d_{tot} of the channel will be

$$d_{tot} = n \times h(\Phi). \quad (12)$$

The geometry of the channels during fabrication is shown in Figure III.1-4a. The irradiated area is always parallel to the original sample surface.

In this mode the production of long high quality channels is particularly difficult, because it is nearly impossible to avoid small holes or walls in the channel floor due to a too big or too small movement between the production of neighboring holes (Figure III.1-4a).

If not otherwise mentioned $n = 200$ pulses were used for statically ablated structures.

III.1.3 Scanning Ablation

A better possibility to produce long high quality micro channels by Laser Ablation is the “*Scanning Ablation*” mode, which has very recently be called “*Sample Dragging*” [112].

In Scanning Ablation the substrate is simply scanned during the irradiation with a velocity v perpendicular to the incident laser beam. Due to the scanning, a ramp forms under the beam (Figure III.1-4b). (For further explanations please refer to section IV.1.)

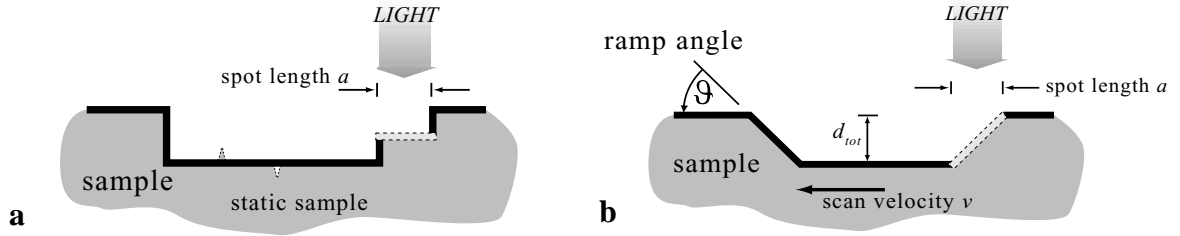


Figure III.1-4: Sketch of the channel geometries in *Static Ablation* (a) and *Scanning Ablation* (b). The figures show a cross section in the channel direction. The grey line represents the irradiated area.

The angle ϑ between the ramp and the original sample surface is given by the total depth d_{tot} of the channel and the length of the irradiated spot a :

$$\vartheta = \text{atan}(d_{tot}/a) = \text{atan}\left(\frac{n \times h(\Phi)}{a}\right) \quad (13)$$

As the existence of the ramp is a characteristic feature of Scanning Ablation (section IV.1), we usually produced series of channels at constant fluence Φ and constant number of pulses per site n , i.e. constant depth d_{tot} . The channels of one such series differ only in the ramp angle ϑ and the irradiated spot length a . The necessary scan speed v , at given pulse repetition rate f and given spot length a , can be expressed as

$$v = \frac{f \times a}{n}. \quad (14)$$

All channels, which were produced by Scanning Ablation, used $n = 200$ pulses per site. If not otherwise mentioned, the pulse repetition rate was $f = 50$ Hz. The spot width, which determines the channel width, was usually $40 \mu\text{m}$. The used spot lengths a and the resulting scan speeds v at $f = 50$ Hz are summarized in Table III.1-1.

a (μm):	1000	500	200	100	50	20
v ($\mu\text{m/s}$):	250	125	50	25	12.5	5

Table III.1-1: Summary of the used spot lengths a and the resulting scan velocities v (Eq. 14), supposing that $n = 200$ pulses per site and $f = 50$ Hz.

In order to obtain, *theoretically*, a rectangular cross section in channels produced in Scanning Ablation the rectangular mask has to be properly aligned with the scanning direction of the substrate. A misalignment of the mask produces in general a trapezoidal shape of the cross section of the channels. The reason is that for high pulse repetition rates f the transversal depth profile is proportional to the length of the irradiated spot shape measured in the scanning direction [23,112]. Thus, rotating the mask with respect to the scanning direction changes the channel cross section.

The *experimental* typical cross section of channels, produced with a properly aligned mask, was measured to be, nearly independent of the used spot length, a trapezoid of the following dimensions: upper width $w_t = 50 \mu\text{m}$, lower width $w_b = 29 \mu\text{m}$, depth (at $\Phi = 1000 \text{ mJ/cm}^2$) $d_{tot} =$

37 μm . This corresponds to a wall angle of $\beta = 74^\circ$, whereas the optimum is 90° (Figure III.4-1). The deviation from the optimum rectangular shape is due to the limited resolution of the mask projection and the material influences upon multiple pulse ablation. A possible slight misalignment of the mask, and heat effects due to the 50 Hz pulse repetition rate have only minor influence.

III.1.4 Ramp ablation

Ramps can be ablated by different techniques. Besides the presented Scanning Ablation, *Opening Mask Ablation*, *Closing Mask Ablation*, *Static Grey-Level-Mask Ablation* and *Diffractive Mask Ablation* can be used. (Opening Mask Ablation and Closing Mask Ablation were very recently called “Mask Dragging” [112].)

Opening Mask Ablation This technique generates a “number-of-shots-gradient” on the irradiated surface without moving the sample. During the irradiation, one side of the freestanding mask is moved in such a way, that the irradiated surface on the sample increases linearly with time. Using this method, the whole created ramp is irradiated at each shot, exactly as the irradiated ramp in Scanning Ablation. Debris cannot accumulate on this kind of ramp.

The distance, which the moving spot border travels during the irradiation time, plays the same role as the spot length a in Scanning Ablation and will also be called a . If, at the beginning of the irradiation, the mask was already opened by a certain distance, a flat ablated surface forms in contact with the ramp (Figure III.1-5a). If the mask let no light pass at the beginning of the irradiations, the resulting hole had a triangular shape (Figure III.1-5b).

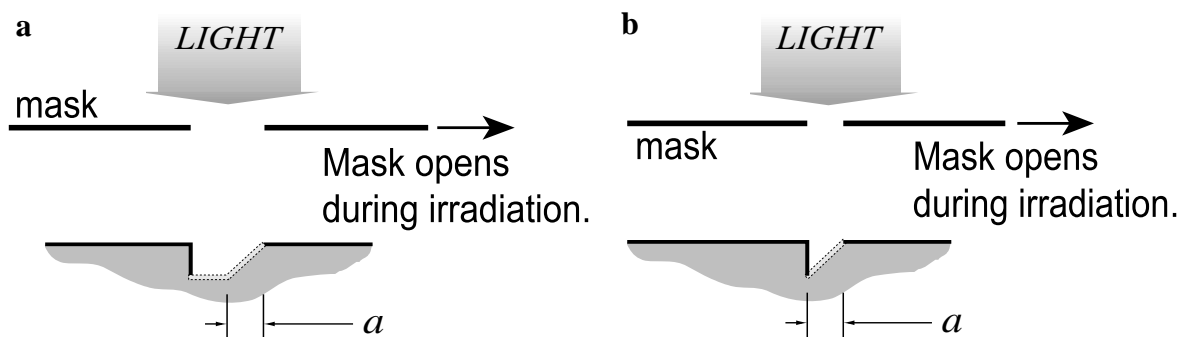


Figure III.1-5: Schematic of *Opening Mask Ablation* and possible shapes of the resulting structures: (a) With flat ablated surface, (b) triangular shape.

Closing Mask Ablation This method is very similar to the previous one, it also creates the ramp by a “number-of-shots-gradient” on the sample. When the mask is closed during the irradiation, the irradiated surface on the sample decreases more and more, and the already created parts of the ramp are no longer irradiated (Figure III.1-6a). This is the reason why debris can accumulate on this kind of ramps, which corresponds to the ramp at the beginning of the channel in Scanning Ablation.

Static Grey-Level-Mask Ablation and Diffractive Mask Ablation The irradiation through an adapted grey-level-mask or a diffractive mask can also create ramps (Figure III.1-6b). In both cases the whole ramp is irradiated with the same number of pulses, but the incident fluence

varies with the lateral coordinate. Thus, with increasing shot number, the ramp inclines more and more. In order to obtain a straight ramp, i.e. a linear variation of the ablated depth with the lateral coordinate, the generated intensity as a function of the lateral coordinate needs to take into account the ablation curve of the substrate material.

When the image of a binary mask is out of focus, one also has a relatively smooth intensity distribution at the edge. In this way, the smooth edges of structures, produced by a not perfectly focussed ablation, are of the same type of “ramp”. Moreover, even with a properly focussed mask, multiple pulse ablation produces walls having a certain wall angle, which depends on the material under investigation and the applied fluence (Figure III.4-1). As already mentioned, this wall angle is 74° in our case. Hence, the walls of the ablated structures are ramps of this type (Figure V.2-3c).

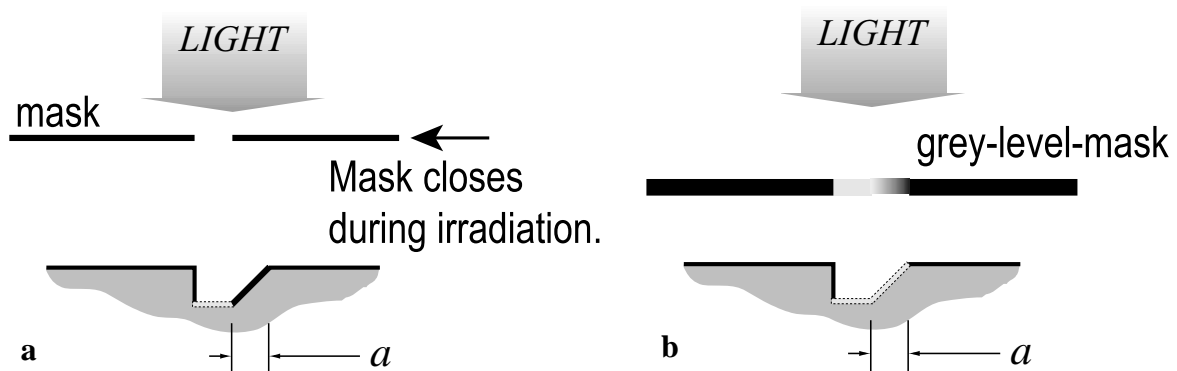


Figure III.1-6: (a) Schematic of *Closing Mask Ablation* and (b) schematic of *Static Grey-Level-Mask Ablation*.

III.1.5 Angle and ablation rate measurements

The depth measurements for the determination of the ablation rates per pulse were carried out by stylus profilometry (α -step 200, Tencor Instruments). The tip apex radius was $2\ \mu\text{m}$ and the force on the tip was $50\ \text{mN}$.

The ramp angles were determined by two different methods:

1. Indirectly, it was calculated by Eq. 13, knowing the applied fluence Φ , the number of pulses n , the ramp length a and the ablation curve $h(\Phi)$.
2. Directly, by scanning with the profilometer the upper part of the ramp and some tens of microns of the unirradiated surface nearby.

III.2 Surface characterization

The Topography of the ablated surfaces was mostly investigated by Scanning Electron Microscopy (SEM). The samples were not coated by an electrically conducting layer. Atomic Force Microscopy (AFM) was used alternatively, allowing for quantitative height information and high resolution images. Transmission Electron Microscopy (TEM) images of prepared cuts, gave information on the very high aspect ratio structures upon Static Ablation. Filtering in the transmission electron microscope allowed for visualization of the laser modified layer on the channel floor and for size estimation of the crystalline domains in the polymer. X-ray Photoelectron Spectroscopy (XPS) was used for the determination of the chemical composition of the ablated surfaces. The water wetting properties of the debris affected surfaces were estimated qualitatively by water condensation.

III.2.1 Topography

Scanning Electron Microscopy (SEM) is in this work the most frequently used topography investigation method. For this purpose the Philips XL30 FE-SEM of the CIME (Central Facility and Research Center in Electron Microscopy / EPFL) was used. All micrographs were taken with the secondary electron detector.

The polymer substrates were looked at without any conductive coating in order to avoid a superposition of the substrate structure with the coating structure. As PET is an electrical insulator, it is necessary to use a low acceleration voltage, i.e. 1-2 kV. Charging effects can nevertheless not be completely avoided. A good and frequent adjustment of the astigmatism is the key factor for submicron resolution, which allows for debris identification.

Besides the submicron lateral resolution, SEM has another advantage over optical microscopy, i.e. the depth of field. The high depth of field in SEM allows for a sharp image of the up to 3 μm high Static Structure.

If not otherwise mentioned the sample was not tilted, i.e. the electron beam incidence was normal to the unirradiated sample surface. Thus, all distances that are measured in the micrographs are directly the real dimensions on the sample, with an error of about 1%.

Atomic Force Microscopy (AFM) was used complementarily to SEM. It was applied to the detection of structures that could not be resolved in SEM, i.e. the structure of small debris quantities. The other application for AFM was the search for quantitative height information on the the observed structures.

Especially for the detection of small debris quantities, the PET substrates turned out to be difficult. Critical manipulation of the feedback parameters was necessary in order to obtain stick-and-slip free images. The debris images (Figure VI.2-3) were obtained with a Nanoscope 3A at the Institute of Condensed Matter Physics (Physics Department / University of Lausanne), and the AFM of the Static Structure (Figure V.1-3a) was taken with a Park Instruments Autoprobe

CP in intermittent contact mode at the Polymer Laboratory (Materials Science and Engineering Department / EPFL).

Transmission Electron Microscopy (TEM) of prepared cuts was used to observe the extreme high aspect ratio tips, which characterize the Static Structure in biaxially stretched PET. The principal aim of the TEM images was however to give a direct proof for the existence of an amorphized layer after Laser Ablation of PET. The sample preparation consisted in:

1. Moulding of the ablated samples in an epoxy resin (Araldite A, Ciba).
2. Contrasting the two polymers by staining with ruthenium-tetroxide (RuO_4).
3. Microtome cutting of 50 nm thick slices of the sample in different directions, i.e. parallel and perpendicular to the ablated surface.

The TEM images were taken on a Philips EM 430 operated at 300 kV at the CIME (Central Facility and Research Center in Electron Microscopy / EPFL).

For contrast creation between oriented crystalline domains and amorphous or unoriented crystalline domains in the polymer, a dark field filtering method was applied. A short description is given in section VI.1.1.

III.2.2 Chemistry

X-ray Photoelectron Spectroscopy (XPS) was used to determine the atomic composition of the surface. It also allows for a general description of the chemical group composition of the surface by analyzing the core spectra of the different elements. During deconvolution of the core or multiplex spectra care has to be taken, especially for non conductive substrates like PET, because charging effects during the acquisition cannot be excluded in spite of the electron shower for charge compensation (parameters: $E \cong 6$ eV, $I \cong 23$ mA). If charging takes place, the peaks get broader and the maxima may also shift from one run to the next. In consequence the acquisition time has to be kept low, resulting in quite noisy data. The absolute position of the spectrum is fixed approximately by the charge compensation during acquisition. After acquisition, the spectra are then shifted in order to fix the aromatic C1s peak exactly to the literature value. The acquisitions were performed on a Perkin Elmer PHI 5500 ESCA System at the Laboratory of Metallurgical Chemistry (Materials Science and Engineering Department / EPFL). The acquisition time was approximately 4 minutes. The take-of angle was 60° for both measurements, and we used monochromated AlK_α radiation (350 W) for the excitation. The pass energy for core spectra acquisition was set to 23 eV. Due to the limited spatial resolution of the system ($500 \times 500 \mu\text{m}^2$) the measurements were done in 1 mm large channels.

Water condensation was also used in order to get an idea of the water wettability (hydrophilicity) of the sample surface. Two different approaches were used:

1. In search of contact angle values *in* the standard channels, an experiment was performed in an Environmental Scanning Electron Microscope (ESEM) at the Swiss Federal Laboratories for Materials (EMPA). Unfortunately, it was not possible to obtain a clear image of a small drop in the channel.

2. In order to examine the influence of the debris on the wettability, water was condensed near the irradiated region by exhaling onto the substrate. Depending on the hydrophilicity of the substrate, the water condensed as droplets of different size or as a thin film. The repeatability of the experiment on the samples of one day was better than on samples of different days. This indicates that the error in the condensing experiment originates from the sample production and not from the measurement.

The condensing experiment gives valuable but only relative and qualitative information on the water contact angle of the observed surfaces. As the images are taken from above, one directly observes the diameter of the forming droplets for partially wetting surfaces and the interference colors of the thin water film in the case of complete wetting (spreading of water on the observed surface). In the interpretation of the images, main emphasis will be on the contrast between partial and complete wetting.

Electroosmotic flow velocity measurements were carried out in order to determine the ζ -potentials of the ablated surfaces in the channels as a function of the irradiation conditions. Besides the fact that knowledge on the electroosmotic flow is interesting for applications of the micro channels, the ζ -potential data itself is valuable information on the ablated surfaces (section II.5). Further information on the experimental procedure is given in section III.5.

III.2 SURFACE CHARACTERIZATION

III.3 Samples

Usually, a biaxially stretched commercial poly(ethylene terephthalate) (PET) film is used. Due to the presence of UV-stabilizers, the ablation threshold of these samples is slightly higher than the literature value. For some experiments, we stretched ourself an amorphous PET film, in order to obtain uniaxially stretched PET with known stretching direction and stretching strength. The stretching was carried out at room temperature and at $T_g < T < T_m$. Commercial, biaxially stretched Poly(ethylene naphthalate) (PEN) was also used. Its ablation threshold at 193 nm is higher than the one of PET.

III.3.1 Biaxially stretched PET samples

The usually used samples are pieces of a commercial Melinex S-grade film purchased from ICI (England) with a thickness of 100 μm . The samples were used “as received”, i.e. the films are biaxially stretched. The extend of stretching was not equal in each direction. The data sheet [113] gives different tensile strengths and different coefficients of thermal expansion in the two stretching directions. The fact that one stretching direction dominated over the other was also visible in the Static Structure formation (section V.1.3). Figure III.3-1 shows the chemical structure and the measured ablation curve for the standard PET substrate. The fit parameters according to Eq. 2 are $\alpha_{\text{eff}} = 1.83 (\pm 0.06) \times 10^5 \text{ cm}^{-1}$ and $\Phi_0 = 35 (\pm 2.3) \text{ mJ/cm}^2$.

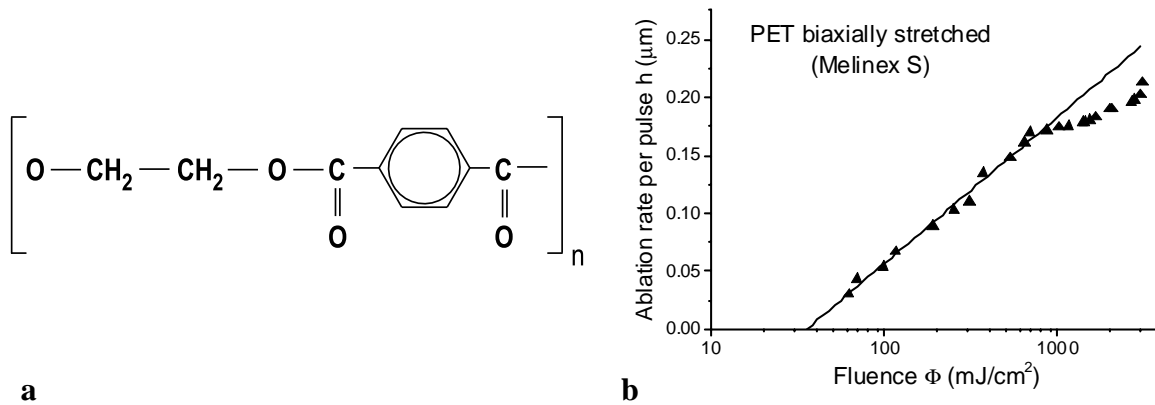


Figure III.3-1: (a) Chemical structure of poly(ethylene terephthalate) (PET). (b) the measured ablation curve of the used standard PET samples (at $\lambda = 193 \text{ nm}$, $\tau = 20 \text{ ns}$). ($\alpha_{\text{eff}} = 1.83 (\pm 0.06) \times 10^5 \text{ cm}^{-1}$ and $\Phi_0 = 35 (\pm 2.3) \text{ mJ/cm}^2$.)

Because of plume shadowing effects, which lower the ablation rate at high fluences, only the measurements with $\Phi < 900 \text{ mJ/cm}^2$ were used for the fit. The literature value for the ablation threshold of the same Melinex S samples, determined from fluences between 20 mJ/cm^2 and 200 mJ/cm^2 , is somewhat lower (28 mJ/cm^2 [18]) indicating already at relatively low fluences deviations from Eq. 2. Moreover, the error in the fluence measurement contributes to this deviation.

III.3.2 Production of uniaxially stretched PET samples

Frozen stresses in the polymer substrates are the reason for the structure formation upon Static Ablation. The standard PET substrate, which was used for nearly all experiments, represents a complicated frozen stress field. For more fundamental studies on the structure formation it was necessary to produce samples with a known and simple frozen stress field.

For this purpose we started from a commercial amorphous unoriented PET film with a thickness of 500 μm (Goodfellow) and prepared two types of samples.

Samples oriented at room temperature: Amorphous unoriented pieces of $3 \times 5 \text{ cm}^2$ were uniaxially stretched with constant bracket speed at room temperature in a traction test machine (809 Axial/Torsial Test System, MTS) in the Laboratory of Applied Mechanics and Reliability Analysis (Mechanical Engineering Department / EPFL). When stretching PET at room temperature, the deformation of the polymer is not homogenous. Only the part of low mechanical resistance at the border of original and stretched material is deformed (Figure III.3-2). This behavior is named “necking” [114].

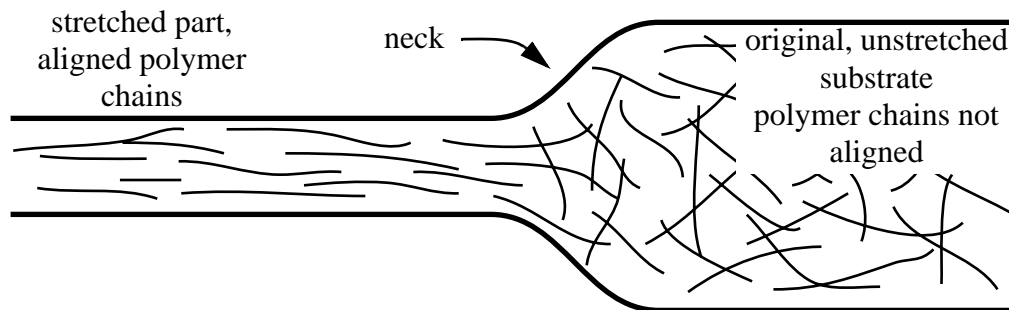


Figure III.3-2: Schematic of the neck, that appears upon drawing of PET at room temperature. Upon stretching of the film the neck propagates to the right.

Samples that are stretched with necking always show a high degree of molecular orientation [115]. The stretching process was slow enough to avoid complete crystallization, which can occur due to local heating in the neck [116]. However, after drawing, the samples exhibited a slightly hazy appearance due to enhanced crystallinity ($>20 \text{ vol.}\%$). The draw ratio DR of these samples (sample length after drawing divided by original sample length) was approximately $DR \cong 3.8$.

Samples oriented at 80°C : Samples with different degrees of chain orientation were prepared at the Laboratoire de Physico-Chimie Structurale et Macromoléculaire (UMR 7615) ESPCI, Paris (France) according to a recipe given by Chang et al. [117]. Pieces of $1 \times 3 \text{ cm}^2$ were stretched at 80°C , i.e. above the glass transition temperature and below the melting temperature of PET. The draw ratios DR were 1.5, 2.0, 2.5, 3.0 and 4.0. For this purpose, a testing system MTS 810 equipped with an interface MTS 458 and a temperature chamber regulated at $80 \pm 0.5^\circ\text{C}$ by means of a temperature controller (Barber Coleman) was used. The deformation rate was 0.003 s^{-1} and the samples were quenched after fabrication in order to avoid crystallization, which was not initiated by the chain alignment itself. The procedure resulted in transparent sam-

ples with slightly enhanced crystallinity at draw ratios bigger than 2, according to the literature [117].

III.3.3 poly(ethylene naphthalate) samples

For comparison, we used also commercial poly(ethylene naphthalate) (PEN) samples, which were purchased from Goodfellow (England). The 75 μm thick films were biaxially stretched. The difference in chemical structure between PEN and PET is that the para-substituted phenyl group of the PET-monomer is replaced by a 2-6-naphthalene unit (Figure III.3-3a). The bigger π -electron system leads to a red-shift of the absorption peaks, with respect to PET, and consequently to a lower low-intensity-absorption at 193 nm (30% of PET [40,62]). The high intensity absorption coefficient α_{eff} defined by Eq. 2 is only slightly lower than the one for PET (86% of PET). The measured ablation curve for the PEN substrate is given in Figure III.3-3b. The fit parameters according to Eq. 2 are $\alpha_{\text{eff}} = 1.57 (\pm 0.05) \times 10^5 \text{ cm}^{-1}$ and $\Phi_0 = 83.8 (\pm 3.1) \text{ mJ/cm}^2$.

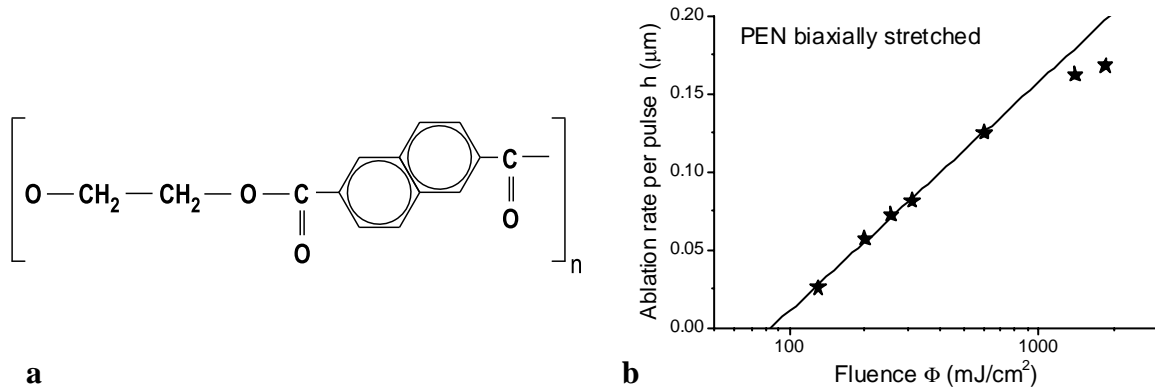


Figure III.3-3: (a) Chemical structure of poly(ethylene naphthalate) (PEN). (b) the measured ablation curve of the used PEN samples (at $\lambda = 193 \text{ nm}$, $\tau = 20 \text{ ns}$). ($\alpha_{\text{eff}} = 1.57 (\pm 0.05) \times 10^5 \text{ cm}^{-1}$ and $\Phi_0 = 83.8 (\pm 3.1) \text{ mJ/cm}^2$.)

III.3 SAMPLES

III.4 Micro fluidic channel production

Simple micro fluidic devices were produced for electroosmotic flow measurements. They consist of a straight micro channel, having a reservoir at each end. The channels between the reservoirs were produced by Scanning Ablation with different spot lengths and different scan velocities, leading to different ramp angles while conserving a constant channel cross section. The ablated channels are closed by a PE on PET lamination. The channels were produced in biaxially stretched and amorphous substrates. Depending on the substrate, the reservoirs were drilled through the substrate or through the lamination.

III.4.1 Channel types

In this section the production of the different types of channels, which were used for the electroosmotic measurements, will be described. In contrast to injection and analysis experiments, which require more complicated channels with at least one T-junction, the electroosmosis measurements are carried out with simple straight channels. The channels have two reservoirs, one at each end. In this subsection the ablation procedure of the channel between the reservoirs is described, before addressing in the next subsection to the production of the reservoirs and the lamination procedure, which is used to close the channels.

All channel types had approximately the same cross section, typically it is a trapezoid of the following dimensions: upper width $w_t = 50 \mu\text{m}$, lower width $w_b = 29 \mu\text{m}$, depth $d_{tot} = 37 \mu\text{m}$. This was achieved by fixing the fluence ($\Phi = 1000 \text{ mJ/cm}^2$) and the number of pulses per site ($n = 200$). Usually the pulse repetition rate of the laser was ($f = 50 \text{ Hz}$). Figure III.4-1 shows a SEM micrograph of a cross section, which was produced at slightly higher fluence.

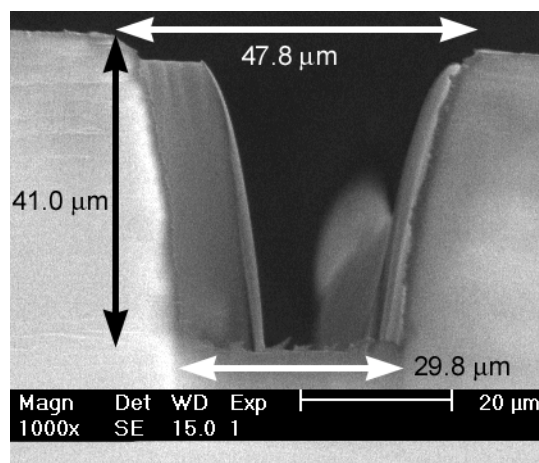


Figure III.4-1: SEM micrograph of a channel cross section, the parameters were $\Phi = 1200 \text{ mJ/cm}^2$ and $n = 200$.

Different kinds of channels produced by *Scanning Ablation* were then made by varying the spot length a and the scan speed v (see Table III.1-1). This finally determines the ramp angle ϑ to the values in Table III.4-1.

a (μm):	1000	500	200	100	50
ϑ ($^\circ$):	2.0	4.3	11	22	42

Table III.4-1: Used spot lengths a for the different micro fluidic channels and corresponding ramp angles ϑ .

Usually the closed part of the channel between the two reservoirs was 15 mm long. The depth of the channels showed a slight dependence on the spot length due to the fact that the pulse repetition rate was slightly higher than 50 Hz.

III.4.2 Channels in thin substrates

The biaxially stretched standard substrate is 100 μm thick. In these substrates the channel production procedure was as follows:

1. Two holes ($40 \times 1000 \mu\text{m}^2$) are drilled completely through the substrate. Free space between them is 15 mm and they will be used as reservoirs.
2. The channel is ablated between the two reservoirs using the mask that generates the appropriate spot length.
3. The substrate is laminated on the ablated front side with a poly(ethylene) on PET lamination at 125 $^\circ\text{C}$ (Morane Senator Lamination machine, Oxon, UK).
4. For the measurement the solutions drops are placed on the backside of the reservoirs.

A cross sectional view of the final structure is given in Figure III.4-2a.

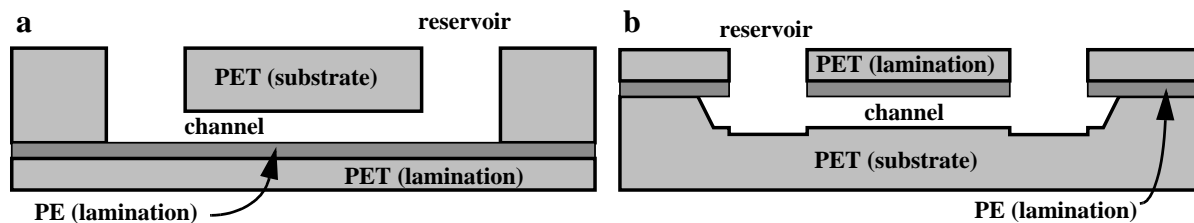


Figure III.4-2: Schematic cross sections in the channel direction of the micro fluidic channels showing the channel, the reservoirs and the lamination. (a) Channels in 100 μm thick substrates. (b) Channels in 500 μm thick substrates.

III.4.3 Channels in thick substrates

The unstretched amorphous substrate has a thickness of 500 μm . It turned out, that traversing reservoirs are not suitable for this kind of substrate, because the ratio, reservoir volume / channel volume, became too big. In consequence the data of the electroosmotic measurements was smoothed out and could not be evaluated. Thus the production procedure for channels in the unstretched substrate is as follows:

1. A channel of at least 15 mm is ablated using the mask that generates the appropriate spot length.
2. The ablated front side of the substrate is laminated.
3. The lamination is ablated using a spot size of $1 \times 1 \text{ mm}^2$ in order to generate surface reservoirs.

In the case of the surface reservoirs the covered channel length between the reservoirs was chosen to be 13 mm. The number of pulses for the ablation of the lamination was chosen to be sufficient to ablate about a micron of the underlying PET. A cross sectional view of the final structure is given in Figure III.4-2b.

III.4 MICRO FLUIDIC CHANNEL PRODUCTION

III.5 Electroosmotic flow measurements

The electroosmotic flow velocity in the channels is measured by the “current monitoring technique”. The channel length divided by the time that is necessary to replace the liquid in the channel by another one, yields the electroosmotic flow velocity in the channel. The electrical current in the channel was approximately $4\ \mu\text{A}$.

III.5.1 The current monitoring method

Before each measurement the channel was filled by placing $10\ \mu\text{l}$ of buffer solution (phosphate buffer $\text{pH} = 7.2$, $10\ \text{mMol/l}$) in one reservoir and pumping at the other side with a water pump. Afterwards the channel was inspected under a microscope, and, if bubbles were detected, the procedure was repeated. Once filled like this, the channel was rinsed by electroosmotic flow with three volumes of buffer solution before beginning the measurement, in order to be sure that the channel is properly rinsed.

The electroosmotic flow was then measured using Huang’s current monitoring method [118]. We placed volumes ($10\ \mu\text{l}$) of a buffer (phosphate buffer $\text{pH} = 7.2$, Sigma) in each reservoir. The total salt concentration of the buffer in the two reservoirs differed slightly ($10\ \text{mMol/l}$, $8\ \text{mMol/l}$). When applying the electric field that induced the electroosmotic flow, the resistivity of the channel was measured. The resistivity of the channel at a given time depends on the percentage of the channel filled with the low resistivity (high concentration) buffer and the percentage of the channel filled with the high resistivity (low concentration) buffer (Figure III.5-1a). The measurement of the channel resistivity as a function of time thus monitors the motion of the interface formed by the two liquids (Figure III.5-1b).

For all measurements, we applied a driving electrical field of $20\ \text{kV/m}$ and all quoted literature values are converted to this value for better comparison. The resulting electrical current varied around $4\ \mu\text{A}$ (Figure III.5-1b).

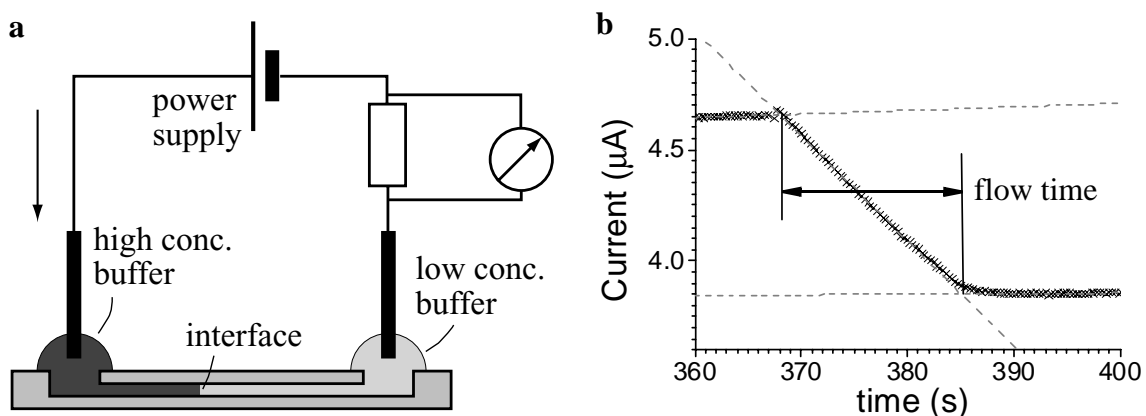


Figure III.5-1: (a) Setup of the current monitoring method for electroosmotic flow measurements. (b) Example of raw data with linear fits, showing low concentration buffer replacing high concentration buffer.

III.5.2 Data treatment

From the raw data as shown in Figure III.5-1b the flow time of the interface was extracted by fitting straight lines to the stable values and the current ramp. The time difference between the two intersection points of the three fitted lines was taken as one value for the flow time. As the channel length and the driving field are known, the flow velocity and the electroosmotic mobility can be calculated.

One point in the electroosmotic data corresponds to one channel that was measured with usually 3 pairs of buffer volumes, each used to generate 4 to 6 current ramps. Thus a value in the graph shows usually the mean of 12 measurements and the indicated error is the standard error (σ/\sqrt{N}).

IV. Scanning Ablation versus Static Ablation

IV.1 The geometry of the channels

Scanning Ablation produces ramps at the beginning and the end of each channel. The end ramp is the only irradiated surface, and its lowest part determines the structure of the channel floor. Channels, which are produced with high ramp angles (steep ramps), are expected to show the particularities of Scanning Ablation better than channels with low ramp angles. For long enough channels, the temporal development of a point on the ramp or on the channel floor can be observed spatially by observing the ramp or the channel floor respectively. End ramps can also be produced by Opening Mask Ablation. Beginning ramps correspond to ramps produced by Closing Mask Ablation, except that the debris contribution is lower after Closing Mask Ablation.

As already mentioned in section III.1.3, Scanning Ablation produces a different geometry of the channel during ablation, compared to Static Ablation. The characteristic feature of Scanning Ablation is the existence of the ramps at the beginning and the end of the channels. Figure IV.1-1 shows schematically how the ramps develop during the first pulses. Only one of the ramps, defined as the one at the *end* of the channel, is irradiated during channel production (Figure IV.1-1e). Hence, the structure on the channel floor is determined by the structure on the lowest part of the end ramp. When the light is normally incident to the unirradiated surface, both ramps have the same ramp angle ϑ , i.e. the angle formed by the ramp and the non-irradiated surface (Figure IV.1-1d). Comparing the irradiation conditions of the two ramps in Scanning Ablation to the ramp production by Opening or Closing Mask Ablation (section III.1.4), one sees that the *beginning ramp* in the channel is of the same type as the ramps being produced by *Closing Mask Ablation*. In both cases, the ramp forms due to a number-of-shots-gradient and only the lowest part of the ramp is irradiated. There is however a difference in the observed surface structures due to the different debris contributions (section IV.2.2). Analogously, the *end ramp* in the channel corresponds to a ramp produced by *Opening Mask Ablation*, the debris is similar in this case.

The ramp angle ϑ can vary theoretically in the range $\vartheta \in]0^\circ, 90^\circ [$. (The limits cannot be reached but they can be approached arbitrarily close.) Practically however, the upper limit is given by the wall angle $\beta = 74^\circ$ (section III.1.3). Upon Static Ablation, the irradiated surface is always parallel to the non-irradiated surface, independently from the angle of incidence of the light (Figure III.1-3a). In other words, Static Ablation is characterized by $\vartheta = 0^\circ$. Hence, in terms of the development of ϑ , we expect the particularities of Scanning Ablation to appear more clearly at high ramp angles than at low ramp angles. This is true for the observations reported in chapter V.

As already motioned in section III.1.3, the irradiated area has in general the form of a stairway rather than a ramp (Figure IV.1-1). However, if the width of the steps is comparable to the optical resolution of the mask projection Δx , the steps melt one into the next and can no longer be

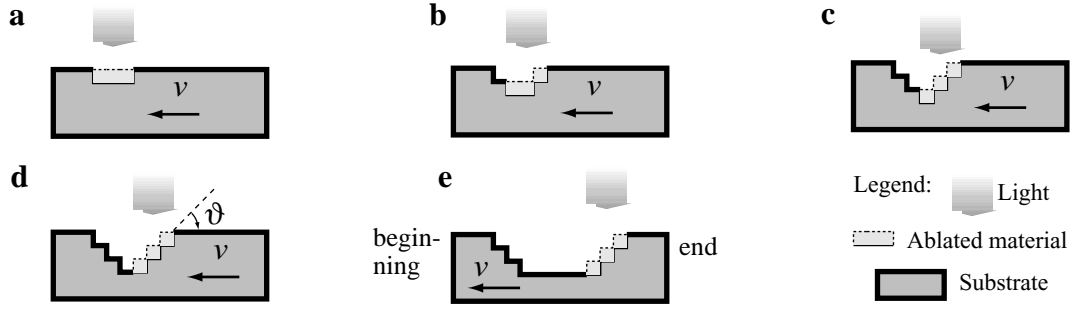


Figure IV.1-1: Ramp formation during Scanning Ablation for $n = 3$. The situation pulse after pulse: (a) First pulse. (b) Second pulse. (c) Third (n -th) pulse, beginning and end ramps are formed. (d) Forth ($n+1$ -th) pulse, the channel floor begins to form. (e) A small part of channel floor is produced with every pulse, while the end ramp moves away from the beginning ramp.

distinguished. If structure formation occurs on the irradiated area, the width of the steps has also to be bigger than the period Λ of the structure, for the steps to be resolved. The condition for the observation of a “smooth” ramp is then:

$$\frac{v}{f} \leq \max(\Delta x, \Lambda) \quad (15)$$

(Where v is the scan velocity and f the pulse repetition rate of the laser.) In our setup, we have $f = 50$ Hz, $\Delta x = 2.7 \mu\text{m}$ (section III.1.1) and $\Lambda = 3 \mu\text{m}$ (section V.1), hence, the maximum allowed scan velocity for obtaining smooth ramps is $v = 150 \mu\text{m/s}$, according to Eq. 15. We used however scan speeds of up to $250 \mu\text{m/s}$ without observing the stairway shape in the SEM. This is due to the fact that the ablation rate per pulse ($< 0.2 \mu\text{m}$, section III.3.1) is much smaller than the height of the Static Structure ($2 \mu\text{m}$, section V.1), thus the steps cannot be observed due to the high roughness of the surface.

If we neglect the early times, where the beginning ramp may be reached by ejected material, we can say that, due to the scanning, the time domain is transposed to different places in the channel direction, i.e. space, and becomes accessible to simple observation in this way. For example, it is possible to see the development of the period of the Static Structure from 0 to n pulses on a simple SEM of the irradiated ramp (Appendix A). Another example is how the temporal accumulation of debris on a certain point on the channel floor is visible as a debris gradient close to the end ramp (Figure V.4-4).

IV.2 Redeposition - Debris

“Indirect” debris redeposition, as described in section II.3.2, is more homogeneous in Scanning Ablation than in Static Ablation. The quantity of indirect debris depends on the shape of the irradiated spot (sections II.3.2 and VI.3.2), but not on the scanning. In Scanning Ablation another PLD like redeposition mechanism exists. The quantity of this “direct” redeposition is important at high ramp angles and negligible at small ramp angles. The total debris deposition in Scanning Ablation is a mixture of direct and indirect redeposition.

IV.2.1 Redepleted debris distribution due to scanning

When comparing Static and Scanning Ablation, one also has to consider the redeposition of particulate ablated material. This material is called debris and is redeposited on the substrate due to the drag forces of the generated shock wave (section II.3.2). On a molecular level, this means that collisions of the particulate ablation products with the molecules of the ambient air and the light ablation products occur, pushing some of the particulate ablation products back onto the substrate surface, where recondensation occurs. Due to the collisions with molecules of the ambient atmosphere, the chemical composition of debris depends on the chemical nature of the gas environment during the ablation process (section II.3.3). This *indirect redeposition* mechanism due to collisions with the surrounding gas takes place as well in Static Ablation as in Scanning Ablation.

In Static Ablation each of the n pulses hits the same surface and thus debris cannot accumulate on the ablated surface, if the fluence is high enough to ablate the debris of the preceding pulse (no cone formation, section II.2.2). Thus, for high enough fluences, only the debris of the last pulse is in the irradiated channel section, whereas near the irradiated surface debris will accumulate [84]. Thus, one expects a periodic, non homogenous, and perhaps discontinuous debris layer on the channel floor of a statically ablated channel (Figure IV.2-1a).

In Scanning Ablation, every point of the forming channel floor is once near the irradiated surface and only the end ramp is continuously cleaned from debris. Thus debris can accumulate homogeneously in the whole channel, because of the scanning of the substrate (Figure IV.2-1b).

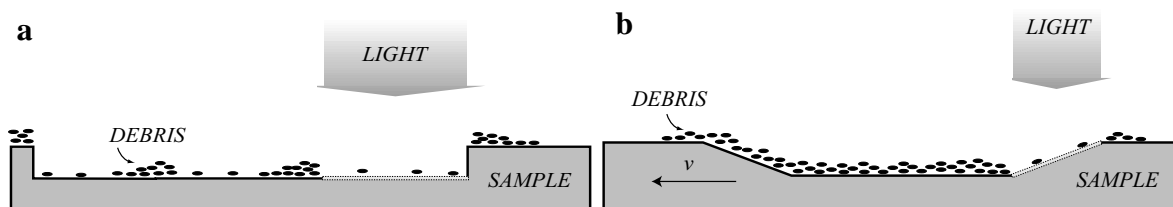


Figure IV.2-1: Debris redeposition in *Static Ablation* (a) and *Scanning Ablation* (b).

In Scanning Ablation debris can accumulate in the channel, in order to form a homogenous layer.

The main difference between Static Ablation and Scanning Ablation, with the same shape of the irradiated spot and a small ramp angle, is the *distribution* of the debris. The *quantity* of *indirect*

debris in the channel does not depend primarily on the substrate scanning, even if reflections of the shock wave at the channel floor might influence slightly the yield of indirect redeposition. However, the quantity of indirect debris in the channel is influenced by the shape of the ablated spot (sections II.3.2 and VI.3.2).

IV.2.2 Enhanced redeposition due to self PLD

In Scanning Ablation however, another mechanism exists resulting in the redeposition of ablated material. It becomes very important in Scanning Ablation with high ramp angles, and is negligible in Static Ablation. This mechanism, as explained below, will be named “*direct redeposition*” and is a kind of Pulsed Laser Deposition (PLD) with the target (irradiated ramp) and the substrate (channel) in one piece.

In PLD, a target material is laser ablated and the ejected ablation products (section II.3.1) are allowed to deposit onto a substrate, which is generally positioned facing the ablated target (Figure IV.2-2a). Usually the Laser is focussed to high fluences in this kind of experiment and the ablation takes place under vacuum ($< 10^{-3}$ mbar [13]). The angular density distribution $\rho(\varphi)$ in this conditions was measured by Lazare *et al.* [74] and can be expressed by:

$$\rho(\varphi) = \rho_0 \times \cos^p(\varphi) \quad (16)$$

Here ρ_0 is a normalization factor, φ is the solid angle measured from the surface normal (Figure IV.2-2a), and p is a parameter depending on the fluence, the material and the wavelength. As already reported in section II.3.1, this means that the material is ejected preferentially perpendicular to the irradiated surface.

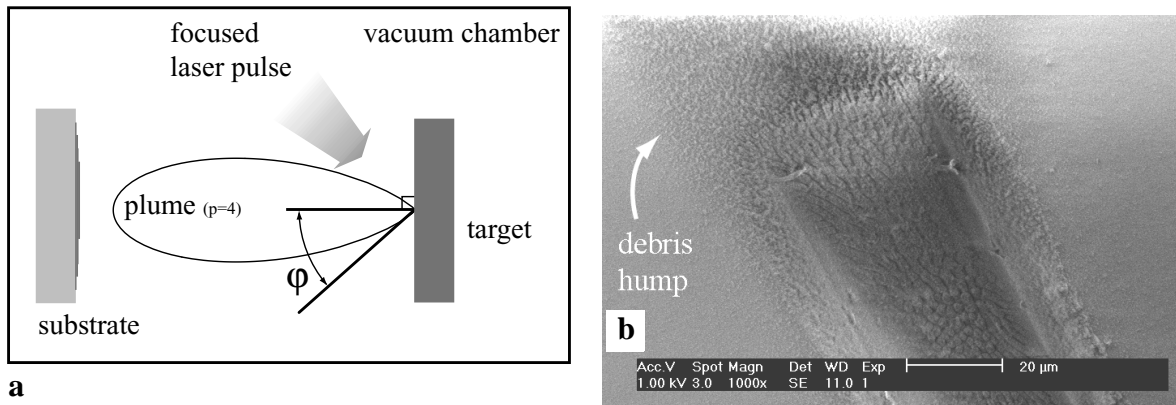


Figure IV.2-2: (a) Schematic PLD setup and visualization of the angular density distribution of the ejected particles $\rho(\varphi)$. (b) Beginning of a channel ablated in Scanning Ablation with $\vartheta = 32^\circ$. The ejected particles (debris) are concentrated around the normal to the ablated surface, i.e. the channel direction.

If a rectangular surface is irradiated in air the simple relation for $\rho(\varphi)$ will clearly no longer be valid. For example the rotational symmetry of Eq. 16 is not valid for rectangular ablated areas [76]. A feature of Eq. 16 that persists, is that material is mainly ejected in directions close to the surface normal. This is clearly visible in Figure IV.2-2b, where a SEM image of the surroundings of a beginning ramp is shown. The observed “hump”, caused by the accumulation of debris, is hardly larger than the ablated channel.

Thus, in Scanning Ablation a direct PLD-like deposition of material in the channel occurs, which is due to the tilt of the irradiated surface with respect to the channel floor. With increasing ϑ the channel floor and the walls cover more and more solid angle, and thus more and more debris deposits directly on them (Figure IV.2-3). It is not trivial to give an expression for the deposited debris quantity, because the density distribution ρ of the ejected particles will depend on many parameters. Namely: (i) The position in space. (ii) The form and the size of the irradiated area. (iii) The gas, in which the ablation is carried out.

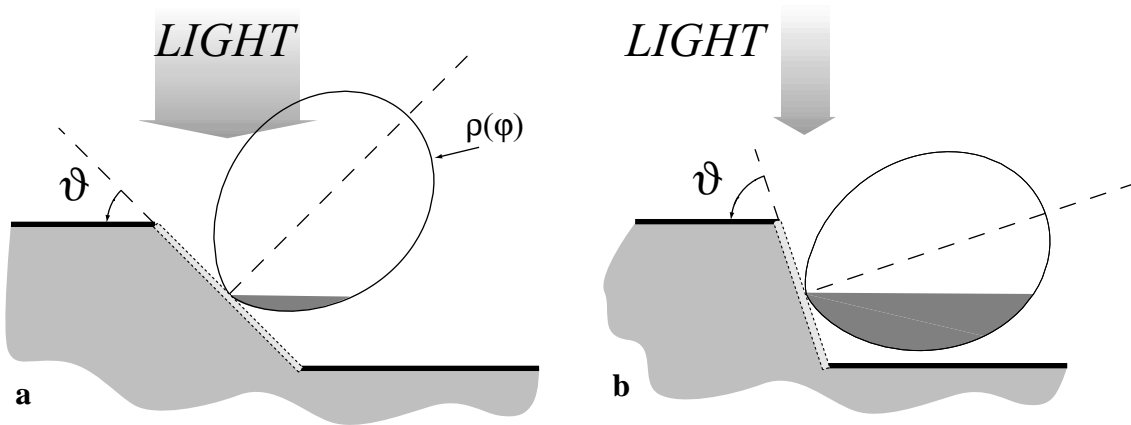


Figure IV.2-3: Scheme of ramp ablation, showing why direct redeposition on the channel floor is more important at high ramp angles ϑ . An angular density distribution of the ejected particles $\rho(\varphi) = \rho_0 \times \cos(\varphi)^2$ is given in polar representation (curved line). The surface of the filled part of the curved line is proportional to the quantity of material, which would be ejected directly in the direction of the channel floor of a long channel. At high ramp angles (b) much more material is redeposited directly in the channel than at low ramp angles (a).

The total debris deposition in Scanning Ablation is a mixture of *direct* and *indirect redeposition*.

V. Structure changes due to Scanning Ablation

V.1 Static Ablation

The Static Structure develops only in stretched substrates. In uniaxially stretched substrates, the main orientation of the resulting Wall-Type Structure is perpendicular to the stretching direction. In biaxially stretched substrates a Nap-type Structure develops [56]. In our biaxially stretched standard PET samples, where the extent of stretching is different for the two stretching directions, a superposition of Nap- and Wall-type Structure is observed. The resulting structure has a mountain chain like shape. The Static Structure formation in PEN upon Laser Ablation is very similar to the one in PET [40]. At the usual irradiation conditions in this work, the period of the Static Structure is approximately $3\ \mu\text{m}$, and its height approximately $2\ \mu\text{m}$.

In this section, the specific appearances of the Static Structure found after Static Ablation of the used substrates will be shown by SEM, AFM, and TEM, in order to serve as a reference for the observations in the following sections.

V.1.1 Unstretched PET

Laser Ablation of unstretched PET at a laser wavelength of 193 nm with relatively high fluences ($75\ \text{mJ}/\text{cm}^2$ - $1200\ \text{mJ}/\text{cm}^2$) leads to smooth etched surfaces, as reported in detail in section II.2.2 [56]. An example of an ablated hole in amorphous unstretched PET is given in Figure V.1-1a. Only slight ripples close to the walls can be observed, which are due to diffraction and/or reflection at the borders.

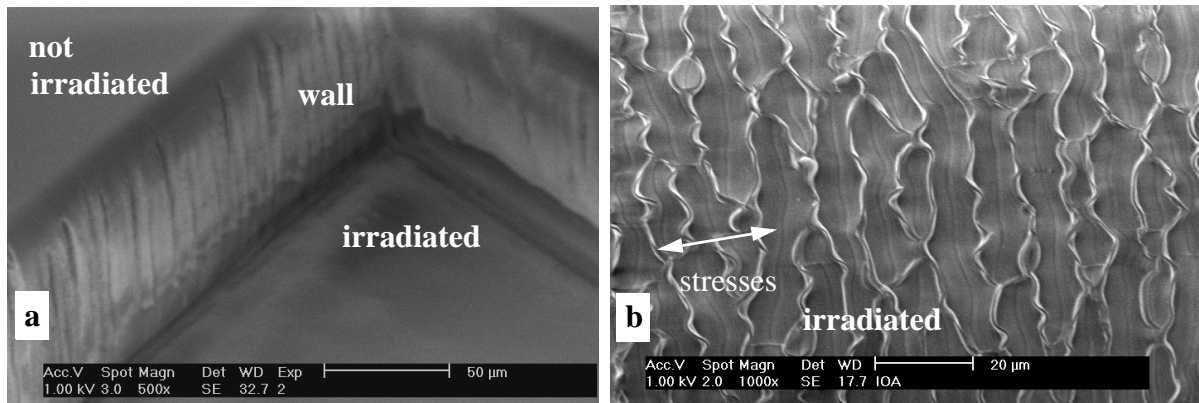


Figure V.1-1: (a) Ablated structure in unstretched amorphous PET ($n = 1000$ pulses and $\Phi = 1200\ \text{mJ}/\text{cm}^2$, SEM observation under 30° tilt angle). By SEM no micrometric structure, except diffraction fringes at the borders are observable on the ablated surface. (b) SEM image of the Static Structure observed on the same material as in (a) after uniaxial stretching. The irradiation was performed with $n = 200$ pulses and $\Phi = 1000\ \text{mJ}/\text{cm}^2$.

V.1.2 Uniaxially stretched PET

As reported in section II.2.2, the frozen stresses in the material are the key factor for the understanding of the shape and orientation of the Static Structure [56]. For some experiments, we used self made uniaxially stretched samples (section III.3.2). The Static Structure developing after the standard irradiation ($n = 200$, $\Phi = 1000 \text{ mJ/cm}^2$) was investigated by SEM (Figure V.1-1b). As expected, the samples show a Wall-like Structure, with the main orientation of the walls perpendicular to the stretching direction.

V.1.3 Biaxially stretched PET

The Static Structure of the biaxially stretched PET samples was a mixture of the Wall-type Structure (section II.2.2) and the Nap-type Structure (section II.2.2), because the films were biaxially stretched but the extend of the stretching was not the same in the two directions. This leads to a mountain chain like structure where the naps (mountains) are aligned preferentially perpendicularly to the main stretching direction. This can be seen in Figure V.1-2a. At lower fluences a pure Nap-type Structure develops at $n = 200$ shots per site (Figure V.1-2b).

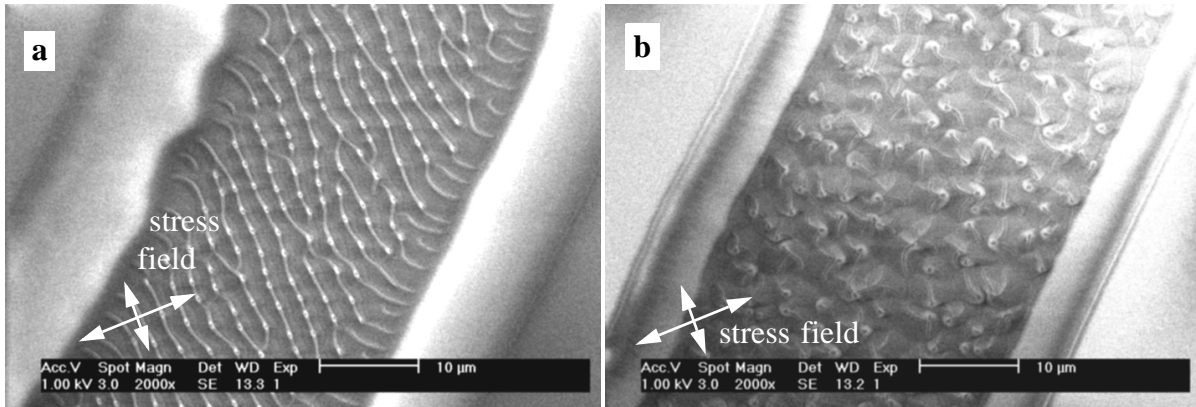


Figure V.1-2: SEM micrographs of the Static Structure in the biaxially stretched standard samples. **(a)** Mountain chain like structure. The white dots are the tops of the naps ($\Phi = 1200 \text{ mJ/cm}^2$, $n = 200$). **(b)** Typical Nap-type Structure ($\Phi = 75 \text{ mJ/cm}^2$, $n = 200$).

The AFM picture in Figure V.1-3a and the TEM of a cross section of the channel floor in Figure V.1-3b give a more detailed and quantitative view of the Static Structure shown in Figure V.1-2a. As the AFM tip geometry limits the lateral resolution, when imaging high aspect ratio structures, the sub-micrometric dimensions of the nap tips are only visible in the TEM picture (Figure V.1-3b). As reported in section II.2.2, the amplitude and the period of the structure depend on fluence and number of shots per site. For the usual irradiation conditions, the period of the structure ranges from 2 to 5 μm (Figure V.1-2a and Figure V.1-1a), whereas the amplitude of the structure ranges from 1 to 3 μm (Figure V.1-3a and b). The tip of the naps or mountains is about the same height as the base or even higher (Figure V.1-3b).

The two key experiments for the structure formation, which are already described in literature [56,58], were also repeated:

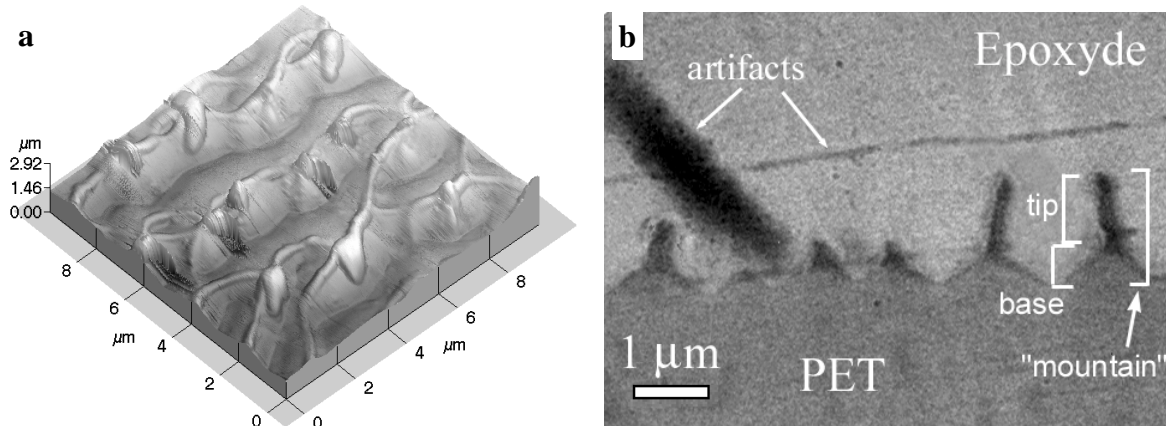


Figure V.1-3: (a) AFM and (b) cross sectional TEM of the Static Structure in the biaxially stretched standard samples. (Parameters: (a) $\Phi = 1200 \text{ mJ/cm}^2$, $n = 50$, and (b) $\Phi = 1200 \text{ mJ/cm}^2$, $n = 200$.)

1. In order to verify that the orientation of the Static Structure is really given by the orientation of the stresses and not by the orientation of the channel, channels in different directions with respect to the main stress direction were ablated [56].
2. In order to verify that the Static Structure does not change significantly with the angle of light incidence in the range from 0° to 70° [58], a Static Ablation with an angle of light incidence of 45° was carried out (Figure III.1-3).

In both cases, the results from the literature reports were confirmed.

V.1.4 Biaxially stretched PEN

The behavior of PEN upon Laser Ablation is similar to the one of PET (section II.2.2). In the case of the used biaxially stretched PEN films the stretching strength in the two directions was approximately the same, because a pure Nap-type Structure was observed after Static Ablation, both with high and low fluence (Figure V.1-4).

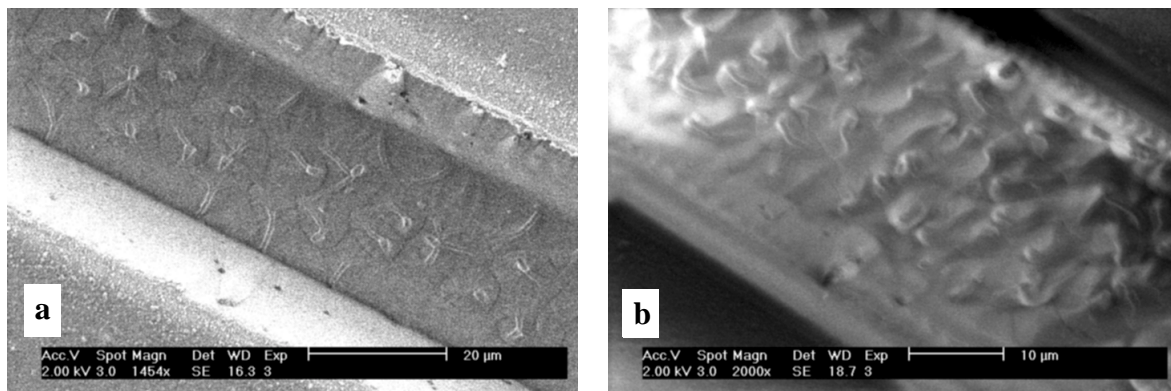


Figure V.1-4: SEM micrographs of the Static Structure in biaxially stretched PEN samples. At high and low fluence a typical Nap-type Structure develops. Parameters: (a) $\Phi = 1100 \text{ mJ/cm}^2$, $n = 200$, and (b) $\Phi = 150 \text{ mJ/cm}^2$, $n = 200$

V.2 Ramp ablation and Scanning Ablation

The structure on ablated ramps in stretched polymers depends on the ramp angle, the orientation of the ramp with respect to the stretching direction, and the fabrication mode. For fabrication modes, where the whole ramp is never irradiated, no differences compared to Static Ablation could be observed. For fabrication modes, where the whole ramp is irradiated, the structure is the same as in Static Ablation, as long as the ramp angle is lower than approximately 10° . Depending on the relative orientation of the ramp and the stretching direction, the structure formation is partially or completely suppressed at higher ramp angles. Vector decomposition of the stress in the polymer allows for a consistent description of all observed effects. The limiting angles between the three possible structures (Static Structure, Scanning Structure and Smooth Structure) depend neither on the extend of stretching, nor on the laser fluence, but they are different for different polymers.

V.2.1 Suppression of the structure formation

In 1998, we observed structure changes on ramps, that were ablated in biaxially stretched PET films (section V.2.2) [8]. At ramp angles above a certain limiting angle ϑ' , the orientation of the Static Structure changed and the naps disappeared, and above a second limiting angle ϑ'' , the ramps got completely smooth. The effect could only be observed on ramps, where the whole inclined surface is illuminated, i.e. the end ramp in Scanning Ablation as well as ramps, which are produced by Opening Mask Ablation or Grey-level Mask Ablation (walls: Figure V.2-3c). This suppression of the Static Structure formation can be understood, when assuming that the *relaxation* of the frozen stresses S in a stretched polymer sample obeys the laws of vector addition [9]. We saw already in section V.1 that this assumption fails in case of the *building-up* of the frozen stresses by stretching: biaxial stretching of a polymer sample should be identical, according to vector addition, to uniaxial stretching in the diagonal direction, but the resulting Static structures, reflecting the stress fields in the polymer, are very different.

Nevertheless, the *decomposition* of the stress S in the polymer into different components S_\perp , S_p and S_a , during the *relaxation* of the stress, leads to a consistent description of the observations. Three experiments were carried out in PET, that was stretched uniaxially at room temperature (section III.3.2). In each of the experiments another orientation of the stresses S with respect to the ramp border was chosen (Figure V.2-1). In all cases ramps with different ramp angles ϑ were ablated by Opening Mask Ablation, and the structure on the ramps was observed by SEM.

Experiment 1: The stresses were oriented perpendicularly to the ramp border, i.e. in the direction of the ramp (Figure V.2-1 left side). Ramps with the ramp angles listed in Table V.2-1 were ablated. SEM pictures of three of the nine different ramp inclinations are shown in Figure V.2-2.

At ramp angles of less than 11° the Static Structure formed, exactly as in Static Ablation (Figure V.2-2a). At a ramp angle of $\vartheta = \vartheta' \equiv 11^\circ$ the structure formation was suppressed, although a slight texture was still visible on the ramp (Figure V.2-2b). At ramp angles of more than 11° the ramps were completely smooth (Figure V.2-2c).

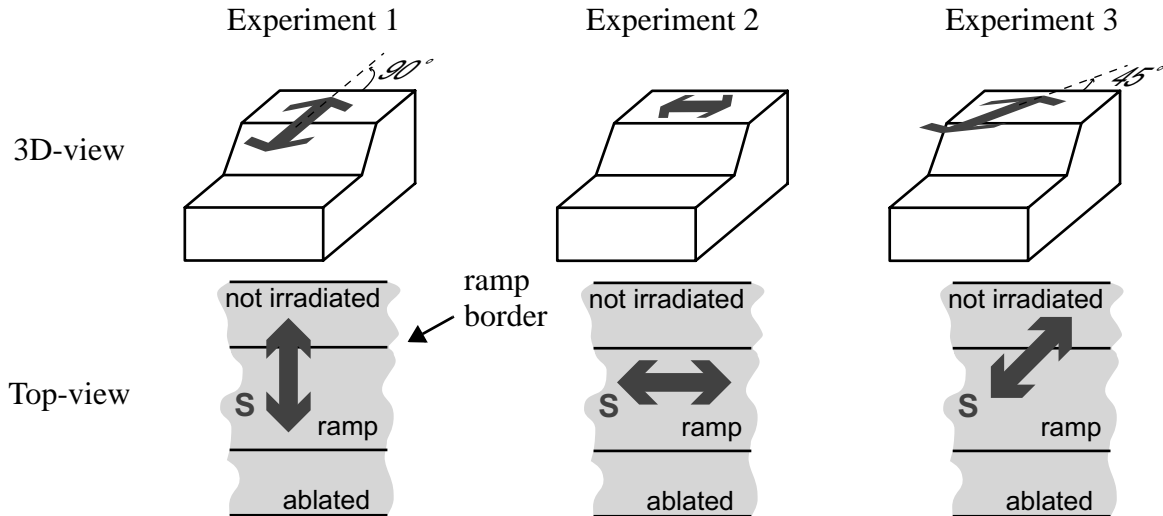


Figure V.2-1: Schematic of the relative orientations of frozen stress S and ramp border in experiments 1 to 3.

a (μm)	1000	500	200	150	100	75	50	30	wall
ϑ ($^\circ$)	2.2	4.3	11	14	21	27	37	52	> 70

Table V.2-1: List of different spot lengths a and ramp angles ϑ used in experiment 1. Fluence was $\Phi = 1000 \text{ mJ/cm}^2$ and number of shots $n = 200$ for all ramps.

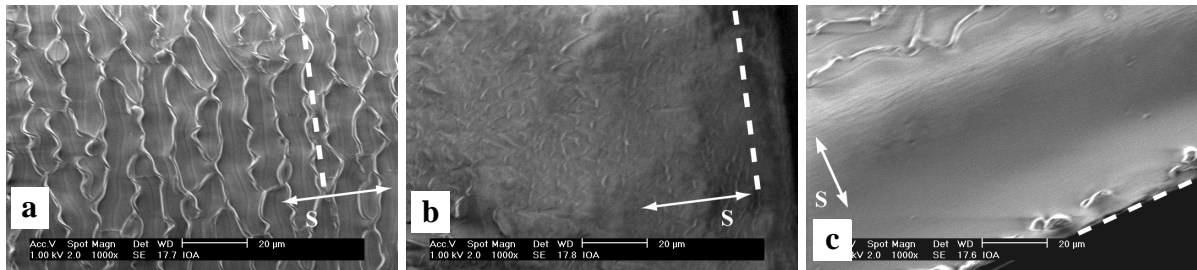


Figure V.2-2: SEM micrographs of the ablated ramps (top-view). The dashed line indicates the direction of the ramp border. Parameters: (a) $\vartheta = 2.2^\circ$, (b) $\vartheta = 11^\circ$, (c) $\vartheta = 27^\circ$.

Experiment 2: The stresses were oriented parallel to the ramp border (Figure V.2-1 center). Ramps with the ramp angles listed in Table V.2-2 were ablated. Figure V.2-3 shows SEM micrographs of three of the ten different ramp angles.

a (μm)	1000	500	200	150	100	75	50	30	15	wall
ϑ ($^\circ$)	2.2	4.3	11	14	21	27	37	52	69	> 70

Table V.2-2: List of different spot lengths a and ramp angles ϑ used in experiment 2. Fluence was $\Phi = 1000 \text{ mJ/cm}^2$ and number of shots $n = 200$ for all ramps.

No suppression of the Static Structure formation was observed, even at high ramp angles. In fact the Static Structure could even be observed on the walls of the ablated structure (Figure V.2-3c).

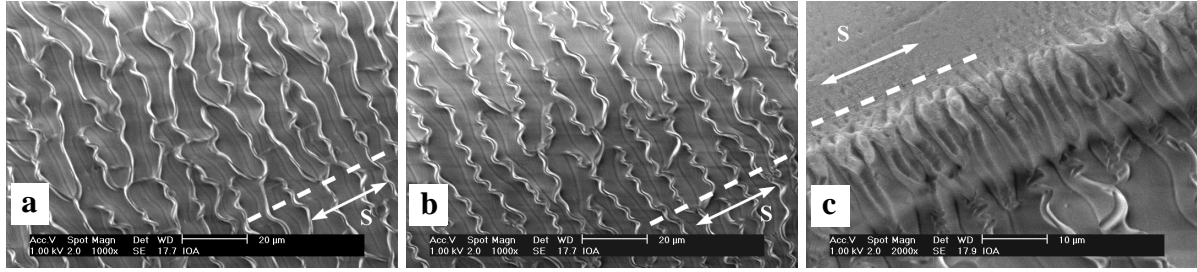


Figure V.2-3: SEM micrographs of the ablated ramps (top-view). The dashed line indicates the direction of the ramp border. Parameters: (a) $\vartheta = 2.2^\circ$, (b) $\vartheta = 11^\circ$, (c) $\vartheta > 70^\circ$.

Experiment 3: The stresses were oriented at an angle of 45° to the ramp border (Figure V.2-1 right side). Ramps with the ramp angles listed in Table V.2-3 were ablated. The SEM pictures of three of the ten produced ramps with different inclinations are shown in Figure V.2-4.

a (μm)	1000	500	200	150	100	75	50	30	15	wall
ϑ ($^\circ$)	2.2	4.3	11	14	21	27	37	52	69	> 70

Table V.2-3: List of different spot lengths a and ramp angles ϑ used in experiment 2. Fluence was $\Phi = 1000 \text{ mJ/cm}^2$ and number of shots $n = 200$ for all ramps.

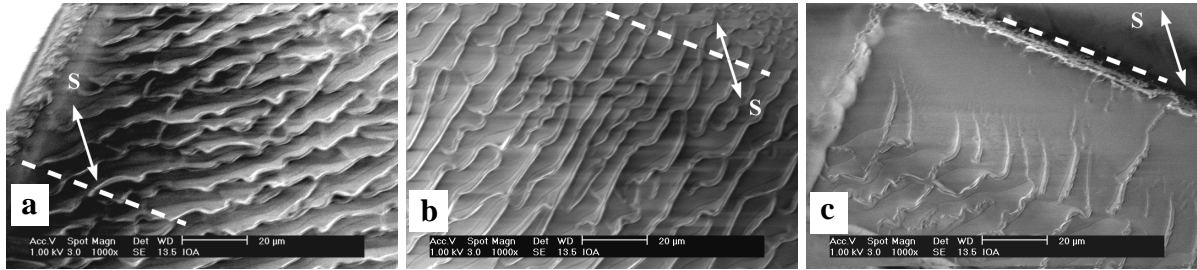


Figure V.2-4: SEM micrographs of the ablated ramps (top-view). The dashed line indicates the direction of the ramp border. Parameters: (a) $\vartheta = 2.2^\circ$, (b) $\vartheta = 11^\circ$, (c) $\vartheta = 37^\circ$.

At ramp angles lower than $\vartheta' = 11^\circ$ the Static Structure developed, as in Static Ablation, perpendicularly to the frozen stresses (Figure V.2-4a). At ramp angles ϑ , with $\vartheta' \leq \vartheta \leq 30^\circ \equiv \vartheta''$, the structure was aligned with the ramp direction and no longer perpendicular to the stress direction (Figure V.2-4b). At high ramp angles $\vartheta > \vartheta''$, the structure formation was suppressed (Figure V.2-4c).

Conclusions from experiment 1-3: Only in experiment 2, the stress S is tangential to the ramp at all ramp angles ($S = S_a$ according to Figure V.2-5 and Figure V.2-1). In this case, S is active for the formation of the Static Structure at all ramp angles. In experiment 1, S becomes inactive for the Static Structure formation at $\vartheta \geq \vartheta'$. This explains also the change in structure orientation, which is observed in experiment 3 at $\vartheta \geq \vartheta'$. It is sufficient to decompose S into a component S_a parallel to the ramp border and a component S_i in the ramp direction (Figure V.2-5a). When considering S_i becoming inactive for structure formation at $\vartheta \geq \vartheta'$, we end up with a

structure being determined by S_a and thus oriented in the direction of the ramp, as it was observed (Figure V.2-4b).

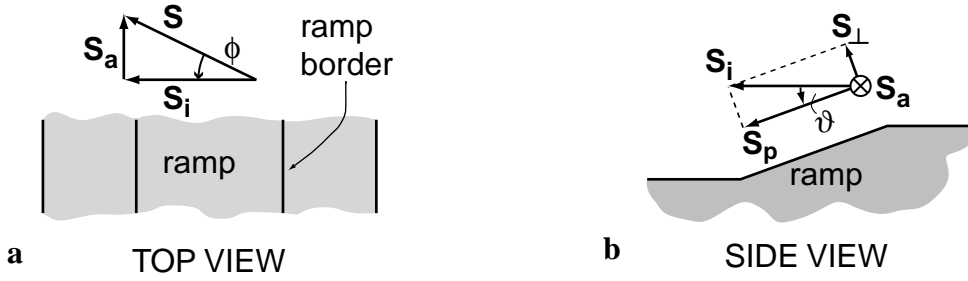


Figure V.2-5: Decomposition of the stress vector S into components parallel and perpendicular to the irradiated surface. (a) Top view, and (b) side view of the ramp. S_a and S_p are parallel to the irradiated surface and S_{\perp} is perpendicular to it. It is $S_a + S_p + S_{\perp} = S$.

The decomposition of S into S_a and S_i is not yet adapted to the problem, because an instable surface (as the polymer surface during the laser pulse) reacts differently on stresses, which are perpendicular to the surface, compared to stresses being tangential to it. Figure V.2-5b defines the decomposition of S_i in its components S_p , parallel to the irradiated surface, and S_{\perp} , perpendicular to it. The adapted coordinate system for the description of the problem is composed by S_a , S_p and S_{\perp} (Figure V.2-5b).

Comparing experiment 2 with experiment 1 and 3, it is clear that $S_{\perp} \neq 0$ needs to be fulfilled for any structure change to occur. In other words, the stress component S_{\perp} , which is perpendicular to the irradiated surface, suppresses the structure formation. With increasing ϑ , first, i.e. from $\vartheta \approx \vartheta'$ on, the stress component S_p , which is parallel to the ramp and in the ramp direction, is rendered inactive for structure formation by the influence of S_{\perp} . Then, from $\vartheta \approx \vartheta''$ on, also the stress component S_a , which is parallel to the ramp and in the direction of the ramp border, is no longer active for structure formation due to S_{\perp} .

Experiment 4: However, it is not yet clear whether the threshold in S_{\perp} which causes the suppression of the Static Structure formation is an absolute or a relative threshold. In an attempt to answer this question, we determined the first limiting angle ϑ' in substrates, which were stretched to different draw ratios DR (section III.3.2). All ramps were ablated in the sensitive configuration with the direction of the stresses and the ramp direction aligned ($S = S_i$). The results of this experiment are summarized in Table V.2-4.

Draw ratio (DR)	1, 1.5	2, 2.5, 3, 4
Limiting angle ϑ'	no structure formation at all	13 (± 0.8)°

Table V.2-4: Results of experiment 4, using the samples that were stretched to different draw ratios at a temperature between the glass transition temperature and below the melting temperature of PET (section III.3.2).

Conclusions from experiment 4: The first result, that at $DR \leq 1.5$ no Static Structure formation occurs, just quantifies in some way the finding of Arenholz *et al.*, that sufficiently strong frozen stresses in the material are necessary in order to induce the Static Structure formation. However, giving a value and a unity for the structure formation threshold in the tangential stress ($S_p + S_a$) is not possible. The problem is to express the quantity *frozen stresses* S by means of polymer properties like the statistical description of the chain alignment, the degree of crystallinity, or the parameters of the rubber network model.

The samples of experiment 4 were prepared, as already mentioned, following a recipe of Chang *et al.*. Thus $\langle P_2 \cos \theta \rangle$, describing the polymer chain alignment as measured by birefringence, and the degree of crystallinity are known as a function of the draw ratio DR , according to their measurements (Figure V.2-6a and b). Additionally we measured the recovery ratio X of our samples. The recovery ratio X describes the extend to which a stretched polymer sample can recover its dimensions before stretching by thermal annealing below the melting temperature and is defined as $X = (l_s - l_a)/(l_s - l_o)$ [119]. Here, l_o is the length of the original unstretched sample, l_s is the sample length after stretching and l_a is the sample length after stretching and successive annealing. For the annealing experiment the samples were kept for 5 h at the same temperature as during stretching, i.e. 80°C , and quenched afterwards to 23°C in order to avoid crystallization, which would cause brittleness. We measured the value of the relative retraction $RR = l_s/l_a$ and determined the recovery ratio X by Eq. 17.

$$X = DR \times \left(\frac{1 - 1/RR}{DR - 1} \right) \quad (17)$$

The plot X vs. DR is shown in Figure V.2-6c.

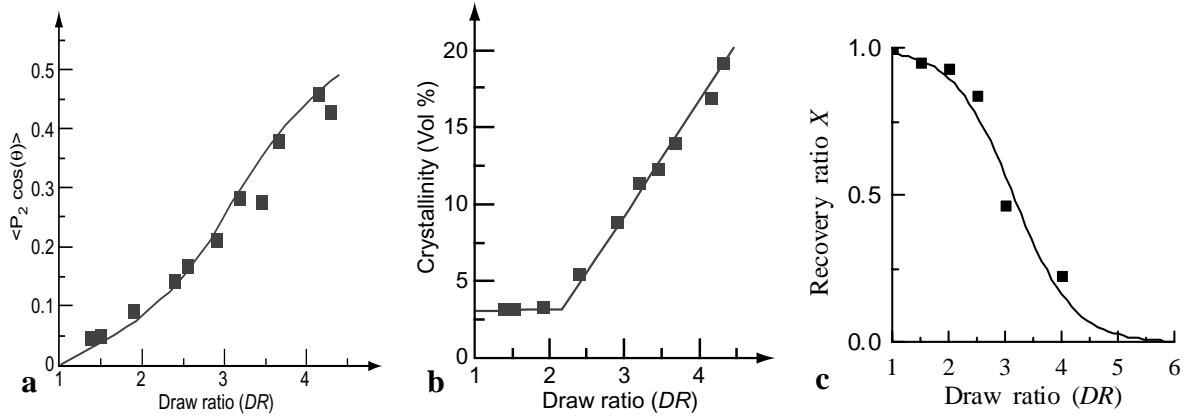


Figure V.2-6: (a) Plot of the chain alignment parameter $\langle P_2 \cos \theta \rangle$ vs. the draw ratio DR [117]. (b) Plot of the crystallinity vs. the draw ratio DR [117]. (c) Plot of the recovery ratio X vs the draw ratio DR .

Thus, we know that the chain orientation $\langle P_2 \cos \theta \rangle$ in our samples increases monotonously, but it is not clear, if the frozen stress S does so. (Defining S as the quantity that is responsible for the structure formation upon Laser Ablation.) Arguments for a saturation of S at $DR > 2$ are the orientation induced enhancement of the degree of crystallization (Figure V.2-6b), and the decrease of the recovery ratio (Figure V.2-6c). S is most probably related to the orientation of

polymer chains in amorphous domains. The formation of new crystallites, as well as the growth of existing crystallites, both reduce the average length of the chains in the amorphous domains of the polymer. In consequence the capacity of the polymer to recover its shape before stretching decreases. One could then imagine that upon stretching, from draw ratio 2.2 to some higher value all further alignment of the chains leads to their crystallization and can in consequence not be relaxed upon laser irradiation. On the other hand, Bahners *et al.* brought experimental evidence against a saturation of S by measuring a difference in the period of the static structure for fibers with $DR = 2.8$ and $DR = 4.2$, if they used more than 5 pulses [55]. This difference can only be explained, if the frozen stresses in the two samples are different. For this reason, Kesting *et al.* relate the frozen stress S with the orientation of the molecules $\langle P_2 \cos \theta \rangle$ [65].

The constancy of ϑ' for $DR \geq 2$ thus indicates the magnitude of S_{\perp} , that is required for the suppression of the structure formation, relative to the magnitude of S_p . The relative suppression threshold for S_p evaluates to

$$|S_{\perp}|/|S_p| \geq \tan(\vartheta') \approx 0.23. \quad (18)$$

With the data of experiment 3, such a relative suppression threshold can be calculated analogously for S_a .

$$|S_{\perp}|/|S_a| \geq \frac{\sin(\vartheta'')}{\tan(\phi)} \approx 0.5, \quad \phi = 45^\circ \quad (19)$$

It is however necessary to emphasize the importance of the heating induced stress for the structure formation, which is not included in the above considerations [59].

Finally, we can say that the structure formation threshold in the tangential stress is reached for PET only at draw ratios higher than 1.5. Moreover, a relative threshold in the perpendicular stress S_{\perp} with respect to the tangential stresses S_p and S_a can be given, from where on S_{\perp} renders the tangential stresses inactive for structure formation.

Summary In this subsection different structures on ramps ablated in uniaxially stretched PET were presented. The observed structure changes can be understood as a step wise suppression of the structure formation, due to the stress component S_{\perp} , which is perpendicular to the ramp. The relative suppression thresholds, perpendicular stress divided by tangential stress, are different for the two different directions of tangential stress (S_p and S_a). Moreover, the structure generation threshold in tangential stress is reached in PET only at draw ratios higher than 1.5.

V.2.2 The general case

As already mentioned, the suppression of the structure formation occurs also on biaxially stretched samples. The samples are biaxially stretched, and the extent of stretching is different in the two directions. The mountain chain like structure, resulting from Static Ablation, was already described in section V.1.3. The structure changes, found on ablated ramps in this substrate, are very similar to those in the uniaxially stretched substrates with a 45° angle between the stress and the ramp border (Experiment 3). Figure V.2-7 shows SEM micrographs of the three structure types that were observed [8].

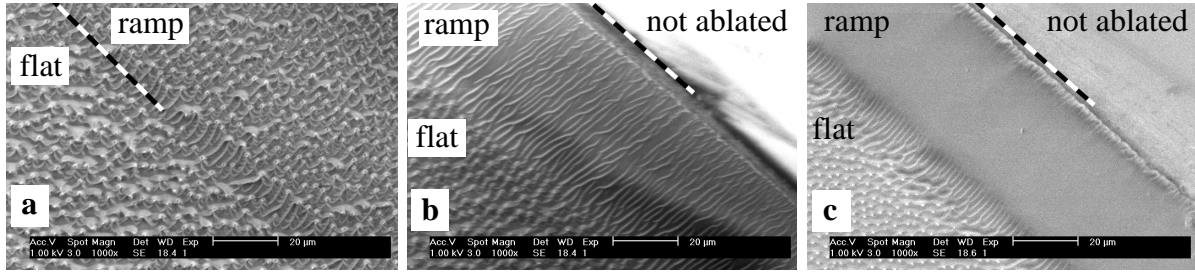


Figure V.2-7: SEM micrographs of ramps, ablated in the biaxially stretched PET substrate by Opening Mask Ablation. The dashed line indicates the direction of the ramp border. Parameters: **(a)** $\vartheta < \vartheta'$ ($\Phi = 290 \text{ mJ/cm}^2$, $a = 200 \text{ }\mu\text{m}$, $n = 200$); **(b)** $\vartheta' \leq \vartheta < \vartheta''$, ($\Phi = 290 \text{ mJ/cm}^2$, $a = 50 \text{ }\mu\text{m}$, $n = 200$); **(c)** $\vartheta > \vartheta''$, ($\Phi = 1000 \text{ mJ/cm}^2$, $a = 50 \text{ }\mu\text{m}$, $n = 200$).

The structures can now easily be understood by taking into account that for $\vartheta' \leq \vartheta < \vartheta''$ only the component S_a of the stresses in the material is active for structure formation. This means that in this range of ramp angles, we have the same situation as in a uniaxially stretched substrate with the stresses oriented in the direction of the ramp border. In consequence, the naps, usually characterizing biaxially stretched substrates, disappear, and the orientation of the structure, normally determined by the main stretching direction, aligns with the ramp direction (Figure V.2-7b). The structure with these characteristics, appearing at ramp angles between ϑ' and ϑ'' , was named *Scanning Structure* [7]. This name will be used from now on, even if it is clear now, that the *Scanning Structure* is just a *Static Structure*, where a part of the frozen stresses in the material is no longer active for structure formation.

At ramp angles $\vartheta \geq \vartheta''$, the component S_{\perp} of the stresses, being perpendicular to the irradiated surface, suppresses the structure formation completely. This leads to the smooth ablation of stretched PET as shown in Figure V.2-7c.

The angles, ϑ' and ϑ'' , at which the structure changes occur, are known more precisely for this substrate, because we produced ramps with different spot lengths at different fluences and also with two methods, i.e. Scanning Ablation and Opening Mask Ablation. Figure V.2-8 shows a map of the parameter space $\{a, \Phi\}$, where all ramps are marked according to their structure and production method with a different symbol. All samples with the same structure are located in a distinct range of ramp angles and the production method does not influence this. Thus, the major results of these experiments are, that ϑ' and ϑ'' do not depend on the fluence, and that the observations are identical for Scanning Ablation and for Opening Mask Ablation.

The values of the limiting angles that were determined indirectly and directly (section III.1.5) were slightly different. Most probably due to errors in the determination of the ablation curve and/or errors in the determination of the fluence in the indirect determination of the ramp angles. The values for the biaxially stretched PET standard substrate are listed in Table V.2-5.

V.2.3 Material dependence of the limiting angles

When comparing the value for ϑ' in Table V.2-5 ($10.5 \pm 0.2^\circ$) with the one in Table V.2-4 ($13 \pm 0.8^\circ$), it is evident that the deviation is bigger than the error in the measurement. However, the corresponding experiments were carried out in different PET substrates. In order to see whether

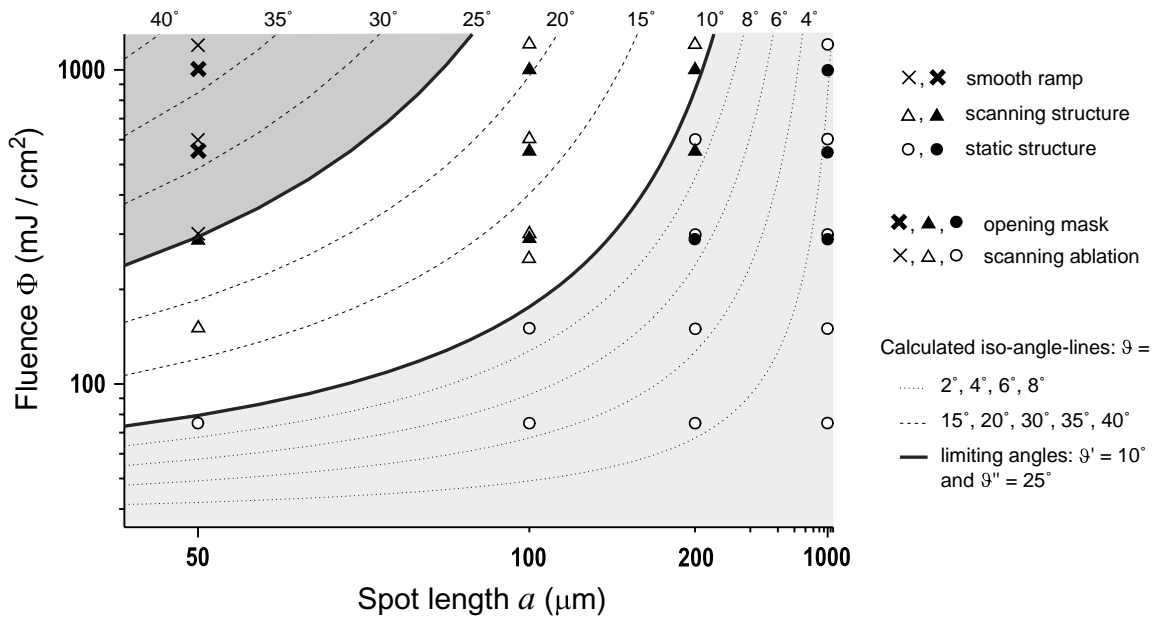


Figure V.2-8: All ramps ablated in the standard PET substrate are marked in this map of parameter space $\{a, \Phi\}$. Bold/filled symbols indicate Opening Mask Ablation, plain/open symbols stand for Scanning Ablation. The form of the symbol gives the observed structure: Circles correspond to the *Static Structure*, triangles to the *Scanning Structure* and crosses to *smooth ramps*. The lines indicate the combinations of a and Φ resulting in the same ramp angle. The limiting angles ϑ' and ϑ'' are indicated by bold lines.

	ϑ'	ϑ''
Indirect method	$10(\pm 0.5)^\circ$	$25(\pm 0.5)^\circ$
Direct method	$10.5(\pm 0.2)^\circ$	not measured

Table V.2-5: Values of the limiting angles for the standard PET substrate, and comparison of the indirect and direct angle determination methods described in section III.1.5.

the limiting angle is really material dependent, the same experiments as with the standard PET substrate were carried out in commercial, biaxially stretched PEN. In the case of PEN only Scanning Ablation was used for ramp production. The map of the samples in parameter space $\{a, \Phi\}$ is shown in Figure V.2-9.

The limiting angles in PEN evaluate to $\vartheta' = 7.7(\pm 1.0)^\circ$ and $\vartheta'' = 20(\pm 1.6)^\circ$ as determined by the indirect method. Table V.2-6 allows for a better comparison of the values obtained in the three different substrates.

There is clearly a dependence of the limiting angles on the substrate material, but, based on the available data, it is impossible to separate the influences of the different material properties. The problem is, that polymer stretching influences the crystallinity, hence also the absorption coefficient [63] and the heat diffusion coefficient [113], as well as the Youngs modulus [65] at the same time. When comparing PET and PEN, not only these parameters change, but additionally

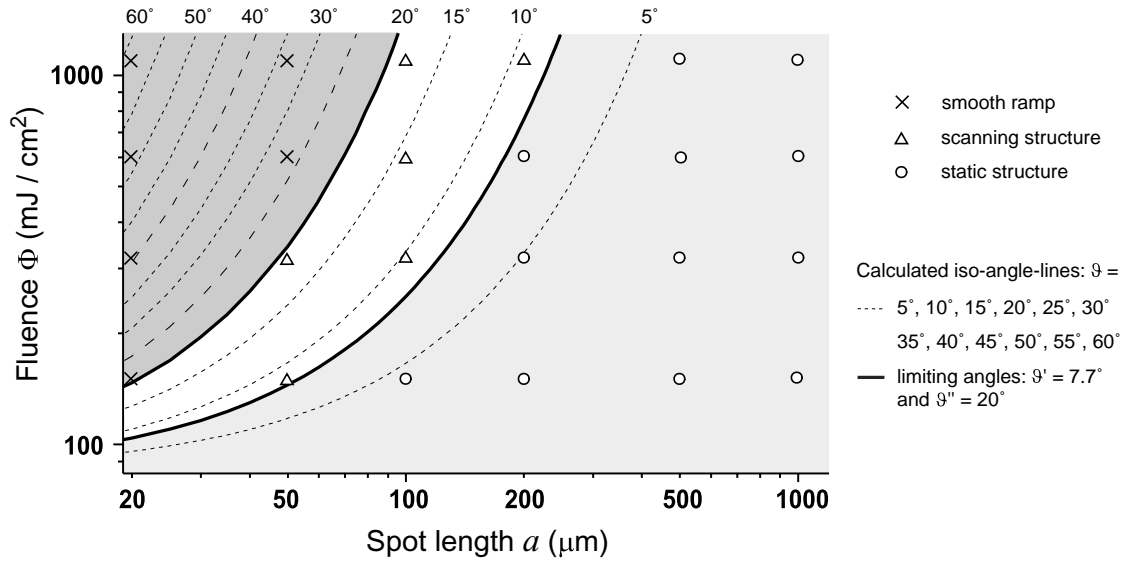


Figure V.2-9: All ramps ablated in the PEN substrate are marked in this map of parameter space $\{a, \Phi\}$. The form of the symbol gives the observed structure: Circles correspond to the *Static Structure*, triangles to the *Scanning Structure* and crosses to *smooth ramps*. The lines indicate the combinations of a and Φ resulting in the same ramp angle. The limiting angles ϑ' and ϑ'' are indicated by bold lines. All ramps were prepared by Scanning Ablation.

	ϑ'	ϑ''
PET uniaxial 85°C	13(± 0.8)°	not measured
PET biaxial	10.5(± 0.2)°	25(± 0.5)°
PEN biaxial	7.7(± 1)°	20(± 1.6)°

Table V.2-6: Values of the limiting angles in the different substrate materials.

the two materials may have different chain mobilities, different crystallite sizes and different crystallization enthalpies. All these parameters probably influence the structure formation [59,61].

V.2.4 The structure on the beginning ramp

As already illustrated in section III.1.4, is also possible to ablate ramps without irradiating more than the lowest part of the ramp. This is the type of ramp, that forms at the beginning of a scanned channel or in Closing Mask Ablation. During the Laser Ablation of those non-irradiated ramps, only the flat surface near the lowest part of the ramp is irradiated. Therefore the part of the ramp formed by the preceding pulses is left untouched by the following one. This means that the whole ramp is never irradiated at once and the structure formation only takes place on flat surfaces. For an illustration of the mechanism forming the ramp see Figure III.1-6a or the left sides in Figure IV.1-1a to c.

With this formation mechanism in mind, it is not astonishing to find always the same type of structure as in Static Ablation on non-irradiated ramps. The only difference to Static Ablation is the debris contribution, which varies with the ramp angle. The debris contribution will be discussed in section V.4. For examples of beginning ramps after Scanning Ablation, see Figure V.2-10.

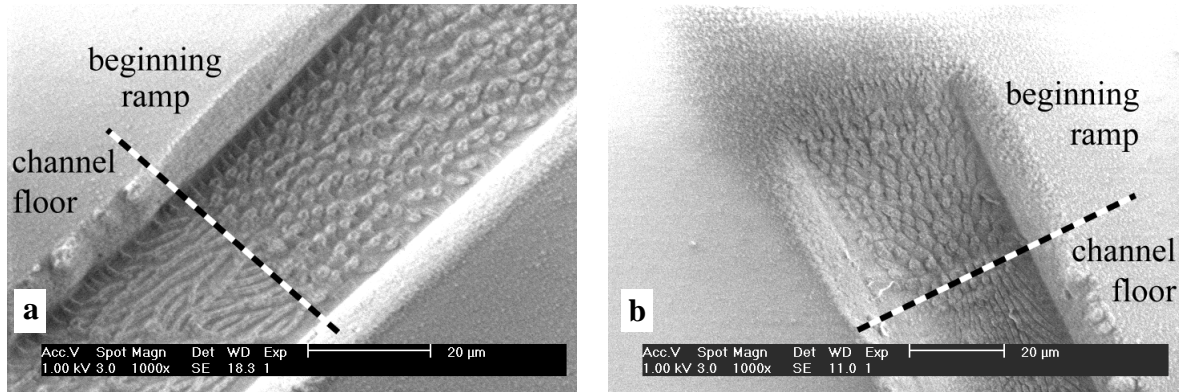


Figure V.2-10: SEM micrographs of non-irradiated ramps at the beginning of channels produced by Scanning Ablation. **(a)** Static type structure on the non-irradiated ramp with $\vartheta' \leq \vartheta < \vartheta''$. (At the same angle, a Wall-Type Structure (Scanning Structure) develops on the irradiated ramp.) Parameters: $\Phi = 250 \text{ mJ/cm}^2$, $a = 100 \text{ }\mu\text{m}$. **(b)** Static type structure on the non-irradiated ramp with an important debris contribution $\vartheta > \vartheta''$ (smooth irradiated ramp) Parameters: $\Phi = 300 \text{ mJ/cm}^2$, $a = 50 \text{ }\mu\text{m}$.

V.3 The channel floor

The micrometric structure on the channel floor is the same as on the irradiated ramp, with the exception that the channel floor cannot become completely smooth. A nanometric structure is added at high ramp angles, because of the direct redeposition of important amounts of debris.

For the application of Scanning Ablation to micro fluidic channel production, the structure on the ramps is not very interesting, because the ramps do not exist in the final device (Figure III.4-2a), or they are in dead ends of the device (Figure III.4-2b). Nevertheless, the end ramp is the only irradiated surface in Scanning Ablation (Figure III.1-4b), and thus determines the structure on the channel floor.

If the structure on the end ramp is of the “static” type or of the “scanning” type the structure on the channel floor is the same as the one on the end ramp (Figure V.3-1a and b). In the case of a smooth end ramp, the channel floor does however not become completely smooth (Figure V.3-1c). A kind of Scanning Structure is obtained for these high ramp angles on the channel floor. This is probably due to the structure formation on the lower corner of the ramp, which is smoothed, because of the limited optical resolution of the mask projection. In consequence, there is a small region where the local ramp angle is less than ϑ'' and there is still enough light intensity to cause stress relaxation.

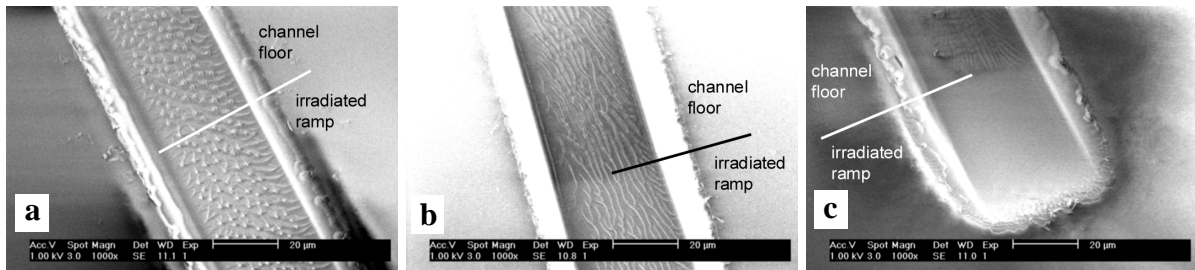


Figure V.3-1: (a) $\vartheta < \vartheta'$ Static Structure on the irradiated ramp, and Static Structure on the channel floor ($\Phi = 300 \text{ mJ/cm}^2$, $a = 200 \mu\text{m}$). (b) $\vartheta' \leq \vartheta < \vartheta''$ Scanning Structure on the irradiated ramp and Scanning Structure on the channel floor ($\Phi = 600 \text{ mJ/cm}^2$, $a = 100 \mu\text{m}$). (c) $\vartheta > \vartheta''$ Smooth end ramp and Scanning Structure on the channel floor ($\Phi = 600 \text{ mJ/cm}^2$, $a = 50 \mu\text{m}$).

The SEM pictures in Figure V.3-1 show the part of the channel floor, which is next to the end ramp, without visible debris. Figure V.3-2 shows the structures that can be observed far away from the irradiated ramp on the channel floor in the three different ranges of ramp angles. In the case of Figure V.3-2c the micrometric structure is nearly hidden by the debris. The debris contribution, increasing from Figure V.3-2a to c, will be discussed in section V.4.

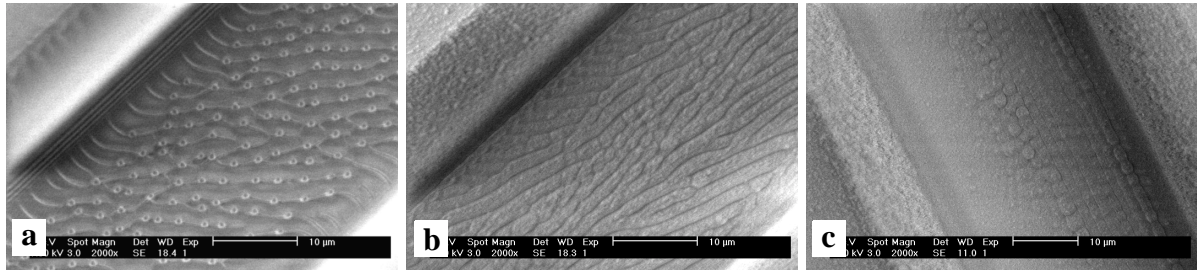


Figure V.3-2: Typical structures on the channel floor. **(a)** $\vartheta < \vartheta'$ Static Structure on the channel floor ($\Phi = 1200 \text{ mJ/cm}^2$, $a = 1000 \mu\text{m}$). **(b)** $\vartheta' \leq \vartheta < \vartheta''$ Scanning Structure on the channel floor ($\Phi = 1200 \text{ mJ/cm}^2$, $a = 100 \mu\text{m}$). **(c)** $\vartheta > \vartheta''$ slightly rough channel floor because of a hidden Scanning Structure ($\Phi = 1200 \text{ mJ/cm}^2$, $a = 50 \mu\text{m}$).

V.4 The debris contribution

In Scanning Ablation, debris adds a nanometer scale surface roughness on the channel floor and the channel walls. This debris contribution to the surface structure, which is principally caused by direct debris redeposition, can be quite important and is directly observable by SEM. Rinsing the channels with pressure driven flow and electroosmotic flow does not remove the debris. A gradient of debris exists on the first 0.6 mm near the irradiated ramp in Scanning Ablation, resulting from the “projection range” of indirect debris. In Static Ablation, the debris causes no measurable modification of the surface structure in the channel. Observation of debris near a statically ablated PET surface is partially possible by optical microscopy. Charging SEM pictures give a good view of the shape of the zone where debris redeposition occurs, and AFM allows for detailed knowledge on the debris caused roughness on flat surfaces.

V.4.1 Debris in Static Ablation

As described in section II.3.2 the redeposition of debris upon Static Ablation is quite well understood and already described in literature. In this section, some of the reproduced results are shown and possible observation methods are compared.

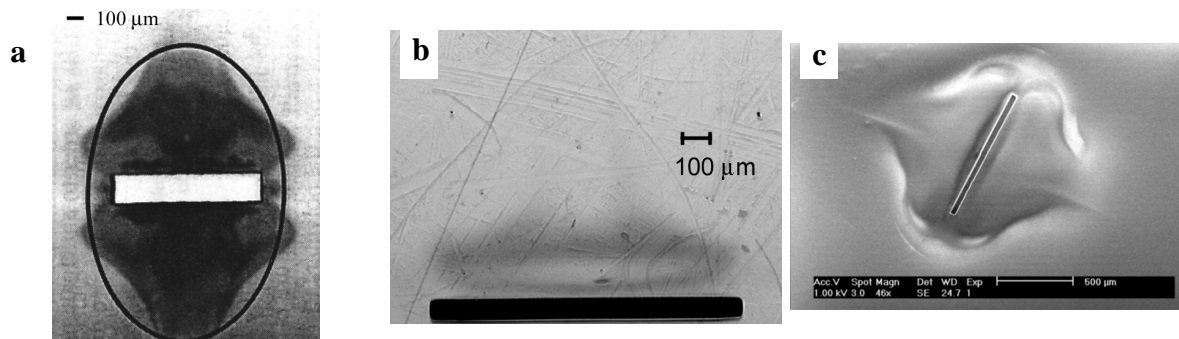


Figure V.4-1: Images of debris patterns near statically ablated surfaces. **(a)** Optical microscope image of a through drilled hole in polyimide [85]. **(b)** Optical microscope image of a standard Static Ablation in PET (Parameters: $\Phi = 1000 \text{ mJ/cm}^2$, $n = 200$, $1000 \times 50 \mu\text{m}^2$). **(c)** Charging contrast SEM image of an ablation comparable to (b) (Parameters: PET, $\Phi = 1200 \text{ mJ/cm}^2$, $n = 200$, $1000 \times 40 \mu\text{m}^2$).

Figure V.4-1 shows a comparison of a SEM image and an optical microscope image of the debris pattern around a surface, which was ablated statically. It is visible, that due to charging of the sample in the SEM, the shape of the debris pattern can be easily detected. In optical microscopy only the main debris humps near the longer sides of the ablated rectangle are visible (Zeiss Epiplan HD objective with integrated dark field illumination). However, without the charging effect, such a small quantity of debris is practically not detectable by SEM (Figure V.3-2a). Atomic Force Microscopy (AFM) is a good tool for detailed analysis of the surface roughness, which is caused by debris (Figure VI.2-3). For PET, it would be exaggerated to speak of a debris contribution to the *structure* of the ablated surface itself during Static Ablation. This, because only the indirect debris of one shot adds roughness to the irradiated surface at our irradiation

conditions. Other polymers like PI show more important indirect redeposition upon Static Ablation (section II.3.2). Depending on the ablation parameters, debris may nevertheless influence the surface structure after Static Ablation by cone formation (section II.2.2). This happens preferentially at relatively low fluences Φ and high pulse numbers n . Figure V.4-2a shows an example of cone formation in PET.

As mentioned before (sections II.3.2, IV.2.1), the indirect redeposition upon Static Ablation only takes place if collisions with the surrounding gas environment are possible. When ablating in vacuum no redeposition of debris is observed. Figure V.4-2b and c show the results for Static Ablation (1 mm^2) of PET in air (1000 mbar) and in vacuum ($5 \times 10^{-2} \text{ mbar}$).

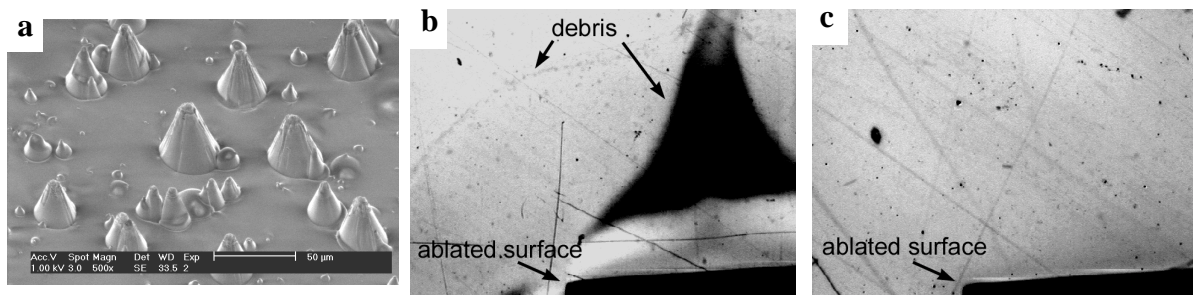


Figure V.4-2: (a) SEM micrograph of cones in amorphous PET (Static Ablation, $\Phi = 150 \text{ mJ/cm}^2$, $n = 1000$, 30° tilt angle in the SEM). (b), (c) Optical microscope images of debris near statically ablated surfaces (highly enhanced contrast). (b) Ablation in air (1000 mbar), (c) Ablation under vacuum $5 \times 10^{-2} \text{ mbar}$.

V.4.2 Debris in Scanning Ablation

The debris contribution to the surface structure in Scanning Ablation can be very important due to the direct redeposition mechanism which has been explained in section IV.2. At high ramp angles, debris can completely cover the micrometric structure, presented in sections V.1-V.3. An example of this is shown in Figure V.3-2c ($\vartheta = 45^\circ$). This important debris contribution is well adherent to the substrate and can thus determine the surface properties in microfluidic experiments. No change in the debris contribution can be observed by SEM and optical microscopy after rinsing the laminated micro channels with an aqueous phosphate buffer solution (pH = 7), using pressure driven flow ($2 \times 20 \text{ s}$, $\Delta P \approx 850 \text{ mbar}$) and electroosmotic flow (11 min., $E_z = 20 \text{ kV/m}$). Figure V.4-3 shows SEM micrographs of channels, which were ablated in amorphous, unstretched PET with high ramp angles. In this material the micrometric structure is absent (section II.2.2 and Figure V.1-1a) and the only surface structure is due to debris. Prior to the SEM investigation, these channels were laminated, used for electroosmotic flow measurements, and finally delaminated directly before introduction in the SEM chamber. The images show that the debris is still present and that there is no significant difference between a part of the channel where the flow passes, and a dead end of the channel, which sees no flow (schematic of channel configuration see Figure III.4-2b).

Another consequence of the direct redeposition pathway is, that close to the irradiated end ramp very little debris is observed, due to the forward peaking of the ablation plume (section II.3.1 and Figure IV.2-2b). However, sites on the channel floor, which are further away from the end

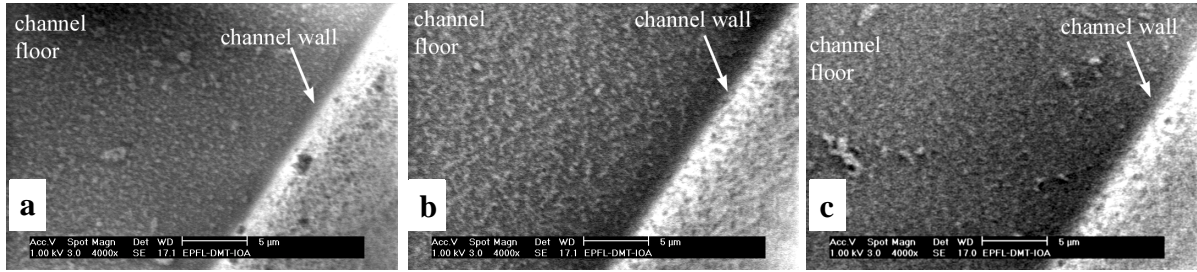


Figure V.4-3: (a) Debris in a dead end of the micro channel ($\vartheta = 22^\circ$). (b), (c) Debris at two different locations in the part of the micro channel that was rinsed during the electroosmosis experiments ($\vartheta = 40^\circ$). Small and big debris particles are still present.

ramp, correspond to direct redeposition along directions where more material is ejected (Figure IV.2-3). Moreover, the sites far away from the end ramp accumulated already the debris from the previous laser shots. Hence, a debris gradient is expected close to the irradiated ramp. The amount of debris saturates at a distance from the irradiated ramp, which can be called the “range of debris projection”. However, the analogy to a “projection range” is not really correct, because there is no ballistics, only gas dynamics. The debris gradient close to the end ramp was observed by SEM and Figure V.4-4b to h show the micrographs taken at the locations indicated in Figure V.4-4a. In order to enable a comparison of the images, special care was taken to adjust brightness and contrast to obtain approximately the same histogram of the zone, which is indicated in Figure V.4-4c. In order to distinguish debris from contrast enhanced noise in the images it is important to look at the evolution of the feature size.

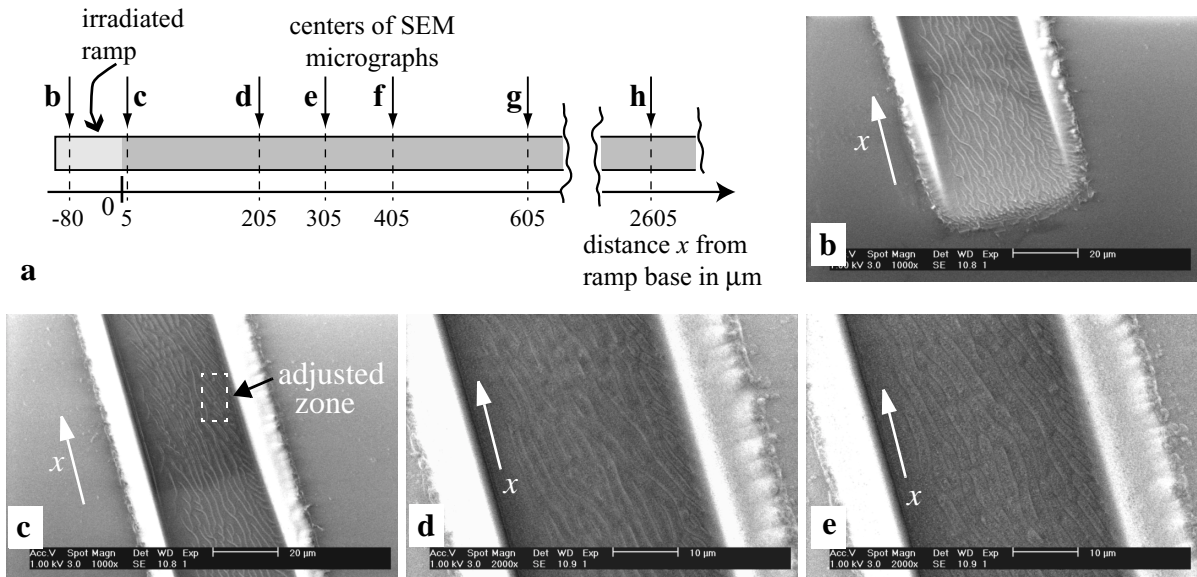


Figure V.4-4: The debris contribution in the channels as a function of the distance x from the base of the irradiated ramp ($\Phi = 600 \text{ mJ/cm}^2$, $a = 100 \mu\text{m}$).

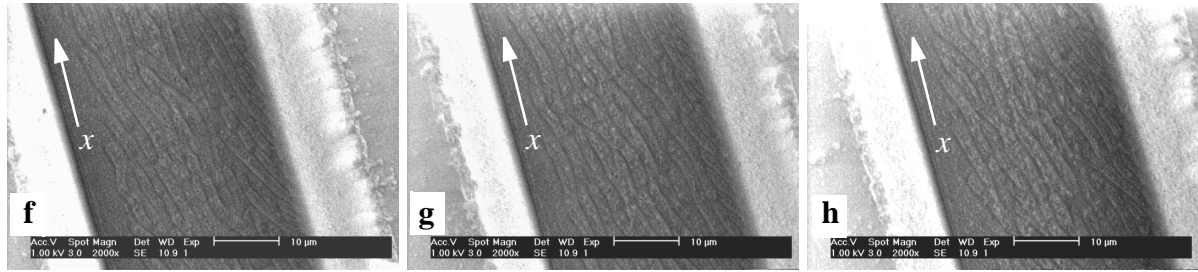


Figure V.4-4: The debris contribution in the channels as a function of the distance x from the base of the irradiated ramp ($\Phi = 600 \text{ mJ/cm}^2$, $a = 100 \text{ }\mu\text{m}$).

The evolution of the debris contribution to the surface structure can clearly be seen, and a range of debris projection of about $600 \text{ }\mu\text{m}$ can be estimated for the ramp angle of $\vartheta = 17^\circ$ and $\Phi = 600 \text{ mJ/cm}^2$. The same investigation was done for $\vartheta = 32^\circ$ and $\Phi = 600 \text{ mJ/cm}^2$ and the estimated range of debris projection is about $300 \text{ }\mu\text{m}$.

When considering direct debris redeposition according to Eq. 3 at a point in the channel floor having a fixed distance from the end ramp, it is visible from Figure IV.2-3 that, at a higher ramp angle more debris will be deposited at this point. This in turn means that the debris contribution on the channel floor saturates closer to the end ramp for higher ramp angles. The fact, that the angular density distribution is less forward peaked for shorter spot lengths a (corresponding to higher ramp angles) further enhances the outlined tendency [76].

V.5 Chapter summary

The surface structure of channels produced by Scanning Ablation was studied, in comparison with channels produced by Static Ablation. As in Scanning Ablation the channel floor structure is identical to the structure on the lower part of the irradiated ramp, the structure formation on ablated ramps was studied in detail.

Using differently stretched substrates, three different structure types were evidenced and shown to depend directly on the ramp angle. The different structures were interpreted as the result from a first partial, and then complete suppression of the Static Structure formation on the ramps. The reason for the suppression of the structure formation is the component of the frozen stresses in the material, which is perpendicular to the irradiated surface.

Additionally to this micrometric structure, the nanometric structure resulting from direct debris redeposition was investigated. In Scanning Ablation the amount of debris that can accumulate on the channel floor is important and depends on the ramp angle. As the debris was shown to be well adherent, it will play an important role in electroosmotic applications of the micro channels. The wetting properties of the micro channels will be determined by the chemical nature and the quantity of the debris. Further, it was shown that close to the end ramp, a gradient of the debris contribution to the surface structure exists in a limited region. The order of magnitude of the region, which is influenced by the debris gradient, was determined.

Hence, the surface structure of the micro channels is drastically changed by Scanning Ablation with respect to Static Ablation, especially at high ramp angles.

VI. Chemical surface composition and microfluidics

VI.1 Chemical composition of the ablated area

A good contrast in the O/C atomic ratio of surfaces after Scanning Ablation and Static Ablation was observed by X-ray photoelectron spectroscopy (XPS). Fresh samples show after Scanning Ablation an oxidized surface, which contains carbon atoms in many different chemical environments. After Scanning Ablation with a low ramp angle, nitrogen incorporation into the surface could be observed, originating most probably from indirect debris redeposition. Aging inverts the contrast in O/C ratio between static and Scanning Ablation. The presented data overestimates the debris contribution, due to the need of large channels. Transmission electron microscopy of prepared cuts of the surface confirmed the existence of an amorphous layer of approximately 80 nm thickness. Please note that A. Schwarz, from the Laboratory of Electrochemistry (EPFL), has investigated the chemical surface composition after Scanning Ablation with low ramp angles, in terms of functional groups, with selective binding methods [95, chapter 3].

VI.1.1 Transmission Electron Microscopy

Transmission Electron Microscopy (TEM) of channel cross-sections was carried out at the Polymer Laboratory (Materials Science and Engineering Department / EPFL). The sample preparation is described in section III.2.1. The initial aim of the investigation was to measure the thickness of the redeposited debris layer in 40 μm wide channels, produced by Scanning Ablation. Unfortunately, it revealed impossible. Nevertheless, the obtained results are interesting, because it was possible to give a direct measure of the laser modified layer thickness during ablation. The TEM measurements were performed with channels in the biaxially stretched PET standard substrate.

Substrate characterization Figure VI.1-1a shows the diffraction pattern of the bulk of the unirradiated substrate and a filtered dark field image of the same region. A dark field filtering method was applied in some of the following images, in order to obtain a contrast between oriented crystalline regions of the polymer and amorphous or unoriented crystalline regions. The diaphragm in the Fourier plane of the microscope, selecting the electrons used for the image reconstruction, was centered around one of the diffraction peaks as indicated in Figure VI.1-1a. The two main diffraction peaks originate from the oriented crystallites in the PET. Thus, selecting this light for the reconstruction of the image, causes the searched contrast, where oriented crystalline parts of the sample appear bright and amorphous or unoriented parts appear dark (Figure VI.1-1b). When considering that we used a biaxially stretched substrate, it is somewhat surprising to see that nearly all crystallites in our biaxially stretched substrates are oriented in one direction. The slightly visible rings indicate only a small percentage of unoriented crystallites. In the upper right corner of the image (grey ellipse), a second order diffraction of crystal-

lites oriented in the perpendicular stretching direction can hardly be distinguished. The size of the crystallites of about 5-10 nm in Figure VI.1-1b shows, as well as references [56] and [65], that the early proposition explaining the Static Structure ($\Lambda > 1 \mu\text{m}$) by selective etching of crystalline and amorphous domains in the polymer is wrong [36,62-64] (section II.2.2). However, this size comparison does not exclude the selective etching of spherulites as proposed by Andrew *et al.* [46] and observed after plasma etching [120] (structure size $0.1 \mu\text{m} - 1 \mu\text{m}$).

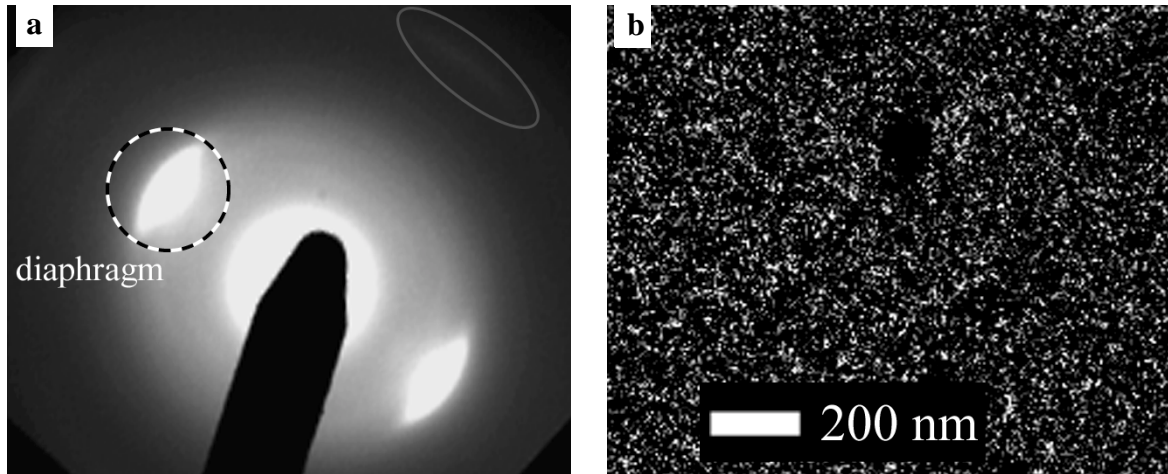


Figure VI.1-1: (a) Electron diffraction image of the biaxially stretched PET sample (bulk) showing the selected diffraction peak for image reconstruction in the following dark field TEM images. (b) Dark field TEM image of the bulk showing the size of the crystallites.

The ablated surface The TEM images in Figure VI.1-2a and b show filtered dark field images of irradiated samples. One observes a dark layer at the surface of both samples. ATR-IR spectroscopy measurements showed this layer to be amorphous and not only unoriented [26,27]. The thickness of the observed layer corresponds approximately to the melted layer during the ablation process. In several high magnification images (Figure VI.1-2c) the thickness of this layer was measured to be $80(\pm 20)$ nm, depending on the place on the structure where it was measured. Lazare *et al.* measured 85 nm by an ellipsometric method and subsequent conversion of the ellipsometer data using a single layer model [25].

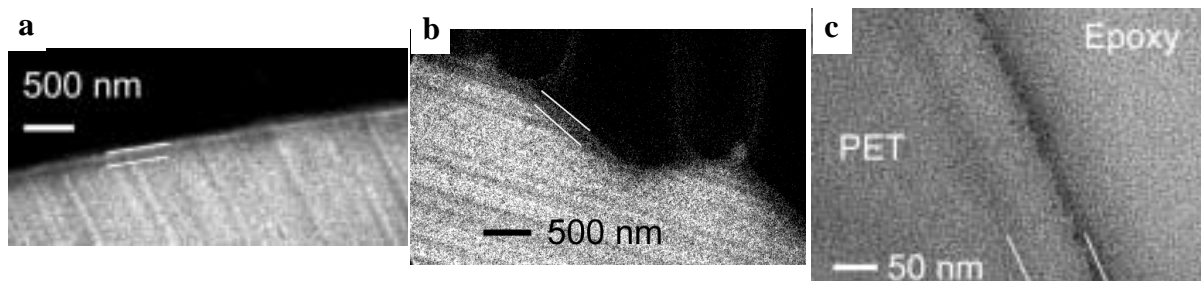


Figure VI.1-2: (a), (b) Filtered dark field TEM images of cross sections of the irradiated surfaces. (Scanning Ablation, $\vartheta = 1.8^\circ$, $n = 200$ shots per site, $\Phi = 600 \text{ mJ/cm}^2$.) (c) High magnification bright field image of the amorphous layer. (Scanning Ablation, $\vartheta = 2.3^\circ$, $n = 200$ shots per site, $\Phi = 1100 \text{ mJ/cm}^2$.)

By TEM analysis no difference could be found between Static Ablation and Scanning Ablation. The amorphous layer has in both cases the same thickness. Thus, wettability differences between Static Ablation and Scanning Ablation cannot be attributed to a change in crystallinity, as it was discussed by Lippert *et al.* for the observed difference in wettability between laser treated and untreated PET [33]. As already mentioned, it was impossible to measure the thickness of the debris layer on the surface, at the investigated ramp angle of approximately 2° .

VI.1.2 X-ray Photoelectron Spectroscopy

X-ray Photo-electron Spectroscopy (XPS), also called *Electron Spectroscopy for Chemical Analysis* (ESCA), was carried out at the Laboratory of Metallurgical Chemistry (Materials Science and Engineering Department / EPFL). Two series of measurements were performed. Once the samples were analyzed only some hours after production, and in the second experiment four month old samples were used. We investigated surfaces on the channel floor of 1 mm wide channels and statically ablated surfaces of 1 mm^2 in the biaxially stretched PET substrate. Wide channels were required, because of the limited spatial resolution of the used XPS-system (section III.2.2). Compared to the usually used $40 \mu\text{m}$ channels, the measured debris influence is overestimated, because the pattern for indirect debris redeposition changes in a way that more indirect debris is deposited onto the channel floor (section VI.3.2). The optical appearance of the four month old samples is shown in Figure VI.1-3. The fresh samples looked identically: (i) White and mat for the statically ablated surfaces, because of the Static Structure, which diffuses the light (Figure VI.1-3a). (ii) Slightly darkened and mat for the samples scanned with $\vartheta = 2.3^\circ$. Here a already visible debris layer was present (Figure VI.1-3b). (iii) Black and mat for the samples scanned with $\vartheta = 45^\circ$. A strong debris contribution due to enhanced indirect and important direct redeposition was visible (Figure VI.1-3c).

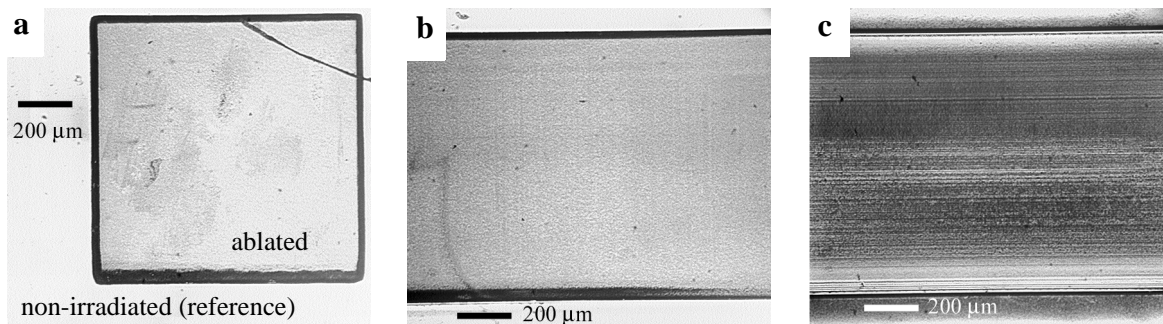


Figure VI.1-3: Optical transmission microscope images, at constant illumination intensity, of samples used for XPS four months after production. (Identical ablated depth $d_{\text{tot}} \cong 40 \mu\text{m}$.) (a) Statically ablated surface and reference. (b) Scanning Ablation ($\Phi = 1250 \text{ mJ/cm}^2$, $a = 1000 \mu\text{m}$, $\vartheta = 2.3^\circ$). (c) Scanning Ablation ($\Phi = 1250 \text{ mJ/cm}^2$, $a = 40 \mu\text{m}$, $\vartheta = 45^\circ$).

Fresh samples These samples were analyzed on the same day as they were produced, and they were kept in dry air in between. Prior to ablation, the substrate was washed with isopropanol and distilled water, and finally dried in air. Four types of irradiations were performed, each several times. Four spectra were acquired from different reference samples, i.e. non-irradiated sur-

faces that were far from the ablation sites. Two spectra were taken from different statically ablated samples, two from different scanned samples with $\vartheta = 2.3^\circ$, four from different scanned samples with $\vartheta = 22^\circ$, and four from different scanned samples with $\vartheta = 38^\circ$. Each spectrum consists of a survey run and the multiplex runs for the O1s-region, the C1s-region and also the N1s-region. As the samples charged, the acquisition time for each spectrum was kept low, resulting in noisy spectra with minimized peak broadening during acquisition. For comparison of the spectra, the aromatic C1s peak was fixed at 284.70 eV [93]. The same shift, as it was applied for the C1s core spectra, was applied to the other elements of the same sample. However there are two exceptions: first, the O1s spectra of the reference samples were not superposed after applying the C1s shift to them, indicating charging (or charge compensation adjustment) during acquisition. The superposition of the spectra was obtained by fixing the peak of the doubly bonded oxygen atoms to 531.26 eV [93]. Second, the same problem occurred (not so strong) with the O1s spectra of the scanned samples with $\vartheta = 38^\circ$. The reason is probably that two of the four spectra were acquired after lunch and the other two were added in the evening. Here, the four spectra were superposed by fixing the centers at the same position as the centers of the spectra of the samples scanned with $\vartheta = 22^\circ$, i.e. 532.78 eV.

Figure VI.1-4 presents the total O/C ratio and the relative atomic concentrations of oxygen, carbon and nitrogen in all samples. The theoretical values for the reference are marked by grey circles.

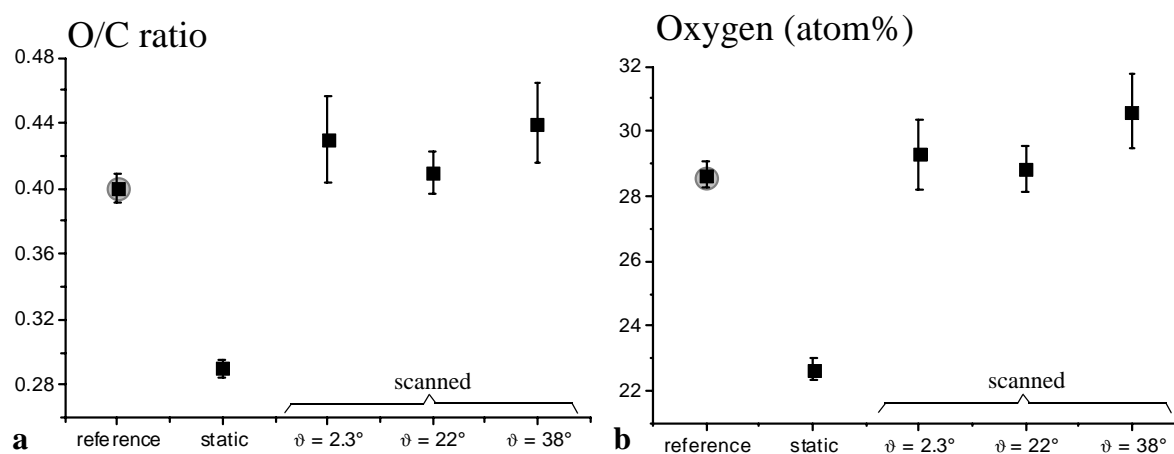


Figure VI.1-4: XPS data of freshly prepared samples. (a) The O/C ratio and the relative contributions of (b) oxygen, (c) carbon and (d) nitrogen. The theoretical values for the reference are marked by the grey circles.

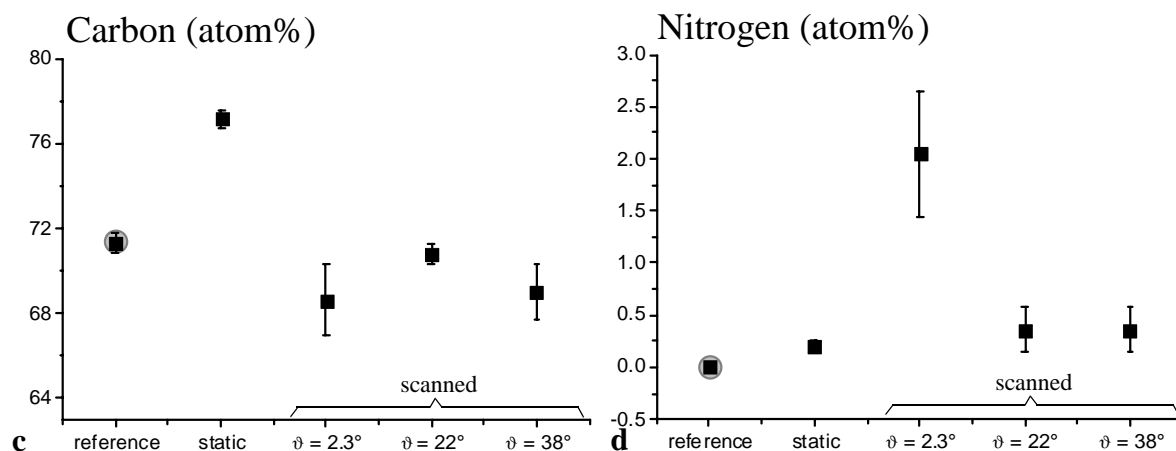


Figure VI.1-4: XPS data of freshly prepared samples. (a) The O/C ratio and the relative contributions of (b) oxygen, (c) carbon and (d) nitrogen. The theoretical values for the reference are marked by the grey circles.

First, concentrating on the O/C ratio graph (Figure VI.1-4a), the first two points confirm several literature reports speaking about a decrease of the O/C ratio of a PET surface upon excimer laser irradiation [26,28-33] (section II.2.1). However, after Scanning Ablation, the O/C ratio is found to be much higher compared to Static Ablation, and even slightly higher compared to the reference. An increase in the O/C ratio after laser irradiation was also reported in two (dependent) publications [19,27]. Bahners *et al.* also scanned their samples under the beam [27].

In fact, the XPS signal after Scanning Ablation is given by the debris, as explained in section IV.2.2. and visible in Figure VI.1-3. From the descriptions in references [19] and [27] it is not clear, whether their XPS spectra were acquired from an impregnated scanned sample, from a sample without impregnation, or from a statically ablated sample. Most probably they measured, as we did, a surface whose chemical properties are determined by the redeposited debris layer.

The XPS measurements of the debris determined surfaces confirm that the particulate ablation products react with the ambient air [71,72,90] (section II.3.3): The debris signal shows a slightly higher oxygen contribution (Figure VI.1-4b) and a slightly lower carbon contribution (Figure VI.1-4c) than the original PET, thus suggesting that the debris is oxidized. Further, a measurable amount of nitrogen is incorporated in the debris determined surfaces (Figure VI.1-4d, Figure VI.1-5 right side)

The nitrogen signal is very interesting, because it is the only one, showing a contrast between Scanning Ablation with different ramp angles ϑ (and/or spot lengths a). According to the reflections in section IV.2.2 and the SEM images in Figure V.3-2, channels with high ramp angles show a much higher quantity of direct debris, compared to the ones with low ramp angles. Figure VI.1-4d thus indicates, that the indirect debris reacts with the ambient nitrogen, whereas the direct debris does not. However, this contrast between $\vartheta = 2.3^\circ$ and $\vartheta = 22^\circ, 38^\circ$ is not visible in the oxygen and the carbon signal, reflecting the relative reactivity of N_2 and O_2 . Niino *et al.* already mentioned the presence of nitrogen moieties in PET surfaces after Scanning Ablation [92], but gave no details and no information on the O/C ratio. The value of 2 atom% of

VI.1 CHEMICAL COMPOSITION OF THE ABLATED AREA

nitrogen has to be considered as quite high, because after Static Ablation of PET in 1000 mbar of NH_4OH , which is a much more reactive environment than 800 mbar of N_2 , Chtaib *et al.* detected only 4 atom% of nitrogen in form of C=N bonds on the surface [29] (peak position not mentioned).

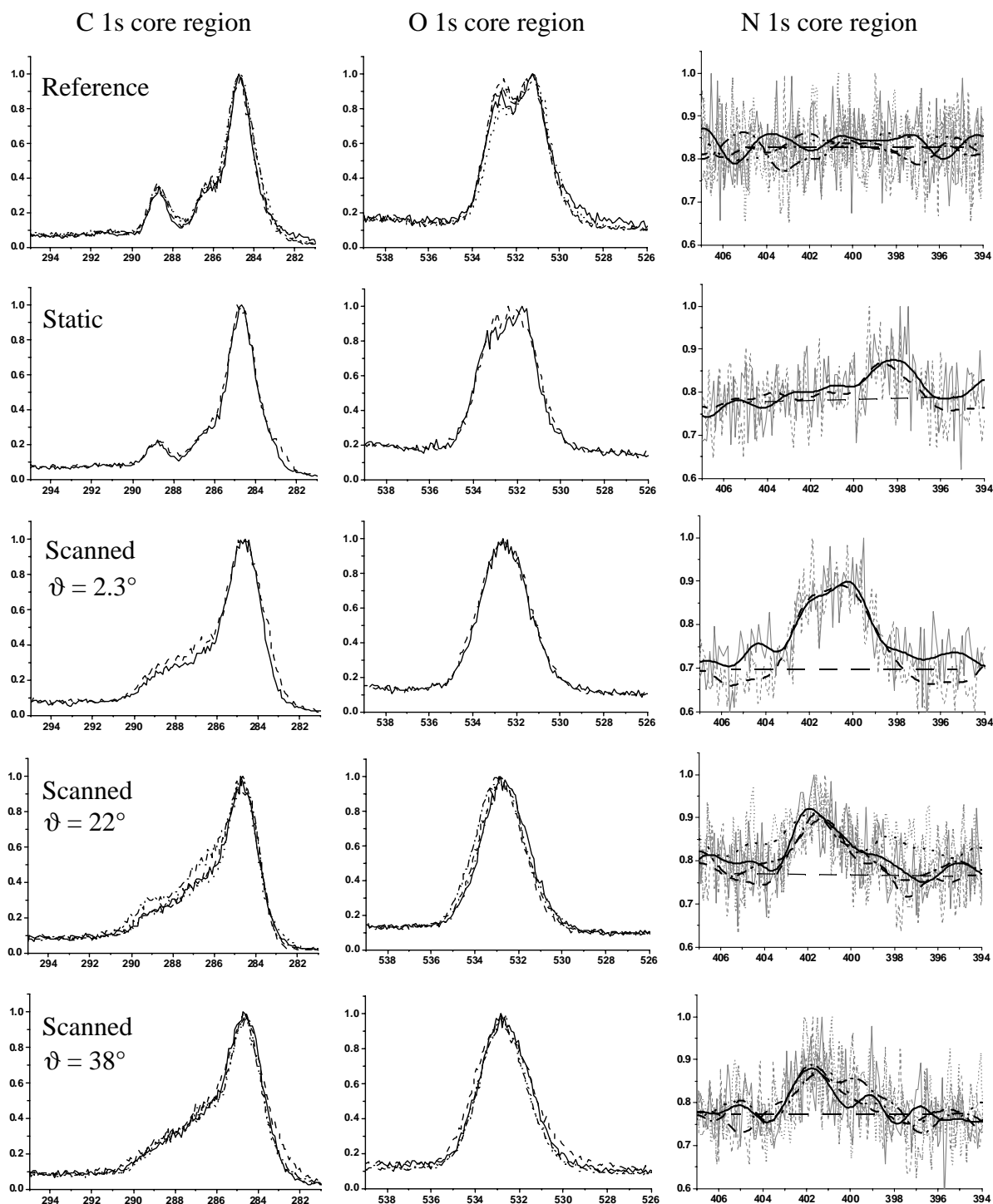


Figure VI.1-5: XPS multiplex data of freshly prepared samples. All spectra are normalized and show the *photoelectron intensity* as a function of the *binding energy in eV*. The C1s and O1s graphs show the shifted raw data. In the N1s graphs the shifted raw data is shown in grey, and the smoothed data (FFT filter, 9 points) together with a baseline in black. (All samples were ablated with $n = 200$ pulses of $\Phi = 1200 \text{ mJ/cm}^2$.)

Concentrating now on the normalized multiplex spectra, which are shown in Figure VI.1-5, we see that the nitrogen signal changes not only quantitatively but also qualitatively, when comparing Scanning Ablation at low and high ramp angles (Figure VI.1-5 right side). The nitrogen atoms in the indirect debris ($\vartheta = 2.3^\circ$) are probably bound to two different chemical environments. The approximate binding energies of the two nitrogen peaks are 401.9 eV and 400.1 eV. In the direct debris however, the peak at lower binding energy has nearly disappeared, and the one at higher binding energy decreased significantly. (The spectra in Figure VI.1-5 are all normalized). The chemical environments of the nitrogen atoms should consist of mainly carbon [19], but, as the surface is charged [92], the XPS signal may also come from nitrogen atoms that are included in ions.

The multiplex spectra of carbon and oxygen after Static Ablation confirm once more literature reports, that the oxygen bound carbon peaks decrease with respect to the aromatic carbon signal [29]. The C1s spectra of the surfaces after Scanning Ablation show a broad shoulder at higher binding energy indicating the coexistence of many different chemical environments for the carbon atoms. This conclusion was also drawn from selective binding experiments of PET after Scanning Ablation [95, ch. 3]. The shoulder of the C1s spectra meets the aromatic carbon peak at a relative intensity of 0.4 for $\vartheta = 2.3^\circ$, and at a relative intensity of 0.55 for $\vartheta = 22^\circ$ and 38° . This tendency is most probably due to the increased debris quantity at higher ramp angles, leading to an increased number of non aromatic carbon atoms. The O1s spectra after Scanning Ablation all have a triangular shape, indicating the presence of at least 3 different chemical environments for the oxygen atoms. No differences can be observed for the spectra corresponding to different ramp angles.

Four months old samples The second series of XPS measurements was carried out on samples that were stored for four months in a simple sample box in the office. The sample box was not air tight and was made out of an unknown polymer. The comparison of this measurements with respect to the previously reported ones gives indications on the aging processes on the surfaces. In this case, only one measurement was performed per sample type, and the samples were: Reference sample, statically ablated sample, scanned sample with $\vartheta = 2.3^\circ$, and another scanned sample with $\vartheta = 45^\circ$. As before, the aromatic peak of the C1s spectra was fixed to the literature value, and the spectra of all other elements were shifted by the offset, which was necessary for the C1s peak. Due to the charging of the samples the spectra do not have the same good resolution as the spectra of the fresh samples. This is evident when comparing the O1s spectra of the reference samples (Figure VI.1-7 center top, and Figure VI.1-5 center top). Additionally the O1s spectrum shifted to lower binding energies between the acquisitions. In consequence, the peak positions cannot be interpreted, but the shape and symmetry of the peaks can.

Figure VI.1-6 shows the O/C ratio and the relative contributions of oxygen, carbon, fluorine and nitrogen of all samples. The origin of the unexpected fluorine signal is unknown, but the most probable explanation is a contamination from the sample box by adsorption to the PET and the nanoporous debris layer [121]. As the quantity of debris increases from the left to the right on the x -axes, the adsorbed fluorine quantity increases also.

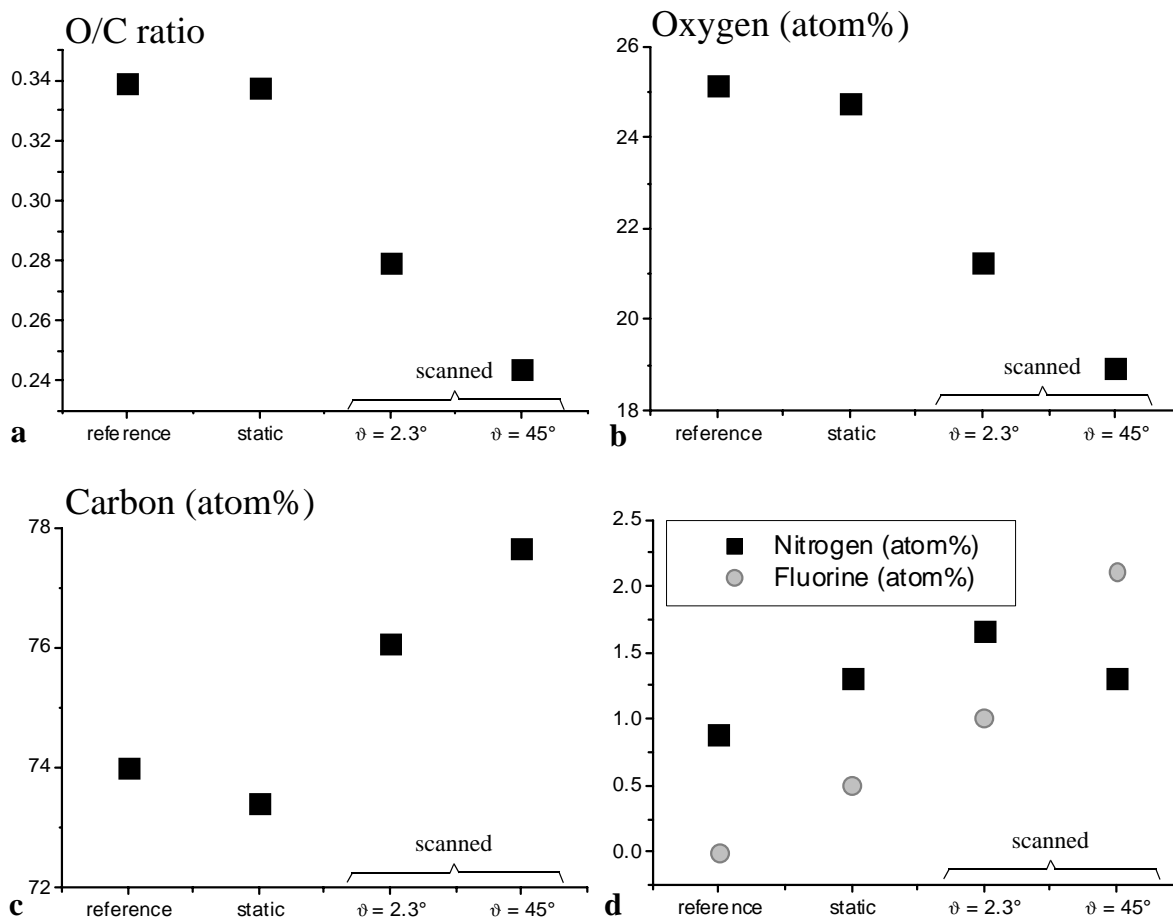


Figure VI.1-6: XPS data of four month old samples. (a) The O/C ratio and the relative contributions of (b) oxygen, (c) carbon and (d) fluorine together with nitrogen. Only one measurement per type was performed.

According to this measurement, the reported and reproduced decrease of the O/C ratio upon Static Excimer Laser Ablation of PET has disappeared four months after sample preparation. Assuming the statically ablated surface to be free of debris, our observation confirms the literature report on the aging of air-corona treated PET films [44]. Strobel *et al.* reported that functionalized PET surfaces, with polar groups at the surface, age much faster compared to PP, due to the ester functionalities in the PET bulk, which interact with the surface functional groups. This interaction enhances the diffusion of the surface polar groups into the bulk. A first increase in the water contact angle and decrease in XPS O/C ratio was already measured after 7 days of storage in air at room temperature. The aging could be slowed down by storing the sample in water.

Our measurements show still a contrast between the O/C ratio of the statically ablated sample and the scanned samples. The contrast is inverted with respect to the measurements of freshly prepared samples, indicating that the debris has become more graphitic. The measured nitrogen content is more or less constant at 1.2%. Nevertheless we measured once more the highest nitrogen content for the sample where the most important contribution of indirect debris is expected ($\vartheta = 2.3^\circ$). Moreover, the N1s core spectrum for the scanned sample with $\vartheta = 2.3^\circ$, conserved its double peak shape, already observed on the fresh samples (Figure VI.1-7 right side).

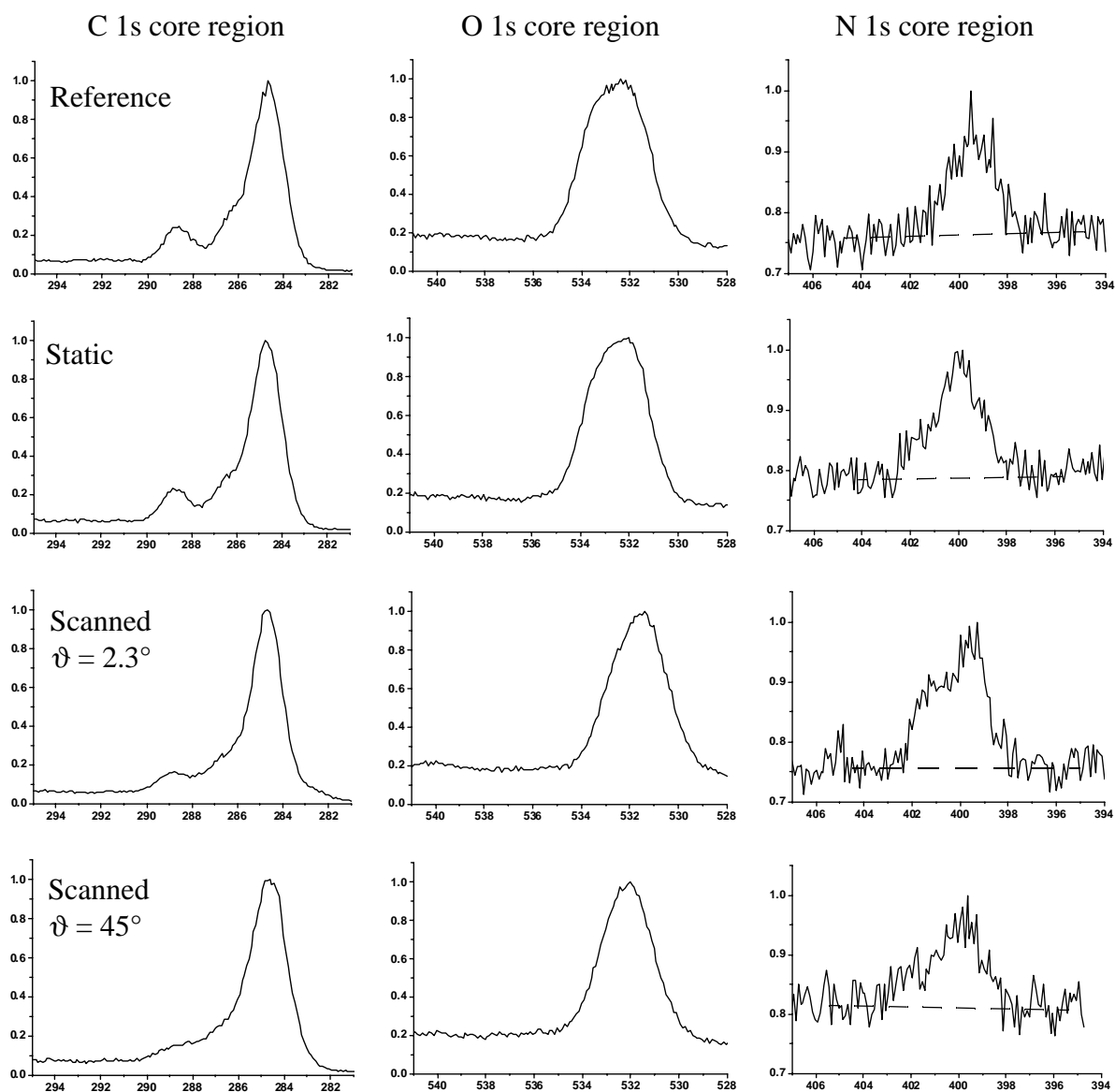


Figure VI.1-7: XPS multiplex data four months after sample production. All spectra are normalized and show the photoelectron intensity as a function of the binding energy in eV. (All samples were ablated with $n = 200$ pulses of $\Phi = 1200 \text{ mJ/cm}^2$.)

Comparing the N1s core spectra of the two scanned samples it seems that aging inverted the asymmetry of the nitrogen spectrum of the direct debris. For the fresh samples the contribution at higher binding energy was more important, and for the aged sample the lower binding energy peak is higher. The C1s spectrum after Static Ablation is nearly identical to the reference spectrum, in particular no decrease of the oxygen bound carbon peaks is visible. After Scanning Ablation with $\vartheta = 2.3^\circ$, the carboxylic carbon peak in the spectrum still shows up, or better shows up again, because for the fresh samples it was hidden in the shoulder at high binding energy. This shoulder is still present in the sample with $\vartheta = 45^\circ$, but meets the aromatic carbon peak at a relative intensity of 0.3 compared to 0.55 for the fresh samples.

XPS summary The measurements show a good contrast in the O/C ratio after Static Ablation and Scanning Ablation, proving that substrate scanning strongly influences the chemical surface

properties of the ablated surfaces. This is due to the redeposited material, as explained in section IV.2. The difference in surface properties after Scanning and Static Ablation possibly allows for understanding of the contradictory literature reports on the surface properties after Excimer Laser Ablation of PET. (Increasing O/C ratio [19,27], decreasing O/C ratio [26,28-33].)

In detail we observed that the surface after Scanning Ablation is of an oxidized nature, comprising many different chemical environments of carbon atoms. The XPS measurements also allow to distinguish indirectly redeposited debris from directly redeposited debris by using the nitrogen signal, which is higher and composed of two peaks in the case of indirect debris. The aging of the examined surfaces was shown to inverse the O/C contrast between Static Ablation and Scanning Ablation. After four months, the statically ablated surface is hardly distinguishable from the original PET surface and a carbonization of the debris took place. The relative importance of the aromatic carbon peak in the C1s spectrum of old debris is higher, compared to the one of fresh debris, indication that the debris becomes more graphitic.

VI.2 Interaction of debris and water

The hydrophilicity of indirect debris upon Static Laser Ablation in ambient air is demonstrated. The wettability of the debris affected surface is determined by the chemical nature of the debris, and the existing nano scale roughness has no measurable influence. An attempt to measure contact angles inside the 40 μm wide channels by means of an Environmental Scanning Electron Microscope (ESEM) is reported and propositions for improving the contact angle measurement are made.

VI.2.1 Contact angle measurement in a channel

In literature, XPS measurements are often paralleled by water contact angle measurements [28,44,122] in order to get an independent second information on the same surface properties. As described in section VI.1.2, the width of the channels influences the quantity of indirect debris on the channel floor. In order to avoid this overestimation of the indirect debris quantity in wide channels, we tried to measure the water contact angle in 40 μm wide channels.

The conditions for this measurement are extremely difficult. It might be even impossible to get *reproducible* contact angle values in stretched samples, because the channel floor usually has a width of 30 μm and the period and amplitude of the Static Structure is about 3 μm [33]. Nevertheless, an attempt for a direct contact angle measurement was done in an Environmental Scanning Electron Microscope (ESEM) at the Swiss Federal Laboratories for Materials (EMPA). The channels were prepared one day before the measurement in biaxially stretched PET, and crossed the border of the substrate. Thus, the observation of the channel floor was possible not only in top view but also in side view. Water was condensed in the ESEM chamber, during the observation by increasing the water vapor pressure from 3 mbar to 6 mbar at 3°C. Unfortunately, it was not possible to obtain drops in the channel, being stable for the acquisition time. First the water condensed only outside the channel (Figure VI.2-1a), and then rushed in (Figure VI.2-1b). Only on the side walls of the channel drops were more stable (Figure VI.2-1b).

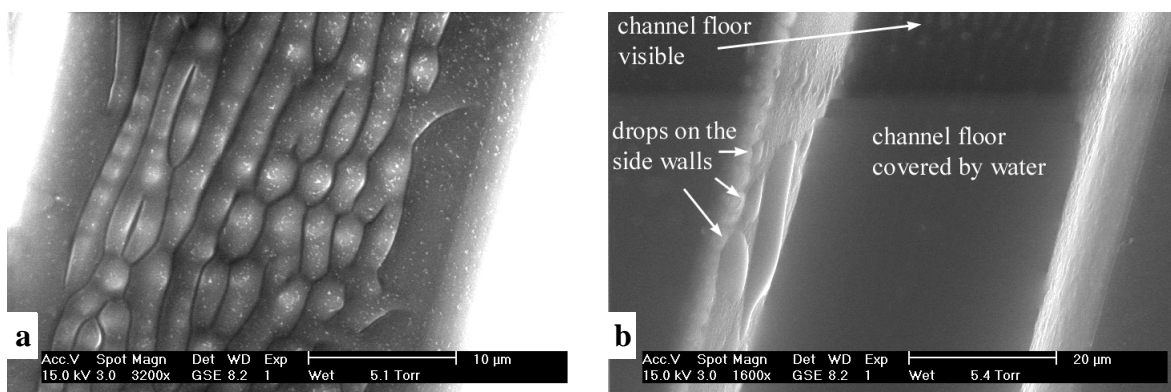


Figure VI.2-1: ESEM images of a 40 μm wide channel. (Scanning Ablation, $\vartheta = 11^\circ$, $\Phi = 1100 \text{ mJ/cm}^2$, $a = 200 \mu\text{m}$.) (a) Wet sample, but with water condensed only outside of the channel (Scanning Structure with little debris) (b) With water condensed in the channel. The water moved in the channel during the acquisition of the image.

A more serious investigation of contact angles in 40 μm wide channels, needs to take into account the following points:

1. Use unstretched substrates, for reduced roughness.
2. Take into account the gravity. (The channel floor needs to be horizontal.)
3. Produce small drops as seeds by spraying.
4. Work always close to thermodynamic equilibrium. (Measurement of advancing and receding contact angles.)

VI.2.2 Condensing experiment

A simple experiment was carried out, in order to show how the fresh debris changes the wetting properties of the biaxially stretched PET substrate. A statically ablated sample was placed under an optical microscope and water was condensed near the irradiated region by simply exhaling onto the substrate. The condensation and evaporation of the water was filmed with a color CCD camera. The experiment could be carried out with excellent reproducibility many times on the same irradiated area. The reproducibility for samples produced on different days was good, but the ease of condensation depended on the weather (temperature of the sample, and relative humidity).

Figure VI.2-2a left side, and Figure VI.2-2b show a wet sample at a moment where the contrast between the different zones A, B, C was optimal. An image of the dry sample after complete evaporation of the water is given at the right side of Figure VI.2-2a.

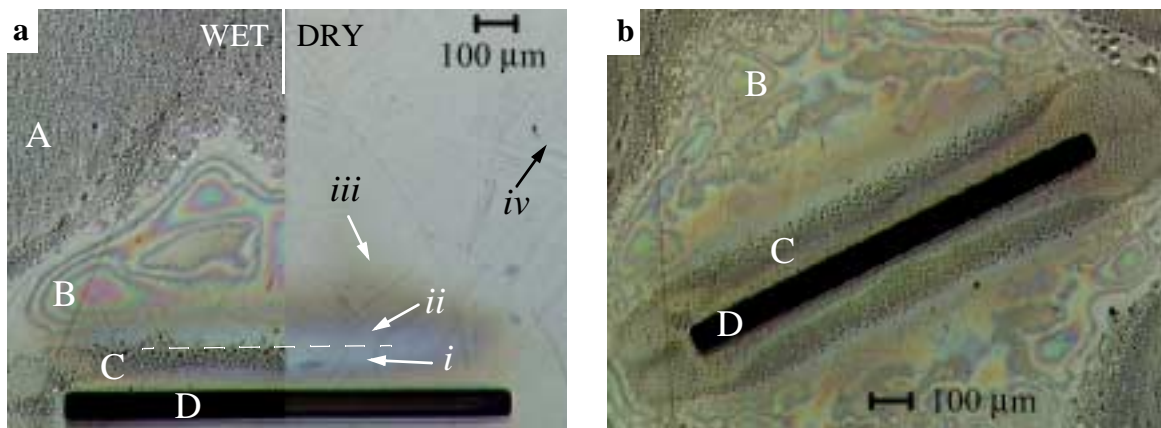


Figure VI.2-2: Optical microscope images of the region near a statically ablated surface D ($n = 200$, $\Phi = 1000 \text{ mJ/cm}^2$). (a) Direct comparison of the sample with water condensed on it (left side) and without (right side). The indicated sites i to iv show where the AFM pictures in Figure VI.2-3 were taken. The indicated zones A, B, C, D correspond to: D - irradiated area; A - unmodified PET; B,C - debris modified PET. (b) Wet sample giving a better view of zone C.

Different zones were evidenced in Figure VI.2-2: Zone A is the native PET substrate without debris. Small droplets (visible as dark dots in the microscope images) form, because PET is only partially wetted by water ($\gamma_a = 67(\pm 4)^\circ$, $\gamma_r = 56(\pm 4)^\circ$ [36]). Zone B and C are modified by the debris redeposition (compare to Figure V.4-1), but they do not show the same wetting behavior.

A thin film of water formed in zone B, whereas again small droplets are observed in zone C. Zone D is the irradiated area.

A first result of this experiment is that debris can be hydrophilic in spite of its carbonaceous nature, leading to spreading of the water, or complete wetting, in zone B. However, not the whole debris affected zone is wettable.

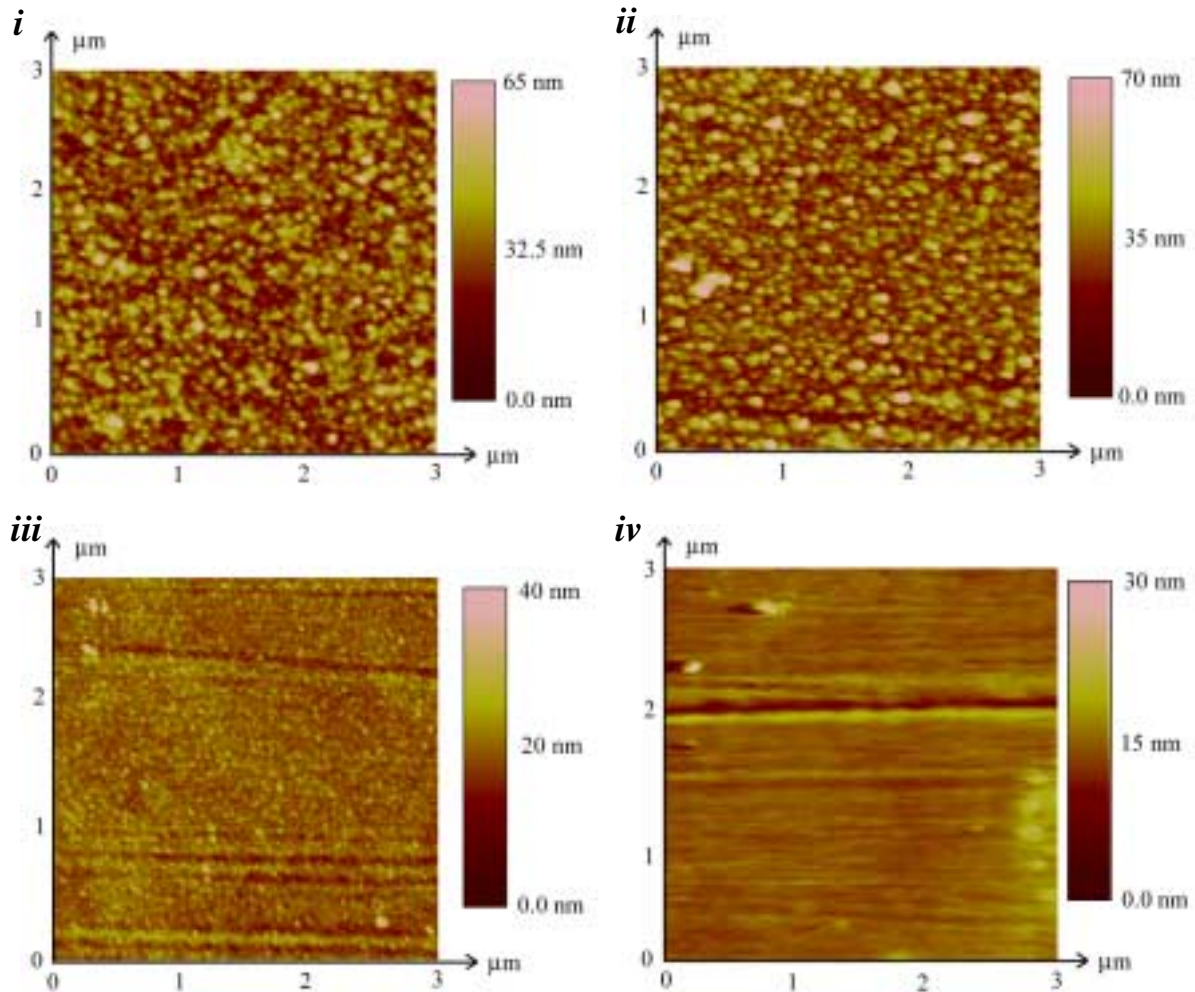


Figure VI.2-3: AFM images of the sites *i* to *iv* indicated in Figure VI.2-2a. (*i*) Zone C. (*ii*) Zone B, close to the border. (*iii*) Zone B, middle. (*iv*) Reference (zone A).

In general, the wettability depends on the chemical composition of the surface and its roughness (section II.4). Atomic Force Microscopy (AFM) images of the sites indicated in Figure VI.2-2a were taken at the Institute of Condensed Matter Physics (University of Lausanne), in order to investigate the roughness of zones B and C compared to the original PET. Figure VI.2-2a also shows that the limit between zone B and C, indicated by the dashed line, passes right on the middle of the main debris hump, which is visible in the dry image. In conclusion, a big roughness difference between site *i* and site *ii* would be astonishing. The AFM images presented in Figure VI.2-3 confirm this conclusion. Inspection of Figure VI.2-3*i* and *ii* confirms that there is no significant difference in roughness between zone B and C, close to their border line. However, comparison of Figure VI.2-3*iii* and *ii* shows that a much more remarkable difference in

roughness is present inside zone B, but no difference in wetting behavior of the sites *ii* and *iii* was observed.

In conclusion, the wetting contrast between zone B and C is not caused by a roughness variation, and is hence due to a difference in surface chemistry (section II.4).

When comparing the experimental picture and the calculation from Miotello *et al.* (Figure II.3-1) [85], one can see that there are differences in a region very close to the ablated surface, approximately corresponding to zone C. The trajectory of the debris in this zone is most probably very short, because the expanding plume (high pressure) presses the debris rapidly down to the surface. Thus the debris in this zone is comparable to the *direct* debris introduced in section IV.2.2.

By XPS, the only difference between indirect and direct debris, zone B and C respectively, was a difference in the nitrogen content, which was higher in indirect debris. The condensing experiment thus gives the additional information that this difference in the chemical composition corresponds to a higher hydrophilicity of the indirect debris.

The influence of the ambient atmosphere on the chemical composition, and thus the wetting properties, of the *indirect* debris is demonstrated by the condensing experiment on samples ablated in air, in argon, and in nitrogen (Figure VI.2-4).

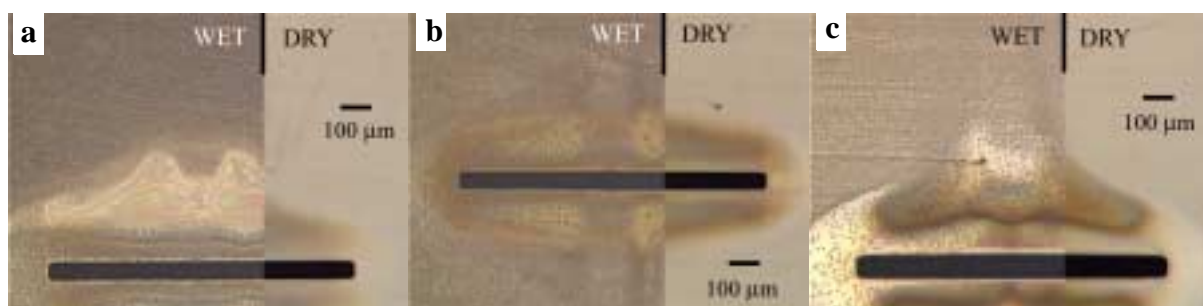


Figure VI.2-4: Condensing experiment after Static Ablation in different ambient atmospheres ($\Phi = 670 \text{ mJ/cm}^2$, $n = 200$, 1000 mbar). (a) Air. (b) Argon. (c) Nitrogen. The amount of condensed water was approximately equal in (a) and (b), and slightly lower in (c) as reflected by the luminosity of the pictures.

It is clearly visible that only after irradiation in air a wettable zone appears. Neither Figure VI.2-4b nor Figure VI.2-4c show the thin film of water visible in Figure VI.2-4a. This is in agreement with the observation of Rossier *et al.* who stated a high capacitive current of indirect debris electrodes from 193 nm ablation of PS only after ablation in air [90]. At approximately constant nanometric porosity a higher wettability of the electrodes results in a higher electrolyte surface in contact with the electrodes [102], and, in consequence, higher capacitive currents.

Comparing the exhibited hydrophobicity in Figure VI.2-4c to the results of the XPS measurement of fresh debris, indicates that in the case of the ablation in air the nitrogen in the surface is bonded to oxygen containing functional groups. This accounts for the double peak shape of the XPS nitrogen signal, and explains also that in absence of oxygen the nitrogen (supposed that there is some in Figure VI.2-4c) does not cause hydrophilicity. In fact the surface seems to be more hydrophobic after ablation in nitrogen than after ablation in argon. This is probably,

caused by insufficient purging of the reaction chamber (ca. 25 liters) before performing the argon experiment. The nitrogen experiment was carried out after the argon experiment. Comparing the size of the wettable zone in Figure VI.2-4a to the one in Figure VI.2-2, it is visible that the wettable zone is smaller after ablation with lower fluence. The fact that the samples shown in Figure VI.2-4 were produced and analyzed on a hot and humid summer day, may also be responsible for this difference.

VI.3 Electroosmotic flow control

Electroosmotic flow control by variation of the Scanning Ablation parameters is demonstrated. For this purpose, electroosmotic flow velocity measurements in micro channels with identical cross sections were carried out. The channels were produced using different spot lengths, leading to different ramp angles during the fabrication. The electroosmotic flow velocity in the channels varied by approximately 25% of the maximum value, and showed its maximum value at a ramp angle of 4.3°. The existence of the maximum can be explained qualitatively by the competition of indirect and direct debris redeposition in the already ablated channel. Indirect redeposition in the channel is enhanced when going to shorter spot lengths. Direct redeposition becomes most important at high ramp angles. The presence or orientation of the micrometric structure on the channel floor showed only slight or negligible influence on the electroosmotic flow.

“For many applications it is desirable to be able to manipulate the magnitude of the electroosmotic flow in order to optimize separation performance” (P. D. Grossman [6]).

Electroosmotic flow experiments were performed with laminated channels, described in section III.4. The channels were produced by Scanning Ablation with different ramp angles and showed approximately the same cross section. Three types of samples series were produced, differing in the micrometric structure, if $\vartheta < 22^\circ$ (section V.2):

1. The biaxially stretched substrate was used, and the main stretching direction was aligned perpendicularly to the scanning direction. Thus, the mountain-chain like, Static Structure was aligned with the channel direction (section V.1.3) and the series is named *longitudinal series*.
2. Once more the biaxially stretched substrate was used, but this time the main stretching direction was aligned with the scanning direction. Hence, the Static Structure was oriented perpendicularly to the channel direction and the series is named *transversal series*.
3. In this case an amorphous, unstretched substrate was used, and hence no Static Structure formed. The only change in structure within this series is due to the debris contribution to the surface roughness (section V.4.2). The channels of this *amorphous series* had a slightly different production procedure, because the substrate was too thick to use through drilled reservoirs (section III.4.3).

The average electroosmotic flow velocity of the buffer solution in the ablated and laminated channels was measured by the current monitoring technique, as described in sections III.5.1 and III.5.2.

VI.3.1 Experimental results

The measured electroosmotic flow velocity v_{eo} is reported as a function of the ramp angle ϑ in Figure VI.3-1. All measurements were performed with the same phosphate buffer solution at pH = 7.2, using the same salt concentrations of the buffer (8 and 10 mMol/l). The driving field $E_z = 20$ kV/m was also kept constant in all measurements. In the graphs of Figure VI.3-1 the

different curves refer to samples, which were produced and/or analyzed on different days, and the error bars indicate the standard error of the electroosmotic flow velocity measurement. Figure VI.3-1a, b and c show each measurements of one series and Figure VI.3-1d shows all measurements superposed.

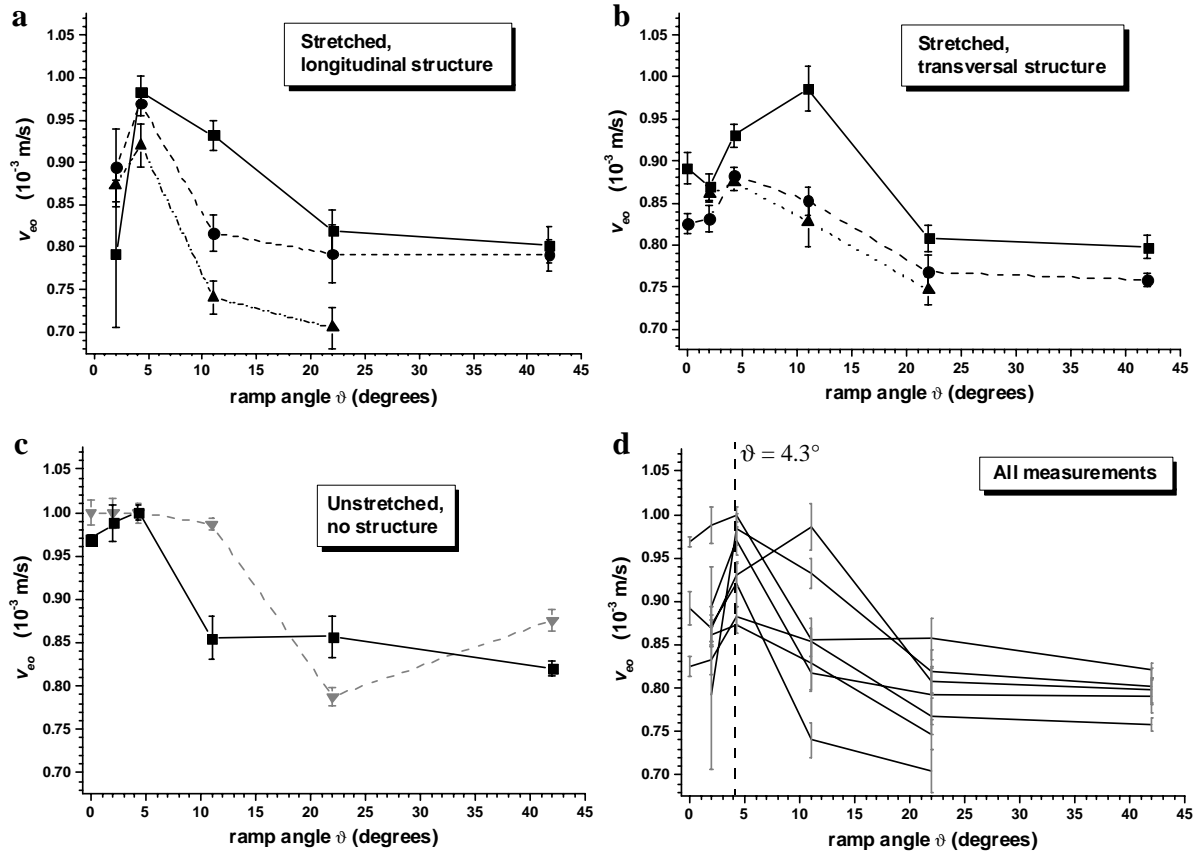


Figure VI.3-1: Electroosmotic flow velocity v_{eo} as a function of the ramp angle ϑ . **(a)** Longitudinal series. **(b)** Transversal series. **(c)** Amorphous series. **(d)** Superposition of (a), (b) and (c). (The measurement in (c), indicated in grey is not reliable, because the channel length was not sufficiently controlled.) $\vartheta = 0^\circ$ are cleaned scanned channels (details see below).

Figure VI.3-1 illustrates the possibility to control the electroosmotic flow in our channels by varying the Scanning Ablation parameters. The flow velocity varies in a range of approximately 25% of the maximum value by varying the ramp angle ϑ from 2° to 42° . For nearly all measurements and substrates, the maximum flow velocity is observed at a ramp angle of 4.3° (Figure VI.3-1d). The flow velocities can reach 2/3 of the electroosmotic flow in fused silica capillaries, which generate under the same conditions a flow of $v_{eo} = 1.4 \times 10^{-3}$ m/s. (Value converted from reference [118] using Eq. 5, Eq. 6 and Eq. 8.

All data presented in Figure VI.3-1 were obtained for laminated channels. The polyethylene lamination is the same for all channels and thus smooths the flow velocity data. This means that the observed variations are lower than the variations that would be observed if all four walls of the channels were ablated surfaces. After the determination of the ζ -potential for the lamination

(section VI.4.5), it is possible to compensate by calculations for this smoothing effect. We can thus obtain information on the ζ -potential of the ablated surfaces (Figure VI.4-7).

The presented data also show that the variations between channels produced and/or analyzed on different days are higher than the error of the measurement method (given by the error bars). The main parameters, which were not well controlled during the production of the micro devices are: (i) Different times between channel production and electroosmotic measurements. (ii) The homogeneity of the lamination. (iii) The atmosphere in which the ablation was carried out, i.e. the composition and the flow of the clean room air. As functionalized PET surfaces are subject to rapid aging, point (i) seems the most probable explanation [44]. The exact dynamics for the aging of the debris are unknown, but it is clear from the XPS measurements in section VI.1.2, that the surface properties of debris changed after four months, but not after six hours.

In spite of the rather fair reproducibility of the numerical values in Figure VI.3-1, a comparison with the flow velocity values published by Roberts *et al.*, who worked with very similar channels [3], yields good results. Roberts and co-workers produced their devices by Scanning Ablation with $\vartheta = 2^\circ$ and reported a value of $v_{eo} = 12.6 \times 10^{-4}$ m/s at $E_z = 30$ kV/m, corresponding to $v_{eo} = 8.4 \times 10^{-4}$ m/s at $E_z = 20$ kV/m. They used the same biaxially stretched substrate and the Static Structure was oriented at 45° with respect to the channel direction. Comparing this with the average of the values in Figure VI.3-1 we find an excellent agreement for the longitudinal series ($v_{eo} = 8.3 \times 10^{-4}$ m/s) and the transversal series ($v_{eo} = 8.5 \times 10^{-4}$ m/s). However, the reliable value of the amorphous series is 18% higher ($v_{eo} = 9.9 \times 10^{-4}$ m/s). This may indicate that the *presence* of the Static Structure slows down a little bit the electroosmotic flow. However, to confirm this observation, further investigations are necessary. According to the presented data, the *orientation* of the Static Structure has no influence on the electroosmotic flow.

The data presented in Figure VI.3-1 were all acquired at a driving field of $E_z = 20$ kV/m. Because the dependency of the electroosmotic flow velocity v_{eo} on the driving field E_z in a given channel is a complementary method to characterize the quality of the electroosmotic measurements (Eq. 8), two typical examples for this relation are given in Figure VI.3-2.

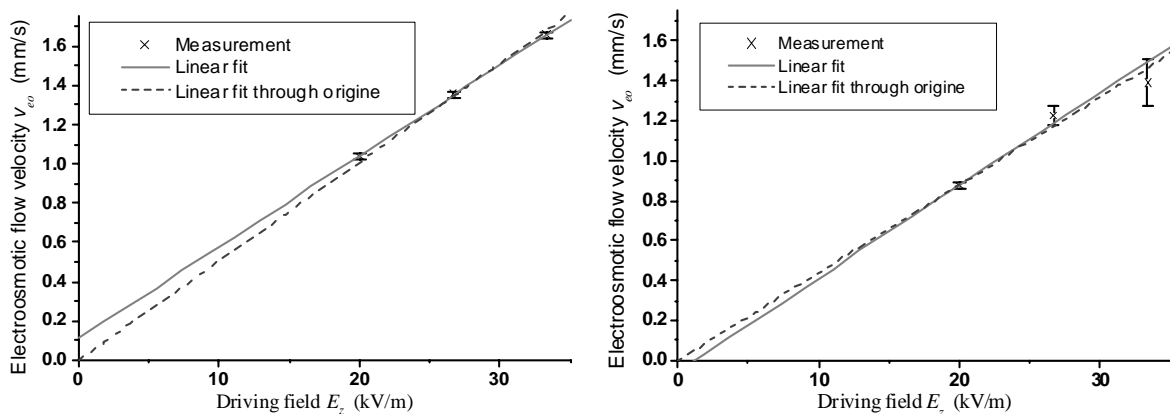


Figure VI.3-2: Electroosmotic flow velocity v_{eo} as a function of the applied driving field E_z .

Astonishingly, compared to the report of Niino *et al.* [91], we observed a negative ζ -potential of the channels, i.e. the electroosmotic flow was always in the direction of the negatively charged electrode.

In an attempt to produce channels with good geometrical quality over the whole channel length, exhibiting nevertheless the properties of statically ablated channels, we tried to clean scanned channels from debris by a second scan. This means that first a *digging scan* was done with $n = 199$ or $n = 198$ pulses per site ($\vartheta = 2^\circ$) and then a *cleaning scan* with $n = 1$ or $n = 2$ pulses per site ($\vartheta = 0.02^\circ$) followed. In nearly all cases these channels showed the same electroosmotic flow velocity as the channels which had simply been scanned with $n = 200$ and $\vartheta = 2^\circ$ (Figure VI.3-1, values at $\vartheta = 0^\circ$). A possible explanation of this result, with the assumption that the cleaning scan really did clean the channel floor and the walls from accumulated debris, might be:

The amount of indirect debris redeposited after one pulse may be sufficient to explain the limited hydrophilicity of the ablated surface. The following estimation supports this thesis.

Up to 43% of the material, ablated by one shot, are redeposited on the substrate [84]. As for PET the sideways expansion of the debris is not especially high, most of this debris will redeposit onto the ablated surface. According to Kelly *et al.* [82] only particulate ablation products will eventually form debris. As no literature value for the yield of particulate ablation products from PET is available, we use the value of PI as a lower estimation. Working at rather high fluences, where disintegration of the particles in the plume by the laser light seems probable, we use the lower of the two literature values, i.e. 4% [82]. Assuming the redeposition of 30% instead of 43%, of the particulate debris, because of sideways expansion, we end up with 1.2% of the ablated material that is redeposited onto the ablated surface. Now, knowing the ablation rate of 200 nm, thus, say 1000 layers of atoms (polymer), we end up with a redeposited layer of 13 atoms thickness. This layer may in fact contain a sufficient number of polar groups for causing the observed limited degree of hydrophilicity, but not enough to change the XPS signal, to an increasing O/C ratio, with respect to unirradiated PET. This is supported by the observation of Chtaib *et al.* who performed XPS measurements of PET after static irradiation of PET at 193 nm with various fluences [29]. They observed an increase in the O/C ratio at fluences higher than the ablation threshold, compared to the O/C ratio at fluences just below the threshold. This can most probably be attributed to debris redeposition. Also, Lazare *et al.* measured an increasing water contact angle hysteresis and decreasing receding contact angles on amorphous PET samples without micrometric roughness, after Static Ablation at 193 nm [36]. The same tendencies were observed more pronounced after ablation of poly(phenylquinoxaline) (PPQ) films, and particularly the decreasing receding contact angle was interpreted as an increase in hydrophilicity [87]. Because of the higher sampling depth of XPS with respect to contact angle measurements, these findings do not contradict the many reports of decreasing O/C ratio after ablation. In the report of Chtaib *et al.*, the O/C ratio also stayed below the level of the reference sample, even at 200 mJ/cm².

VI.3.2 Explanation of the optimum

The main feature of all electroosmotic measurements shown in Figure VI.3-1 is the existence of an optimum ramp angle for fastest electroosmotic flow. This can be understood when one considers the changing relative contributions of indirect and direct debris to the total debris on the channel floor and the channel walls.

In cases where *indirect debris* is predominant, i.e. at low ramp angles, the channel surface is hydrophilic. This was shown directly by the results of the condensing experiment in section VI.2.2. Further the surface contains not only polar oxygen-functional groups, but also nitrogen-functional groups as shown by the results of the XPS measurements.

On the contrary, when *direct debris* is most important, i.e. at high ramp angles, the channel surface is relatively hydrophobic, which is also a conclusion of the condensing experiment. The XPS measurements in section VI.1.2 showed, that direct debris also contains polar oxygen-functional groups. This is the reason for the relatively high level of electroosmotic flow at very high ramp angles, being comparable to the electroosmotic flow at very low ramp angles where only little indirect debris and no direct debris is present Figure VI.3-1d.

It was shown in section IV.2.2, the contribution of direct debris is expected to be negligible at low ramp angles, but that it becomes dominant in the case of high ramp angles (Figure V.3-2). The change between “low” and “high” ramp angles in this sense depends on the shape of the density distribution $\rho(\varphi)$, at the given parameters. Especially, the extent of forward peaking of the plume is important for the absolute value of the transition regime between “low” and “high” ramp angles.

Concerning the contribution of indirect debris, it is known that the shape of the indirect debris pattern upon Static Ablation depends on the shape of the irradiated surface (section II.3.2). For the channel production, rectangular masks with the same width and different lengths were used. The relative contribution of the indirect debris in the channel upon *Scanning Ablation* is closely correlated to the quantity of indirect debris upon *Static Ablation*, which is redeposited in the 40 micrometer wide band, covered by the channel (Figure VI.3-3).

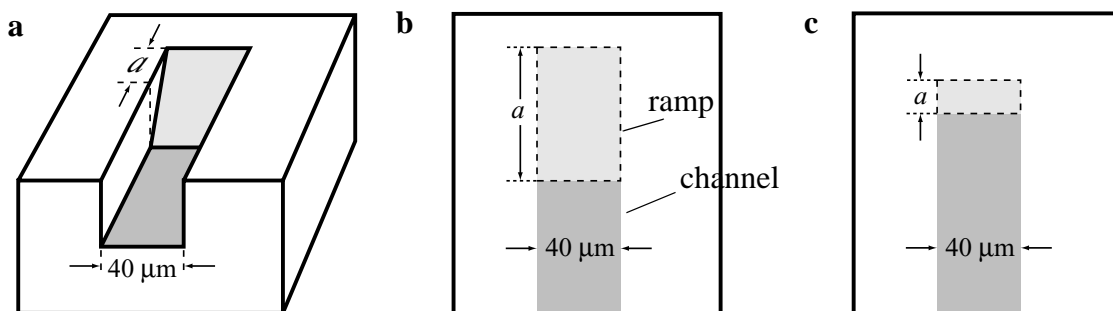


Figure VI.3-3: Schematic of the region near the ablated surface, which is covered by the channel. (a) Three dimensional view. (b) Top view for the case of a long spot length a , i.e. small ϑ . (c) Top view for the case of a short spot length a , i.e. high ϑ .

As it was pointed out and quantified by Miotello *et al.*, the indirect redeposition is most important near the long side of a rectangle [75,85]. An intuitive reason for this behavior, gives the fact

that the yields of formation and redeposition of particulate ablation products are high, if the primary ablation products are confined for a “long” time to a “small” space [81]. Sites where the evacuation of the ablation products is confined by the ablation products of neighboring site are thus preferred for debris redeposition.

The dependence of the relative quantity of indirect debris, redeposited in the channel is illustrated by the charging SEM images in Figure VI.3-4. For channel production with higher ramp angles ϑ the irradiated spot length a was more and more decreased compared to the width of the irradiated spot width (section III.4). In consequence, it is sure that the indirect debris contribution also increases with increasing ramp angle.

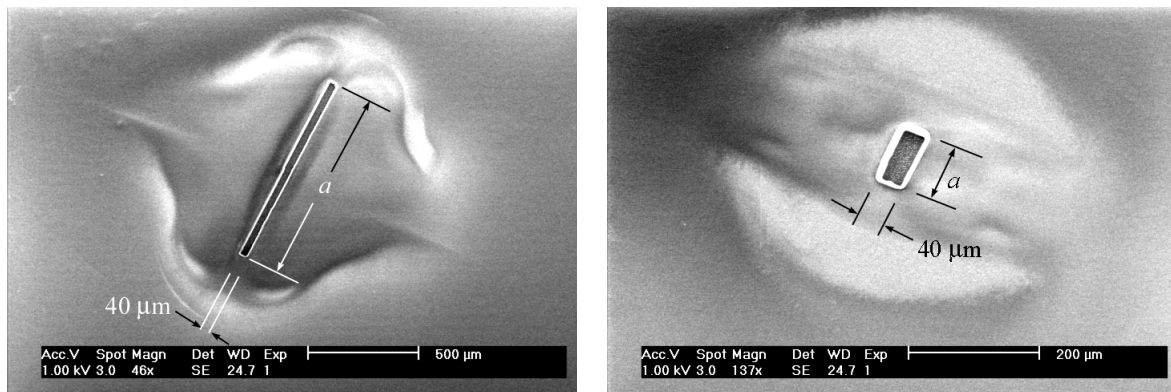


Figure VI.3-4: Charging SEM images showing debris patterns near statically ablated regions with the masks used for channels with (a) $\vartheta = 2.3^\circ$ ($a = 1000 \mu\text{m}$), and (b) $\vartheta = 22^\circ$ ($a = 100 \mu\text{m}$). In the case of short mask length (high ramp angle) more indirect debris redeposits on the $40 \mu\text{m}$ wide band which is occupied by the channel (Figure VI.3-3). ($1200 \text{ mJ}/\text{cm}^2$, $n = 200$)

It is important to keep in mind, that the two tendencies, which were sketched in the last paragraphs, for the direct and the indirect debris respectively, influence one another. For example the channel walls will hinder the expansion of the ablation products at the lower part of the irradiated ramp but not at the higher part. Nevertheless, free expansion of the ablation products is the basic assumption of the model of Miotello and co-workers. Also, the higher the contribution of the direct debris, the lower the input for the collision mechanism yielding indirect debris. Further, it cannot be excluded that the chemical composition of the indirect debris changes with the ramp angle. This because the dynamics of the ablation products and the surrounding atmosphere are altered, giving probably rise to a change in the “average trajectory” of material becoming indirect debris. (Number of collisions with O_2/N_2 .)

The theoretical limit for the direct debris contribution, at $\vartheta = 90^\circ$, is 50% of the ablated material, whereas the theoretical limit for the indirect debris contribution is more difficult to estimate. Probably, it will not exceed half of the indirect debris in Static Ablation.

In conclusion, indirect, hydrophilic debris is most important at low ramp angles, and the quantity, redeposited in the channel, increases with decreasing spot length a , i.e. increasing ramp angle ϑ . Therefore, the hydrophilic behavior of the channel is enhanced by increasing the ramp angle from $\vartheta = 2.3^\circ$ to $\vartheta = 4.3^\circ$, which corresponds to a reduction of the mask length from $a =$

1000 μm to $a = 500 \mu\text{m}$. At higher ramp angles, the more hydrophobic contribution of the direct debris determines the channel surface.

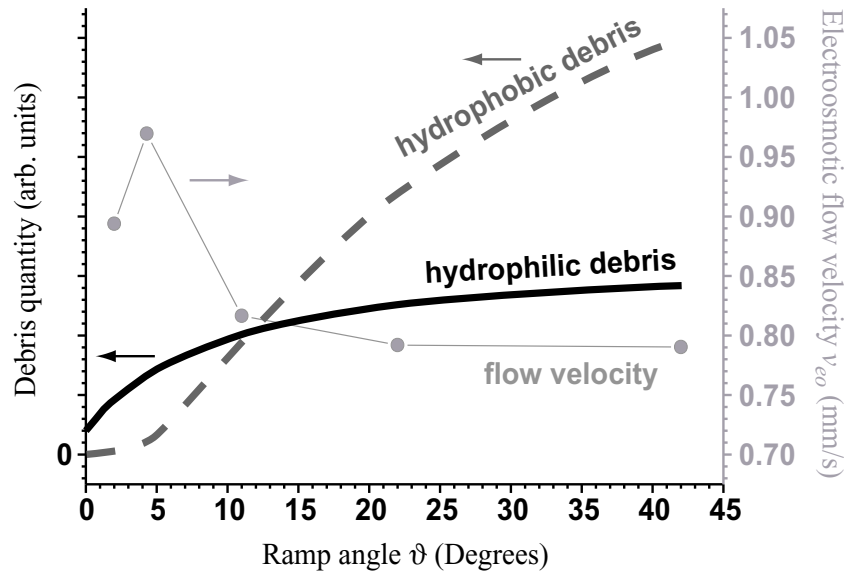


Figure VI.3-5: Schematic showing the competition between indirect and direct redeposition leading to the existence of an optimum ramp angle for highest electroosmotic flow.

VI.4 Zeta potential determination

In order to get information on the ablated surface, a separation of the influences of the laminated surface and of the ablated surface on the observed electroosmotic flow was performed. This is possible as the heterogeneous electroosmotic flow velocity profile in rectangular channels can be calculated (section II.5.3). François Bianchi from the Laboratory of Electrochemistry (EPFL) has performed electroosmotic flow velocity measurements in channels with different depth and constant composition. We implemented the analytical formula of Andreev et al. [106] numerically, in order to perform a fit of the experimental data, yielding the ζ -potential values for the ablated surface and the laminated surface. Precise knowledge about the ζ -potentials of the channel walls is important from an application point of view, because the heterogeneous flow velocity profile gives rise to Taylor-dispersion, which may limit the separation resolution of electrophoresis in composite channels.

VI.4.1 Experiments

The channels for the electroosmotic flow measurements were produced in two different substrate materials (poly(ethylene terephthalate) and polycarbonate). For the production of channels with same width and length and different depths, F. Bianchi used Scanning Ablation with constant spot length and varied the scan speeds. The resulting channels had a trapezoidal cross section [11]. Their depth d_{tot} , their width at the top w_t , and their width at the bottom w_b were measured for each channel. Then the channels were laminated (poly(ethylene) on PET), and the average electroosmotic flow velocity $\langle v_{eo} \rangle$ was measured at $pH = 4.6$ as described in section III.5.1.

VI.4.2 Electroosmotic flow in laminated channels

The electroosmotic flow velocity profile $v_{eo}(x,y)$ in a channel, which is composed of materials with different ζ -potentials, deviates from the classical plug profile (section II.5.3), and can no longer be described by the Schmoluchowsky equation (Eq. 8). An analytical infinite sum description of the electroosmotic flow velocity profile in rectangular micro channels, where each wall may have a different ζ -potential, was given by Andreev et al. (Eq. 9) [106]. Based on this expression, it is possible to predict changes of the *average* electroosmotic flow velocity $\langle v_{eo} \rangle$ (Eq. 11) in rectangular laminated micro channels as a function of the channel cross section.

The channels are described by ζ_s and ζ_l , the ζ -potentials of the substrate and the lamination respectively, and the width l_x and the depth l_y of the channels (Figure VI.4-1a). The numerical implementation of Eq. 9 and Eq. 11 allows for visualization of the electroosmotic flow velocity profile $v_{eo}(x,y)$ in a quadratic channel ($l_x = l_y = 50 \mu\text{m}$) with $\zeta_s = -100 \text{ mV}$ and $\zeta_l = -30 \text{ mV}$ (Figure VI.4-1b). The $\langle v_{eo} \rangle$, given by the numerical implementation, are precise to $\pm 1 \%$ as can be estimated from the numerical tests performed. For details on the numerical implementation of Eq. 9 and Eq. 11 and the convergence tests, please refer to Appendix B.

In the experiments, we measure the average of such flow profiles (grid 500×500 points) over the whole channel cross section. (For the flow profile in Figure VI.4-1b the average is: $\langle v_{eo} \rangle =$

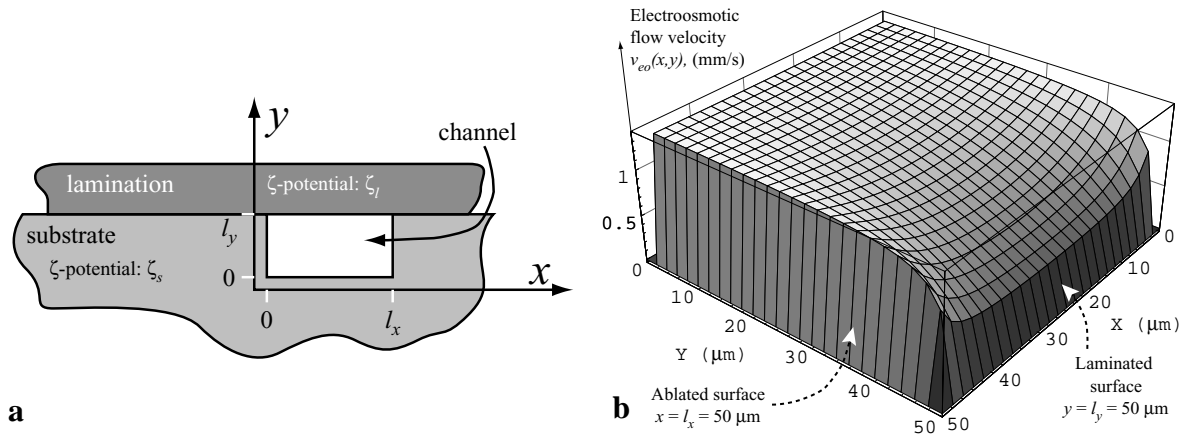


Figure VI.4-1: (a) Schematic defining the parameters, which describe the channels in the calculations. (b) 3D-grey-level-plot of the electroosmotic flow velocity profile $v_{eo}(x,y)$ in a laminated channel. The flow velocity close to the laminated surface (right side in front) is lower due to the lower ζ -potential. Parameters defined below: $l_x = l_y = 50 \mu\text{m}$, $\zeta_s = -100 \text{ mV}$, $\zeta_l = -30 \text{ mV}$, $1/\kappa = 0.1 \mu\text{m}$, $E_z = 20 \text{ kV/m}$. Numerical parameters defined in Appendix B: $k_{up} = 200$, grid 26×26 points.

1.092 mm/s.) Except close to the borders, the *shape* of the flow velocity profile does not depend on the size of the channels, but only on the ratio of channel depth l_y and channel width l_x . Alternatively, the relative contribution of the laminated surface relative to the whole channel surface $r \equiv l_x / (2l_x + 2l_y)$ can be used as parameter. This *lamination ratio* r , which can vary in the range of 0 to 0.5 for laminated channels, was chosen for the abscissa in all viewgraphs describing the dependency of the average electroosmotic flow velocity $\langle v_{eo} \rangle$ on the channel depth. The independence of the velocity profile shape on the channel size is illustrated in Figure VI.4-2 by cross sections of the flow velocity profiles for channels of the same geometry and different scales.

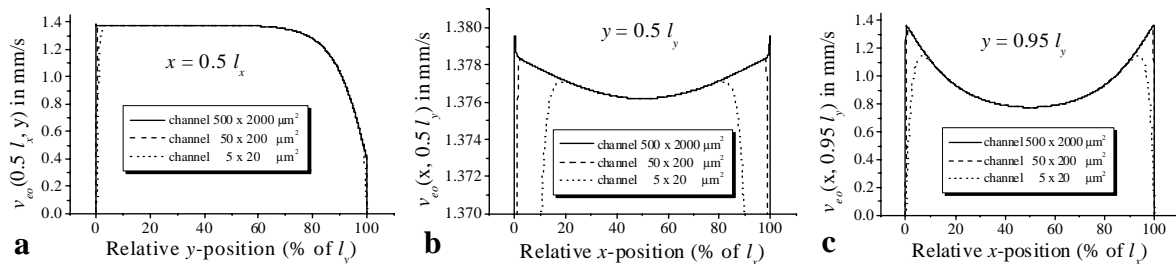


Figure VI.4-2: Cross sections through the flow velocity profiles of channels which are four times deeper than large ($r = 0.1$). The different curves in one graph correspond to different channel widths (500 μm , 50 μm , 5 μm). (a) Shows cross sections along the y-axes at $x = 0.5 l_x$. (b) Shows cross sections along the x-axes at $y = 0.5 l_y$. (c) Shows cross sections along the x-axes at $y = 0.95 l_y$. ($\zeta_s = -100 \text{ mV}$, $\zeta_l = -30 \text{ mV}$, $1/\kappa = 0.1 \mu\text{m}$, $k_{up} = 200$, $E_z = 20 \text{ kV/m}$, sampling step = $0.5 1/\kappa$).

However, the shape of the flow velocity profiles, and also the average flow velocity, both change, when the depth of the channel is changed at constant channel width. Figure VI.4-3a shows cross sections of flow velocity profiles, which illustrate how the shape changes. In the

limit of large and shallow channels the whole velocity profile can be approximated by a plane, i.e. $v_{eo}(x,y)$ is nearly independent of x and linearly dependent on y , with the values close to the channel walls given by the Schmoluchowsky equation. Figure VI.4-3b shows the variation of the average electroosmotic flow velocity $\langle v_{eo} \rangle$ as a function of r . For $r \cong 0.5$, i.e. very shallow channels, the electroosmotic flow decreases, because of the overlapping of the channel floor double layer and the double layer of the laminated surface. This effect was artificially enhanced in the generation of the data by using an unrealistic thick double layer ($1/\kappa = 0.1 \mu\text{m}$).

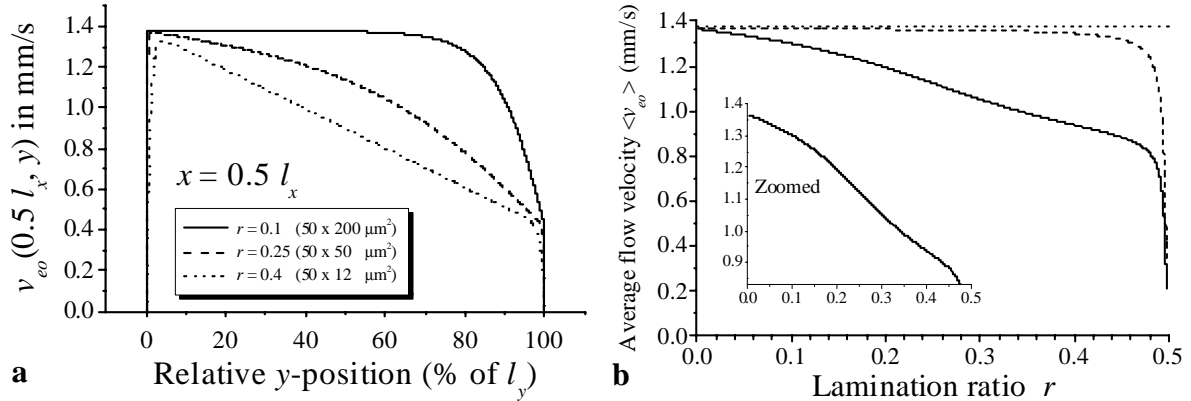


Figure VI.4-3: (a) Cross sections along the y -axes at $x = 0.5 l_x$ through the flow velocity profiles of laminated channels with different depth. (b) Typical dependency of the average electroosmotic flow velocity $\langle v_{eo} \rangle$ on the lamination ratio r (channel depth). Solid line: laminated channel ($\zeta_s = -100 \text{ mV}$, $\zeta_l = -30 \text{ mV}$). Dashed line: homogenous channel ($\zeta_s = \zeta_l = -100 \text{ mV}$), Dotted line: Schmoluchowsky equation ($\zeta = -100 \text{ mV}$).

Parameters: (a) $\zeta_s = -100 \text{ mV}$, $\zeta_l = -30 \text{ mV}$, $1/\kappa = 0.1 \mu\text{m}$, $E_z = 20 \text{ kV/m}$, $k_{up} = 200$, and sampling step = $0.5 1/\kappa$. (b) $1/\kappa$, E_z see (a), grid 500×500 points for all channel geometries, $k_{up} = 50$ for $0.034 < r < 0.466$, and $k_{up} = 200$ for $r \leq 0.034 \wedge r \geq 0.466$.

VI.4.3 Linking model and experiment (approximations)

The cross section of the channels In the calculations, the trapezoidal cross section of the ablated channels was approximated by a rectangular cross section.

The cross section of the ablated channels is trapezoidal with a nearly constant wall angle β of about 74° (Figure III.4-1). More precisely, the channels were $50 \mu\text{m}$ wide, 20 mm long, and their depth varied between $15 \mu\text{m}$ and $60 \mu\text{m}$. The corresponding channel in the calculation was evaluated so that r , the relative contribution of the laminated surface with respect to the total channel surface, was identical in both cases. The width of the channel in the calculation l_x was chosen to correspond to the width of the lamination w_t . In consequence the depth of the channel in the calculation l_y was slightly lower than the measured depth, $l_y \leq d_{tot}$ (Figure VI.4-4). The lamination ratio r of the ablated channels is given by

$$r = w_t \times \left(w_t + w_b + 2 \sqrt{\left(\frac{w_t - w_b}{2} \right)^2 + d_{tot}^2} \right)^{-1} . \quad (20)$$

And hence, the expressions for l_x and l_y of the modelled channel, as a function of the measured values w_t , w_b and d_{tot} of the experimental channel are:

$$l_x = w_t \quad l_y = \frac{1}{2} \times \left(w_b - w_t + \sqrt{4d_{tot}^2 + (w_t - w_b)^2} \right). \quad (21)$$

Figure VI.4-4 shows schematically a cross section of an ablated channel together with the corresponding channel in the calculations. The ratio l_y/d_{tot} only depends on the wall angle β , leading to

$$l_y/d_{tot} = \frac{1}{\sin \beta} - \frac{1}{\tan \beta} \cong 0.75, \quad \text{for } \beta = 74^\circ. \quad (22)$$

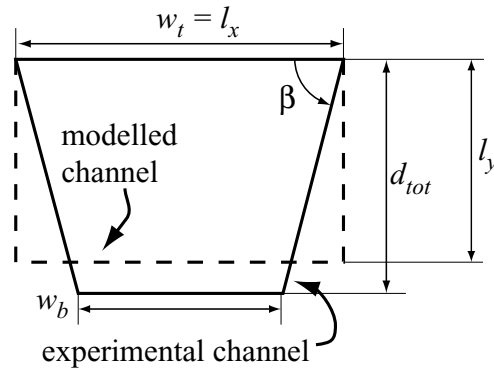


Figure VI.4-4: Schematic of an experimental channel cross section (solid line) and the corresponding rectangular cross section, used in the calculations (dashed line).

The homogeneity of the ζ -potential of all ablated walls In the model calculations, we assumed that all ablated surfaces (channel floor and side walls) exhibit the same ζ -potential, being homogenous over the whole channel length, and being the same for all channels discussed in this section.

The homogeneity of the ζ -potential with the position along the channel can be concluded mostly from the fact that a very thin layer of debris is sufficient for a change of ζ -potential. This is for example visible in the XPS data, where the major changes occurred when going from Static Ablation to Scanning Ablation with $\vartheta = 2.3^\circ$, while only minor changes were observed for Scanning Ablation with different ramp angles. However, direct observation of the debris contribution on the channel floor in section V.4.2 showed that a gradient in debris quantity exists. For high ramp angles ($\vartheta = 17^\circ, 32^\circ$) the determined projection lengths were less than $600 \mu\text{m}$, i.e. $< 3\%$ of the channel length of 20 mm . It is necessary to note however, that the existence of this gradient in debris quantity not necessarily causes a gradient in the ζ -potential of the channel, because very thin layers of debris cannot be detected in SEM (without the charging effect). Even if a gradient in ζ -potential exists, it would be very weak because the situation is nearly symmetrical during the production of the channels ($\vartheta = 0.85^\circ$ to 3.4°). This means, that nearly the same amount of debris is deposited before and behind the irradiated ramp. In summary one can say, that most probably no gradient of the ζ -potential in the channel direction exists, if it exists nevertheless, it is weak and concerns less than 3% of the total channel length.

In section VI.3 it was shown, that the ramp angle influences the ζ -potential of the ablated channels. Especially, a strong dependency was found for low ramp angles ($2.3^\circ - 11^\circ$). As explained before (section VI.3.2), this dependency is caused not so much by the inclination of the irradiated ramp, but by the change in mask geometry. For the channels, which are discussed in this section, F. Bianchi used always the same mask ($50 \times 1000 \mu\text{m}^2$) at different scan speeds, in order to produce channels with constant width and varying depth. The constancy of the spot geometry implies that the quantity and quality of indirect debris is approximately identical for all channels. The ramp angles during production, ranging from 0.85° to 3.4° , are small enough for direct debris to be negligible in all cases. Thus, the assumption, that the ablated surfaces of all channels exhibit the same ζ -potential, is reasonable.

Finally, the third reason for an heterogeneity of the ζ -potential on the ablated surfaces could be a difference of the ζ -potentials of the channel floor and the side walls respectively. As shown in Figure III.4-1 and discussed before, the cross section of the ablated channels is trapezoidal. Consequently the redeposition of material, which is dragged back to the surface, is possible on the channel floor and the channel walls. Though, the channel floor and the channel walls will have roughly the same ζ -potential. The fact that debris redeposits well adherent not only on the channel floor but also on the channel walls is visible in Figure V.4-3.

VI.4.4 Fit results

Figure VI.4-5 shows the experimental data obtained in the two types of channels: ablated poly(ethylene terephthalate) with the poly(ethylene) lamination (PET-PE), and ablated poly(carbonate) with the poly(ethylene) lamination (PC-PE). The curves are generated from the fitting coefficients showed in Table VI.4-1.

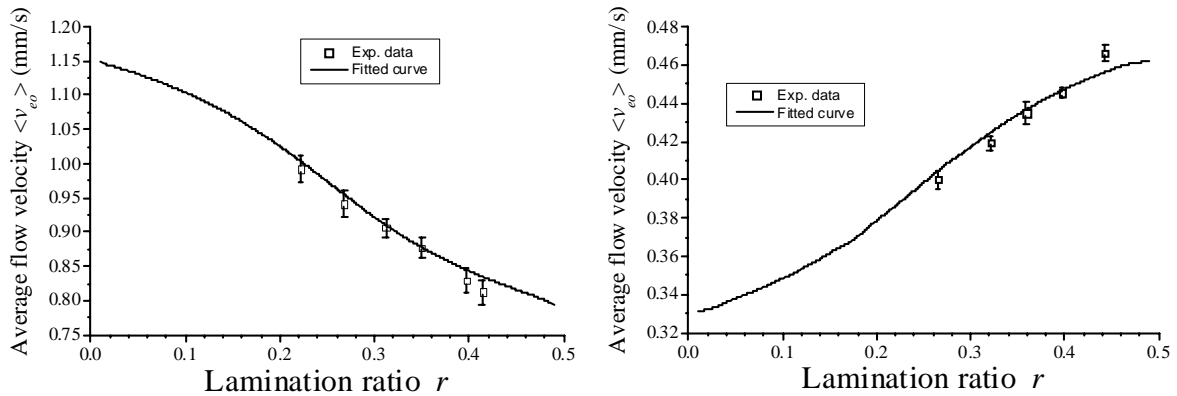


Figure VI.4-5: Average electroosmotic flow velocity $\langle v_{eo} \rangle$ as a function of the lamination ratio r (*buffer pH = 4.6*). Experimental data and fit with Eq. 9 and Eq. 11 (taking into account the relations of section VI.4.3). **(a)** PET-PE channels. **(b)** PC-PE channels.

Table VI.4-1 also shows values, which are obtained using a fitting function proposed by F. Bianchi. As the electroosmotic flow is generated by the electrochemical double layer close to the channel walls, a *linear combination of the classical Schmoluchowsky equations of the two wall materials* (Eq. 23) is useful as an approximation, in order to explain $\langle v_{eo} \rangle(r)$.

		Andreev's formula (Eq. 9 & Eq. 11)	Linear combination (Eq. 23)
PET-PE channel (Figure VI.4-5a)	ζ_{PET}	-84 ± 3 mV	-87 ± 2 mV
	ζ_{PE}	-32 ± 4 mV	-19 ± 3 mV
PC-PE channel (Figure VI.4-5b)	ζ_{PE}	-44 ± 3 mV	-48 ± 2 mV
	ζ_{PC}	-24 ± 2 mV	-22 ± 4 mV

Table VI.4-1: ζ -potential values (pH = 4.6) of the materials composing the micro channels, determined by fitting the experimental data in Figure VI.4-5. The numerical parameters for the fit with Andreev's formula were: $k_{up} = 10$ and grid = 200×200 points (The estimated error due to the numerical approximations is 2.5% in this case (Appendix A)).

$$\langle v_{eo} \rangle \cong \frac{\epsilon_r \epsilon_0 E_z}{\eta} \times [r\zeta_l + (1-r)\zeta_s] \quad (23)$$

The results of the different fitting methods in Table VI.4-1, both show a discrepancy between the values for ζ_{PE} obtained from the different data sets. The error of the average of the two values can be taken as a measure for the quality of the fitting method applied (Table VI.4-2).

	Andreev's formula (Eq. 9 & Eq. 11)	Linear combination (Eq. 23)
$\zeta_{PE}(\text{PET-PE})$	-32 ± 4 mV	-19 ± 3 mV
$\zeta_{PE}(\text{PC-PE})$	-44 ± 3 mV	-48 ± 2 mV
Simple average ζ_{PE}	-38 ± 6 mV	-33.5 ± 14.5 mV
Relative error	16%	43%
Weighted average ζ_{PE}	-39.7 ± 6 mV	-39.1 ± 14.5 mV

Table VI.4-2: ζ -potential values for the PE-lamination (pH = 4.6).

For the fit with Eq. 23, the existence of this discrepancy is not astonishing, because $\langle v_{eo} \rangle(r)$ can be approximated as linear only in a certain range of r -values, and the borders of this range depend on the ζ_s and ζ_l (Figure VI.4-5). However, for the fit with Andreev's expression, the same value for ζ_{PE} is expected for both data sets. The reasons for this error, valid for both fitting methods, are:

1. The error in the experimental data, which is estimated to approximately 10%, due to the fabrication conditions of the channels (Figure VI.3-1).
2. The approximation of the trapezoidal cross section of the ablated channels by a rectangular cross section of the modelled channels.

VI.4.5 Discussion

The knowledge of the ζ -potential values of different materials, composing the micro fluidic channels, allows to evaluate the contribution of the Taylor dispersion to the total dispersion in the system [11]. This is very important, because in the case of PET-PE channels Taylor dispersion limits the separation efficiency of electrophoretic devices realized in this kind of micro channels.

The performed determination of the ζ -potentials of the different materials composing a micro channel may be easier by other means in cases where: (i) the ζ -potentials of the materials are not influenced by the channel fabrication, and (ii) it is possible to produce two homogeneous micro channels separately out of every wall material. In the case of micro channel fabrication by Scanning Excimer Laser Ablation, it would be much more complicated to produce tight channels out of ablated polymer only, and out of heated lamination only, than applying the presented fitting procedure.

Unfortunately, the ζ -potential of the lamination is known only at pH = 4.6 by the experiments presented in this section, whereas the experiments in section VI.3.1 were carried out at pH = 7.2. It is therefore difficult to transform the flow velocity curves as a function of the ramp angle during production (Figure VI.3-1) into ζ -potential curves of the ablated PET surfaces. Values for the average flow velocities in PC-PE channels as a function of pH were published [3], but no data is available on PET-PE channels.

However, there is one hint that the ratio $\zeta_{PE}/\zeta_{PET}=0.38$ is approximately constant in the range from pH = 4.6 to pH = 9.2 [11]. Using this constancy, it is possible to calculate the average flow velocities for possible values of ζ_{PE} in a channel having the cross section of the channels in section VI.3.1 (Figure VI.4-6a). Each pair of ζ_{PE} , ζ_{PET} in Figure VI.4-6a corresponds then to a different buffer pH value. Due to the irradiated spot shape of $1000 \times 40 \mu\text{m}^2$ and the low ramp angles, the debris in the channels in section VI.4.1 is very similar to the debris in the channels with $\vartheta = 2^\circ$ in section VI.3.1. Knowing this, we can determine the values for ζ_{PE} and ζ_{PET} at pH = 7.2, ζ_{PE}^7 and ζ_{PET}^7 respectively, for the channel with $\vartheta = 2^\circ$, by looking up in Figure VI.4-6a at which ζ -potentials the measured value of $\langle v_{eo} \rangle = 0.84 \text{ mm/s}$ was calculated. The interpolation yields $\zeta_{PE}^7 = -29.8 \text{ mV}$ and $\zeta_{PET}^7(\vartheta = 2^\circ) = -78.4 \text{ mV}$.

Using the constancy of $\zeta_{PE}^7 = -29.8 \text{ mV}$ with respect to changes of the ramp angle ϑ during the ablation, it is now possible to determine the variation of the ζ -potential of the ablated surface ζ_{PET}^7 as a function of the ramp angle ϑ during the ablation. For this purpose, the data presented in Figure VI.4-6b was generated. It shows the calculated average flow velocity $\langle v_{eo} \rangle$, as a function of the ζ -potential of the ablated surface (ζ_{PET}^7), and uses the geometrical parameters of the channels in section VI.3.1 and the determined value of $\zeta_{PE}^7 = -29.8 \text{ mV}$. Using the linear fit of Figure VI.4-6b, it is finally possible to find the value of ζ_{PET}^7 yielding a certain measured flow velocity value in Figure VI.3-1. The resulting curves of $\zeta_{PET}^7(\vartheta)$ for the different measurement series are shown in Figure VI.4-7.

The linearity of the plots in Figure VI.4-6 is no approximation, but a fundamental feature of Eq. 9 and Eq. 11. In agreement with the Schmoluchowsky equation, the dependence of the av-

VI.4 ZETA POTENTIAL DETERMINATION

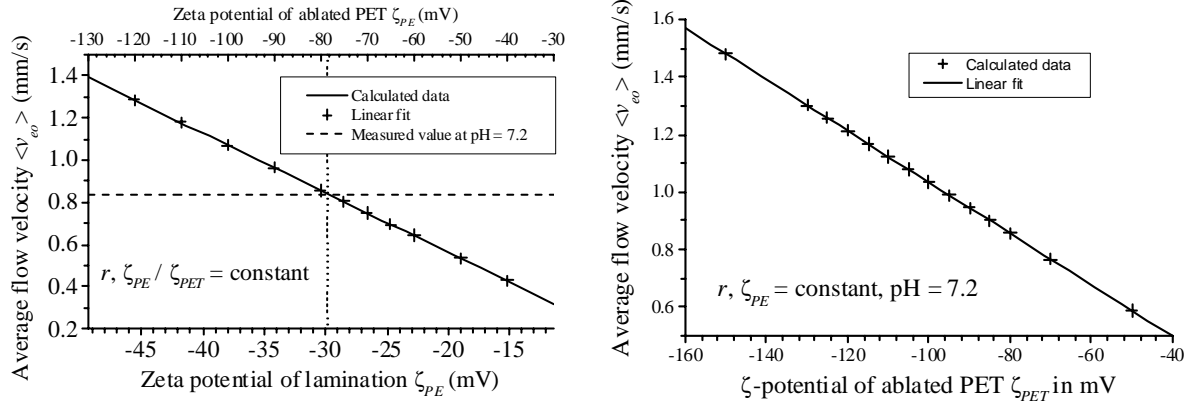


Figure VI.4-6: (a) The average electroosmotic flow velocity $\langle v_{eo} \rangle$ calculated as a function of the ζ -potential of the ablated PET, assuming the ratio ζ_{PE}/ζ_{PET} to be constant and using the cross section of the channels in section VI.3.1 ($r = 0.32$). **(b)** Calculated average flow velocity $\langle v_{eo} \rangle$ in the channels of section VI.3.1, as a function of the ζ -potential of the ablated surface (ζ_{PET}^7). The cross section of the channels and the ζ -potential of the lamination are constant (pH = 7.2).

verage electroosmotic flow velocity on variations of the ζ -potentials is linear, at constant channel cross section. It is

$$\langle v_{eo} \rangle = \text{const}_1(l_x, l_y) \times \zeta_s + \text{const}_2(l_x, l_y) \times \zeta_l \quad (24)$$

The detailed expressions of $\text{const}_1(l_x, l_y)$ and $\text{const}_2(l_x, l_y)$, which cannot be evaluated symbolically, are given in Appendix C.

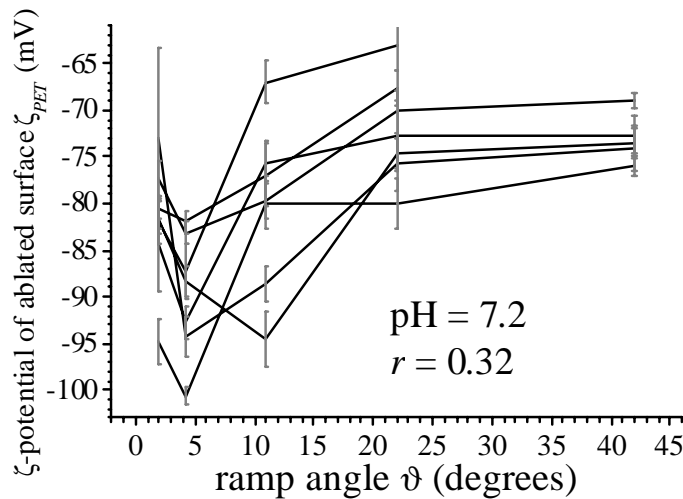


Figure VI.4-7: Figure VI.3-1d transposed to $\zeta_{PET}^7(\vartheta)$ instead of $\langle v_{eo} \rangle(\vartheta)$.

The relative variation of the ζ -potential of the ablated surface $\zeta_{PET}^7(\vartheta)$ is approximately 29% of the maximum (absolute) value, compared to the 25% variation in $v_{eo}(\vartheta)$ (section VI.3).

VI.5 Chapter summary

The chemical composition of the ablated surfaces in the channels, and the electroosmotic flow in the laminated channels were studied.

The presence of two chemically different types of debris, *indirect debris* and *direct debris* respectively, was concluded from XPS measurements, the wetting behavior of debris determined surfaces, and the existence of an optimum ramp angle for highest electroosmotic flow.

Indirect debris was shown to be predominant in channels with low ramp angles. The resulting surfaces are hydrophilic and include oxygen and nitrogen functionalities. More indirect debris is deposited in the channel if the spot length a is small compared to the channel width. *Direct debris*, on the other hand, determines the channel surface at high ramp angles. Direct debris is more hydrophobic than indirect debris but includes also oxygen functionalities. The quantity of direct debris in the channel depends on the ramp angle and can be very important.

In consequence, changing the ramp angle changes the relative importance of the two types of debris in the channel. This explains the observed optimum ramp angle for maximum electroosmotic flow at constant channel cross-section.

Since not all channel walls are ablated surfaces, the measured electroosmotic flow depends also on the relative surface covered by the forth wall, i.e. the PE-lamination. This influence causes a variation of the electroosmotic flow at constant debris composition in the channel, if the depth of the channel is changed. This variation of the electroosmotic flow does not depend on the scale of the channel but only on the ratio channel width / channel depth. A numerical fit to the experimental data, using a complicated analytical expression for the electroosmotic flow [106], allowed for separation of the influence of the ablated surfaces and the lamination on the measured electroosmotic flow. After determination of the ζ -potentials of lamination and ablated surface at constant debris composition, it is possible to determine the variation of the ζ -potential of the ablated surfaces due to the different quantities of direct and indirect debris. Variation of the ramp angle from 2° to 42° changes the ζ -potential of the ablated channel surface by approximately 30% of its maximum value.

Hence, controlled variations of the chemical surface composition of the micro channels are possible by Scanning Ablation.

VII. Conclusion and outlook

The results of the present work clearly show that substrate scanning upon Excimer Laser Ablation leads to important modifications in the topography and chemistry of the ablated surfaces compared to Static Ablation. This is important for products and devices where the *wettability*, the *adhesion*, the ζ -*potential* or the *micro/nano roughness* of the ablated surfaces are key factors.

Structure changes: The topographical structure changes, which were observed upon Scanning Ablation of stretched polymers, were attributed to the changing geometrical orientation of the irradiated surface with respect to the frozen-in stress field of the substrate.

In fact, upon Scanning Ablation the irradiated surface has the form of a ramp, which is inclined by the ramp angle with respect to the non-irradiated surface. It is the structure on the lower part of this ramp, that determines the structure on the channel floor. For ramp angles lower than approximately 12° , the structure on the irradiated ramp is the same as on statically (flat) ablated surfaces. The orientation of the structure changes at ramp angles between 12° and 30° . In this range the structure orientation coincides with the channel direction, whereas the structure orientation is normally perpendicular to the direction of the frozen stresses [56]. At very high ramp angles, the ramps become smooth.

The two structure changes on the ramps can be described by a model, where the component of the frozen stresses, which is perpendicular to the irradiated ramp, suppresses the structure formation, first for tangential stress component down the ramp and then for the stress component parallel to the ramp border. An experiment with differently stretched PET showed that the limiting angles of the structure changes are independent of the total amount of frozen stresses in the polymer. In other words, the ratio of the perpendicular stress to the tangential stress components is the important value for the structure changes to occur. Experiments at different fluences and in different substrates showed that the limiting angles for the structure changes do not depend on the laser fluence, but do depend on the substrate material.

The channel floor cannot become completely smooth, but the orientation of its structure changes as described above and at the same ramp angles. However the structure in the channel has a second nanometric component in addition to the micrometric component just described. This nanometric structure is due to strongly enhanced redeposition of ablated material (debris) on the channel floor and the channel walls. At high ramp angles, the debris can fill up the valleys of the micrometric structure, and thus determines the structure on the channel floor. It consists of porous material, which was shown to be strongly adherent to the channel floor and walls.

The orientation of the micrometric structure at ramp angles below 22° did not influence the average electroosmotic flow velocity of the buffer solution in the fabricated 40 micron deep channels. The presence of the structure may have a slight influence, but further investigations would be necessary in order to prove this effect.

Moreover, further investigations on the fundamental process underlying the formation of the micrometric structure in polymers, would help improving the presented idea of vector decomposition of frozen stresses upon their relaxation. Especially, the knowledge of the relative

VII. CONCLUSION AND OUTLOOK

amounts of frozen stresses, compared to the laser heating induced stresses, in the initial stage of the structure formation, could confirm or contradict the idea of a relative suppression threshold in the perpendicular stress component. This work can only be performed if it is possible to express the quantity “frozen stresses” by polymer physico-chemical properties, as chain alignment, interaction between chains, crystallinity etc.. Qualitative ideas for this purpose were given in this work but the quantification is necessary, if knowledge on the relative importances of frozen stresses and laser induced heating stresses is the aim. Another fundamental question, which shows up is why the perpendicular stress component acts differently on the tangential component down the ramp, than on the tangential component parallel to the ramp border. Most probably the answer lies also in a better understanding of the relation between real polymer properties and the concept of frozen stresses.

From the application point of view, the obtained results could be a tool for attempts of spatially patterned functionalization of the channel floor, which may be interesting in the domain of biological applications of micro fluidics. Producing flat channels in uniaxially stretched polymers, with arbitrary orientation of the micrometric structure with respect to the channel direction, could be also interesting in this domain. However, the know-how for this is already 9 years old [56].

Debris: The observed variations in the chemical composition were only attributed to a change in redeposition of well adherent debris. The total debris contribution was assumed to be a mixture of two distinct types of debris: indirect debris and direct debris. This assumption certainly simplifies the situation, but it was possible to explain all obtained data within this framework. The quantity of the different debris types, which is redeposited in the micro channels, changes when changing the shape of the irradiated spot and/or the ramp angle.

Indirect debris is the “classical” type of debris, which is observed after Static Ablation near the irradiated area. It redeposits due to the drag forces of the shock wave forming upon Laser Ablation in ambient atmosphere [84]. The condensing experiment showed that the collisions with the molecules of the ambient atmosphere give rise to chemical modifications of this kind of debris. Compared to a statically ablated surface, surfaces which are covered by indirect debris contain more oxygen and nitrogen, as detected by XPS. Also the surface is hydrophilic as shown by the condensing experiment. The quantity of indirect debris is determined by the shape of the irradiated region, and only indirectly by the ramp angle.

Direct debris redeposits due to a PLD like process, i.e. the ablation products are directly ejected in the direction of the channel floor, and no collisions with the molecules of the ambient atmosphere are necessary for this kind of debris. This kind of debris is special to Scanning Ablation, and is only important at high ramp angles. Compared to indirect debris, direct debris was shown to be more hydrophobic. Nevertheless, it contains approximately the same amount of oxygen.

Real debris is in general none of these two distinctly defined limiting cases of debris. The real physical process is not the production of two types of debris, their mixing, and the redeposition of the mixture. On the contrary, we should speak of a probability of the real debris to react with oxygen or nitrogen, and its redeposition yield, which both depend on the ramp angle and the shape of the irradiated spot. However, the experiments show, that the redeposition yield and the

probability of reaction with the ambient atmosphere are correlated. This is why the chosen simplified description is successful for the explanation of the observed effects. Some uncertainties however remain, for example the following question: is the indirect debris, which was observed in the condensing experiment the same indirect debris as the one which was observed by XPS in large channels? Further theoretical work should aim at giving a description of the observed effects, staying closer to the physical process of the ejection of the ablation products, the possible reactions with the ambient atmosphere, and the possible redeposition.

Electroosmosis: The applied model of the changing ratio indirect / direct debris did nevertheless succeed to explain the observed maximum of the electroosmotic flow velocity.

The fact that direct debris is dominating at high ramp angles and negligible at low ramp angles, explained the decrease of the observed electroosmotic flow velocity at ramp angles higher than the optimum value of 4.3° . The increase at ramp angles lower than 4.3° , could be explained by the increasing redeposition of the indirect debris on the surface which is occupied by the already fabricated channel, due to the shorter irradiated spot length at higher ramp angles. The variation of the electroosmotic flow velocity with varying Scanning Ablation parameters corresponds to a variation of the ζ -potential of the ablated surfaces in the channel.

This variation was determined based on a separate measurement, which allowed for the separation of the influences exerted by the ablated surfaces and the lamination, and thus yielded the ζ -potentials of ablated surface and lamination at a buffer pH of 4.6. The obtained absolute values for the ζ -potentials of the ablated surfaces at pH = 7 are based on the rather weak assumption that the ratio ζ_{PET} / ζ_{PE} is the same at pH = 4.6 and pH = 7. The result of the deconvolution showed that the ζ -potentials of the ablated surfaces can be varied in a range of about 30% of their maximum value by varying the Scanning Ablation parameters.

This special capacity of Scanning Ablation could be exploited in the future in order to produce a gradient of ζ -potentials somewhere in a channel. The practical solution of the problem is just a question of programming the computer controlled x-y-table, where the sample is mounted on, and another motor which opens or closes the mask during the ablation. This would allow to produce devices based on the combination of a chromatographic separation method and capillary electrophoresis. For the production of long-living devices by Scanning Excimer Laser Ablation, a more profound understanding of the aging processes of the debris would be very useful. First indications were given in this report, i.e. the debris becoming richer in carbon after four months, but the dynamics of the aging on a time-scale of some weeks remains unknown. Because PET is a “fast aging polymer”, the role of the substrate material in the aging process of the channel surface would also be interesting and not too difficult to investigate.

In conclusion, Scanning Ablation changes all surface properties of the micro channels, except the thickness of the amorphous layer.

VII. CONCLUSION AND OUTLOOK

Appendix A: Development of the Static Structure with the number of pulses

A.1 As observed by Static Ablation

The development of the Static Structure with the number of incident pulses was reported and analyzed in detail by others [58,59]. Here, the interest of showing the SEM images in Figure A.1-1 is to give a better impression of the different forms of the Static Structure, and to demonstrate how the temporal development of the structure is resolved in space on ramps, which are formed by a number-of-shots-gradient (section A.2).

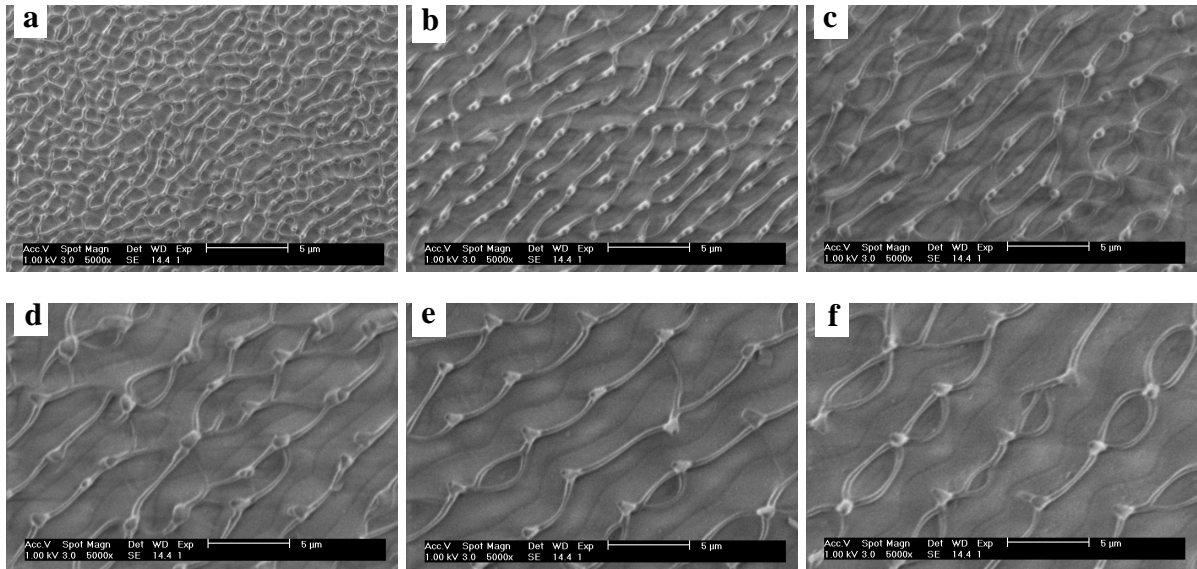


Figure A.1-1: Static Ablation of the biaxially stretched substrate ($\Phi = 1200 \text{ mJ/cm}^2$). Series of different number of shots n_s : (a) $n_s = 3$, (b) $n_s = 10$, (c) $n_s = 20$, (d) $n_s = 50$, (e) $n_s = 100$, (f) $n_s = 300$.

A.2 As observed by Scanning Ablation

The ramps, forming at the beginning and the end of the channels in Scanning ablation, are caused by a number-of-shots-gradient. In consequence, the increase of the structure size with the number of pulses n_s (Figure A.1-1) can be observed in the range $n_s \in [1, n]$ on the ramps of channels produced with n shots per site (Figure A.2-2). This is true for both the scanning structure (Figure A.2-2b) and the static structure (Figure A.2-2a).

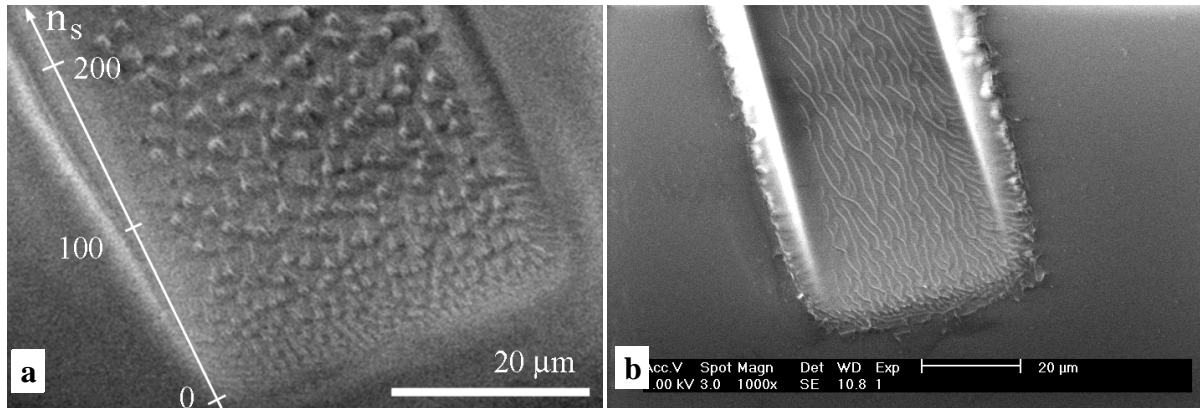


Figure A.2-2: Variation of structure size due to shot number gradient on the end ramps. **(a)** Static Structure. (Scanning Ablation, $n = 200$, $\Phi = 75 \text{ mJ/cm}^2$, $a = 50 \text{ }\mu\text{m}$, $\vartheta = 10^\circ$.) **(b)** Scanning Structure. (Scanning Ablation, $n = 200$, $\Phi = 600 \text{ mJ/cm}^2$, $a = 100 \text{ }\mu\text{m}$, $\vartheta = 19^\circ$.)

Appendix B: Numerical implementation of Eq. 9 and Eq. 11

B.1 The implemented equations (approximations)

As in the experiments the average electroosmotic flow velocity $\langle v_{eo} \rangle$ in our composite channels is detected, it was necessary to implement the calculation of the velocity profile $v_{eo}(x, y)$, given by Eq. 9, and the average over the velocity profile, given by Eq. 11.

The implemented forms of Eq. 9 and Eq. 11, which define the parameters, describing the precision of the numerical approximation of the value of $\langle v_{eo} \rangle$ are then

$$v_{eo}(x, y) = -\frac{4b_0^2}{\pi} \times \sum_{k=0}^{k_{up}} \left\{ \frac{\sin(p_k y)}{2k+1} \left(\zeta_1 \left[\frac{\sinh(p_k x)}{\sinh(p_k l_x)} - \frac{\sinh(q_k x)}{\sinh(q_k l_x)} \right] + \zeta_2 \left[\frac{\sinh(p_k(l_x - x))}{\sinh(p_k l_x)} - \frac{\sinh(q_k(l_x - x))}{\sinh(q_k l_x)} \right] \right) \right. \\ \left. + \frac{\sin(m_k x)}{2k+1} \left(\zeta_3 \left[\frac{\sinh(m_k y)}{\sinh(m_k l_y)} - \frac{\sinh(n_k y)}{\sinh(n_k l_y)} \right] + \zeta_4 \left[\frac{\sinh(m_k(l_y - y))}{\sinh(m_k l_y)} - \frac{\sinh(n_k(l_y - y))}{\sinh(n_k l_y)} \right] \right) \right\} \quad (\text{B-1})$$

and

$$\langle v_{eo} \rangle = \frac{1}{N_x N_y} \times \sum_{i=1}^{N_x} \sum_{j=1}^{N_y} v_{eo}(x_i, y_j), \text{ with } x_i, y_j \text{ regularly spaced between } 0 \text{ and } l_x, l_y \quad (\text{B-2})$$

respectively.

The numerical parameters are k_{up} , the number of sum terms being considered in Eq. B-1 (instead of infinity), and $N_x \times N_y$ the grid size, giving the number of points, which are used for the sampling of the velocity profile in Eq. B-2 (instead of infinity).

One problem showed up in the implementation of Eq. B-1: when using the realistic Debye length $1/\kappa$ of about 3 nm, numerical overflow occurred at high r -values, i.e. low l_x/l_y , during the calculation of the sinh-expressions. In order to avoid this, the arguments of the sinh-functions were tested before evaluation and the fractions of the form $\sinh(\dots)/\sinh(\dots)$, which are indicated by the numbers 1 to 8 in Eq. B-1, were approximated if necessary.

The fractions 1, 2, 5 and 6 in Eq. B-1 are of the form

$$\frac{\sinh(c_1 x)}{\sinh(c_1 c_2)}, \quad \text{with } c_1, c_2 = \text{constant}. \quad (\text{B-3})$$

Using the definition of the sinh-function ($\sinh x = (e^x - e^{-x})/2$) one obtains for high c_1 :

$$\frac{\sinh(c_1 x)}{\sinh(c_1 c_2)} \approx e^{c_1(x - c_2)}, \quad \text{with } c_1, c_2 = \text{constant, and } c_1 \gg c_2, x. \quad (\text{B-4})$$

The fractions 3, 4, 7 and 8 in Eq. B-1 are of the form

$$\frac{\sinh(c_1(c_2 - x))}{\sinh(c_1 c_2)}, \quad \text{with } c_1, c_2 = \text{constant}. \quad (\text{B-5})$$

Again using the definition of the sinh-function one obtains for high c_1 :

$$\frac{\sinh(c_1(c_2 - x))}{\sinh(c_1 c_2)} \approx e^{-c_1 x}, \text{ with } c_1, c_2 = \text{constant, and } c_1 \gg c_2, x. \quad (\text{B-6})$$

B.2 Numerical tests, convergence and precision

The convergence of the numerically calculated average flow velocity $\langle v_{eo} \rangle$ was quantified by the tests shown in Figure B.2-1. The convergence was evaluated independently for each parameter k_{up} and N (grid $N \times N$), while keeping the second parameter constant at a rather high value. The graphs show the resulting curves for different channel depths (r -values).

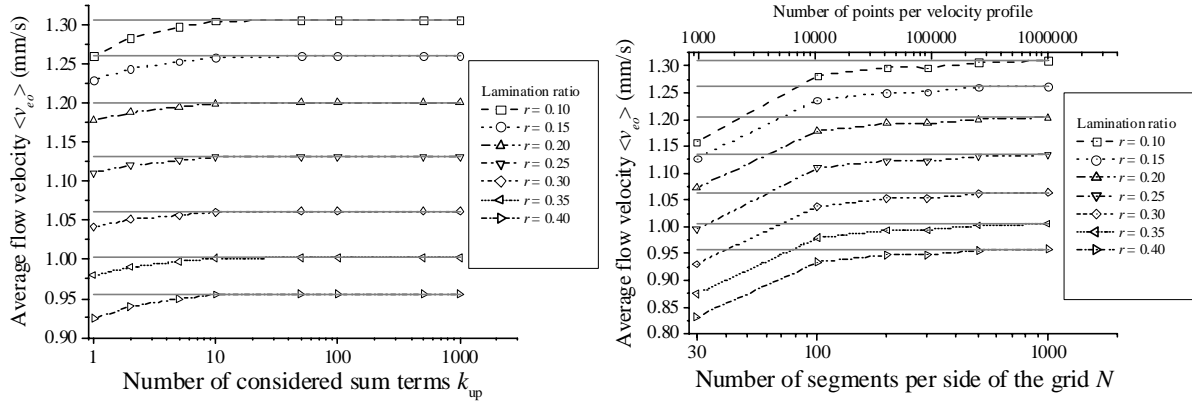


Figure B.2-1: (a) Dependence of the numerically calculated average flow velocity $\langle v_{eo} \rangle$ as a function of k_{up} (grid size fixed to 500×500 points). (b) Dependence of the calculated $\langle v_{eo} \rangle$ as a function of the symmetric grid size (k_{up} fixed to 200).

The convergence of $\langle v_{eo} \rangle$ as a function of k_{up} was observed to be practically independent of r , whereas $\langle v_{eo} \rangle$ as a function of N converged slightly faster for lower r -values than for higher r -values. Reasonable values for the considered sum terms and the grid are thus:

$$k_{up} = 50 \quad \text{and} \quad N \times N = 500 \times 500. \quad (\text{B-7})$$

One might argue that a fixed number of grid points, as chosen here, is not adapted to the sampling of channels of equal width and different depth, because the sampling step in the y -direction is different for the different channels. In order to estimate the development of the numerically calculated $\langle v_{eo} \rangle$ with decreasing sampling step, one has to consider the scales of the channel dimensions ($l_x, l_y \cong 50 \mu\text{m}$) and the Debye layer thickness ($1/\kappa \cong 3 \text{ nm}$, for $[\text{ion}] \cong 9 \text{ mMol/l}$). In order to resolve the Debye layer the sampling step has to be less than half of the Debye layer thickness (Figure VI.4-2), i.e. sampling step = 1.5 nm. For a channel with a cross section of $50 \times 50 \mu\text{m}^2$ this results in a grid of $N \times N = 33333 \times 33333 \cong 1 \times 10^9$ points. In other words, the Debye layer is in general not resolved in the numerical calculations of $\langle v_{eo} \rangle$. For very high values of r ($r > 0.4926$), i.e. very shallow channels, the debye layer is resolved in y -direction, when working with a grid of 500×500 points.

However, the resolution of the Debye layer is not necessary for big enough channel cross sections if a small error is accepted. In the calculation, all points at the border of the grid are set to zero. Thus, the influence of the Debye layer is over-estimated for the situations where it is not resolved. Table B.2-1 gives the relative number of the border points ($2N + 2(N - 2)$) with re-

spect to the whole number of points ($N \times N$) for symmetric grids. This value can be used as an estimation of the error due to the fact that the Debye layer is not resolved. For comparison, the relative channel surface, occupied by the Debye layer is $< 1\%$ for $r < 0.494$, when dealing with $50 \mu\text{m}$ wide channels.

Grid size	30×30	100×100	200×200	300×300	500×500	1000×1000
Importance of border	12.9%	4.0%	2.0%	1.3%	0.8%	0.4%

Table B.2-1: Estimation of the error in the numerical calculation of $\langle v_{eo} \rangle$, due to the use of a finite grid size for the averaging.

In consequence, the calculated $\langle v_{eo} \rangle$ are exact within 1% of precision, if the channels are $50 \mu\text{m}$ wide, not too shallow ($r < 0.49$), and a grid of at least 500×500 points is used.

B.3 Software

The numerical implementations were performed in different environments. “Mathematica” was used for the first tests, because it increases the working precision until a fixed precision of the result is achieved. In consequence the approximations (Eq. B-4 and Eq. B-6) were not necessary. The disadvantage of “Mathematica”, at least if it calculates with high precision, is that it is very slow. For higher speed, Eq. B-1 and Eq. B-2 were implemented in “Delphi” (former “Pascal”), using the 10 byte data type for highest possible precision (19-20 significant digits, upper limit = 1.1×10^{4932}). This implementation was used to generate the plots presented in this section. Finally, for the fitting of the experimental data the implementation was translated to the programming language of Igor Pro (Version 3.14).

Appendix C: Linearity of Eq. 9 at constant channel cross section

C.1 Explicit form of $\text{const}_1(l_x, l_y)$ and $\text{const}_2(l_x, l_y)$ in Eq. 24

Andreev *et al.* [106] gave the following expression for the electroosmotic flow velocity profile v_{eo} in a rectangular micro channel (Eq. 9):

$$v_{eo}(x, y) = -\frac{4b_0^2}{\pi} \times \sum_{k=0}^{\infty} \left\{ \frac{\sin(p_k y)}{2k+1} \left(\zeta_1 \left[\frac{\sinh(p_k x)}{\sinh(p_k l_x)} - \frac{\sinh(q_k x)}{\sinh(q_k l_x)} \right] + \zeta_2 \left[\frac{\sinh(p_k(l_x - x))}{\sinh(p_k l_x)} - \frac{\sinh(q_k(l_x - x))}{\sinh(q_k l_x)} \right] \right) \right. \\ \left. + \frac{\sin(m_k x)}{2k+1} \left(\zeta_3 \left[\frac{\sinh(m_k y)}{\sinh(m_k l_y)} - \frac{\sinh(n_k y)}{\sinh(n_k l_y)} \right] + \zeta_4 \left[\frac{\sinh(m_k(l_y - y))}{\sinh(m_k l_y)} - \frac{\sinh(n_k(l_y - y))}{\sinh(n_k l_y)} \right] \right) \right\} \quad (\text{C-1})$$

Here p_k, q_k, m_k and n_k are simple functions, depending only on the channel dimensions l_x, l_y , the Debye length κ , and the sum counter k . Also, $b_0, \zeta_1, \zeta_2, \zeta_3$ and ζ_4 are constants, independent of the sum counter k as well as the variables x and y . Especially for laminated channels, $\zeta_3 = \zeta_l$, and $\zeta_1 = \zeta_2 = \zeta_4 = \zeta_s$, the ζ -potentials of the lamination and the substrate respectively.

One can thus rewrite Eq. 9:

$$v_{eo}(x, y) = \zeta_l \left(-\frac{4b_0^2}{\pi} \sum_{k=0}^{\infty} \left\{ \frac{\sin(m_k x)}{2k+1} \left[\frac{\sinh(m_k y)}{\sinh(m_k l_y)} - \frac{\sinh(n_k y)}{\sinh(n_k l_y)} \right] \right\} \right) \\ + \zeta_s \left(-\frac{4b_0^2}{\pi} \sum_{k=0}^{\infty} \left\{ \left(\frac{\sin(p_k y)}{2k+1} \left[\frac{\sinh(p_k x)}{\sinh(p_k l_x)} - \frac{\sinh(q_k x)}{\sinh(q_k l_x)} \right] \right) + \left(\frac{\sin(p_k y)}{2k+1} \left[\frac{\sinh(p_k(l_x - x))}{\sinh(p_k l_x)} - \frac{\sinh(q_k(l_x - x))}{\sinh(q_k l_x)} \right] \right) \right. \right. \\ \left. \left. + \left(\frac{\sin(m_k x)}{2k+1} \left[\frac{\sinh(m_k(l_y - y))}{\sinh(m_k l_y)} - \frac{\sinh(n_k(l_y - y))}{\sinh(n_k l_y)} \right] \right) \right\} \right) \quad (\text{C-2})$$

Averaging of $v_{eo}(x, y)$ (Eq. 11) yields:

$$\langle v_{eo} \rangle = \zeta_l \left(-\frac{4b_0^2}{\pi l_x l_y} \int_0^{l_x} \int_0^{l_y} \sum_{k=0}^{\infty} \left\{ \frac{\sin(m_k x)}{2k+1} \left[\frac{\sinh(m_k y)}{\sinh(m_k l_y)} - \frac{\sinh(n_k y)}{\sinh(n_k l_y)} \right] \right\} dy dx \right) \\ + \zeta_s \left(-\frac{4b_0^2}{\pi l_x l_y} \int_0^{l_x} \int_0^{l_y} \sum_{k=0}^{\infty} \left\{ \left(\frac{\sin(p_k y)}{2k+1} \left[\frac{\sinh(p_k x)}{\sinh(p_k l_x)} - \frac{\sinh(q_k x)}{\sinh(q_k l_x)} \right] \right) + \left(\frac{\sin(p_k y)}{2k+1} \left[\frac{\sinh(p_k(l_x - x))}{\sinh(p_k l_x)} - \frac{\sinh(q_k(l_x - x))}{\sinh(q_k l_x)} \right] \right) \right. \right. \\ \left. \left. + \left(\frac{\sin(m_k x)}{2k+1} \left[\frac{\sinh(m_k(l_y - y))}{\sinh(m_k l_y)} - \frac{\sinh(n_k(l_y - y))}{\sinh(n_k l_y)} \right] \right) \right\} dy dx \right) \quad (\text{C-3})$$

For a given channel cross section, i.e. $l_x, l_y = \text{constant}$, both expression in the parentheses following the ζ -potentials are constant. Thus we can write (Eq. 24):

$$\langle v_{eo} \rangle = \text{const}_1(l_x, l_y) \times \zeta_s + \text{const}_2(l_x, l_y) \times \zeta_l \quad (\text{C-4})$$

with

APPENDIX C.1 EXPLICIT FORM OF $CONST_1(L_x, L_y)$ AND $CONST_2(L_x, L_y)$ IN EQ. 24

$$\begin{aligned} \text{const}_1(l_x, l_y) = & -\frac{4b_0^2}{\pi l_x l_y} \int_0^{l_x} \int_0^{l_y} \sum_{k=0}^{\infty} \left\{ \left(\frac{\sin(p_k y)}{2k+1} \left[\frac{\sinh(p_k x)}{\sinh(p_k l_x)} - \frac{\sinh(q_k x)}{\sinh(q_k l_x)} \right] \right) + \left(\frac{\sin(p_k y)}{2k+1} \left[\frac{\sinh(p_k(l_x-x))}{\sinh(p_k l_x)} - \frac{\sinh(q_k(l_x-x))}{\sinh(q_k l_x)} \right] \right) \right. \\ & \left. + \left(\frac{\sin(m_k x)}{2k+1} \left[\frac{\sinh(m_k(l_y-y))}{\sinh(m_k l_y)} - \frac{\sinh(n_k(l_y-y))}{\sinh(n_k l_y)} \right] \right) \right\} dy dx \end{aligned} \quad (\text{C-5})$$

and

$$\text{const}_2(l_x, l_y) \equiv -\frac{4b_0^2}{\pi l_x l_y} \int_0^{l_x} \int_0^{l_y} \sum_{k=0}^{\infty} \left\{ \frac{\sin(m_k x)}{2k+1} \left[\frac{\sinh(m_k y)}{\sinh(m_k l_y)} - \frac{\sinh(n_k y)}{\sinh(n_k l_y)} \right] \right\} dy dx . \quad (\text{C-6})$$

In other words, the average electroosmotic flow velocity is linearly dependent on the different ζ -potentials, as long as the cross section of the channel is constant. However the constants of this linear relationship (Eq. C-4) cannot be evaluated symbolically.

Appendix D: List of symbols and abbreviations

D.1 Symbols used (alphabetical order)

\times	Explicit multiplication sign.
\cong	Approximately equal.
\equiv	Defined as.
a	Spot length of light on the sample, measured in scanning direction.
α_{eff}	Effective high intensity absorption coefficient in Beer's law.
b_0	Constant in Andreev's formula.
β	Wall angle (vertical = 90°)
d_{tot}	Multiple pulse structure depth, mostly channel depth.
DR	Draw ratio of stretched polymer samples. $DR = l_s / l_o$
ΔP	Pressure difference, inducing pressure driven flow.
Δx	Resolution of the mask projection.
e	Euler constant.
e_0	Electron charge.
\vec{E}_z	Driving field of the electroosmotic flow (in channel direction).
E_z	Absolute value of \vec{E}_z (without sign).
ϵ_0	Dielectric vacuum permittivity.
ϵ_r	Relative dielectric permittivity of electrolyte.
f	Pulse repetition rate.
φ	Solid angle in the density distribution of the ejected particles.
ϕ	Angle between S and S_i .
Φ	Laser fluence per pulse, usually in mJ/cm^2 .
Φ_0	Ablation threshold fluence.

APPENDIX D.1 SYMBOLS USED (ALPHABETICAL ORDER)

γ	Equilibrium contact angle.
γ_a	Advancing contact angle.
γ_r	Receding contact angle.
$h(\Phi)$	Ablation rate per pulse at fluence Φ .
η	Viscosity of electrolyte.
k_B	Boltzmann constant.
k_{up}	Upper k-value (counter) in the numerical approximation of the infinite sums.
$1/\kappa$	Debye length (Debye layer thickness).
l_a	Polymer sample length after stretching and annealing.
l_o	Original polymer sample length.
l_s	Polymer sample length after stretching.
l_x	Width of the channel in the calculation (a in the Andreev's paper).
l_y	Depth of the channel in the calculation (b in the Andreev's paper).
λ	Wavelength.
Λ	Lateral size (period) of static structure.
m_k	Simple function in Andreev's formula.
n	Number of pulses per site.
n_k	Simple function in Andreev's formula.
n_s	Applied shot number (Appendix A).
p	Exponent in the density distribution of the ejected particles.
p_k	Simple function in Andreev's formula.
$\langle P_2 \cos \theta \rangle$	Second momentum of the statistical chain orientation function. The higher $\langle P_2 \cos \theta \rangle$, the better the chains are aligned.
q_k	Simple function in Andreev's formula.
r	Ratio of laminated surface and total channel surface (e/f in our paper).

RR	Relative retraction of stretched polymer after annealing. $RR = l_s/l_a$
$\rho(\varphi)$	Density distribution of ejected particles: $\rho(\varphi) = \rho_0 \times \cos(\varphi)^p$
ρ_0	Normalization factor in the density distribution of the ejected particles.
S	Frozen stress in the stretched polymer sample.
S_a	Stress component parallel to the ramp border and parallel to the sample surface.
S_i	Stress component in the direction of the ramp and parallel to the sample surface.
S_p	Stress component in the direction of the ramp and parallel to the irradiated surface.
S_{\perp}	Stress component in the direction of the ramp and normal to the irradiated surface.
σ_{XY}	Interfacial energy per surface area (surface tension) of the interface formed by compound X and Y .
T	Absolute temperature (Kelvin).
τ	Pulse duration.
ϑ	Ramp angle, usually in degrees
ϑ'	First limiting angle. Between static and scanning structure.
ϑ''	Second limiting angle. Between scanning structure and smooth ablation.
v	Scanning speed.
v_{eo}	Electroosmotic flow velocity of the buffer solution in the channel.
$\langle v_{eo} \rangle$	Average electroosmotic flow velocity in the channel. ($= v_{eo}$)
$v_{eo}(x,y)$	Electroosmotic flow velocity profile.
w_b	Channel width at the bottom (channel floor).
w_t	Width of the channel at the top (lamination).
$[x]$	Concentration: particles of species x , per volume.
X	Recovery ratio of the stretched polymer after annealing.
ζ_s	Zeta-potential of the substrate.

ζ_l Zeta-potential of the lamination.

D.2 Abbreviations (alphabetical order)

AFM	Atomic Force Microscopy
APD	Ablative Photo Decomposition
ATR-IR	Attenuated Total Reflection Infrared Spectroscopy
ESCA	Electron Spectroscopy for Chemical Analysis
ESEM	Environmental Scanning Electron Microscopy
FFT	Fast Fourier Transform
IR	Infrared
LIF	Laser Induced Fluorescence
LIPSS	Laser-Induced Periodic Surface Structures
μ -TAS	Micro-Total Analyzing System
PE	Poly (ethylene)
PEI	Poly (ether imide)
PEN	Poly (ethylene naphthalate)
PET	Poly (ethylene terephthalate)
PI	Poly (imide)
PLD	Pulsed Laser Deposition
PMMA	Poly (methyl methacrylate)
PP	Poly (propylene)
PS	Poly (styrene)
SEM	Scanning Electron Microscopy
TEM	Transmission Electron Microscopy
TOF-MS	Time of Flight Mass Spectrometry
UV	Ultraviolet
XPS	X-ray Photoelectron Spectroscopy

Bibliography

- [1] Y. Kawamura, K. Toyoda and S. Namba, *Effective deep ultraviolet photoetching of polymethyl methacrylate by an excimer laser*, Applied Physics Letters, **40**, (1982), 374-375.
- [2] R. Srinivasan and V. Mayne-Banton, *Self-developing photoetching of poly(ethylene terephthalate) films by far-ultraviolet excimer laser radiation*, Applied Physics Letters, **41**, (1982), 576-578.
- [3] M. A. Roberts, J. S. Rossier, P. Bercier and H. Girault, *UV Laser Machined Polymer Substrates for the Development of Microdiagnostic Systems*, Analytical Chemistry, **69**, (1997), 2035-2042.
- [4] C. S. Effenhauser in *Microsystem technology in chemistry and life science*, edited by A. Manz and H. Becker (Springer, Berlin, 1998), Vol. 194, pp. 51-82.
- [5] J. S. Rossier, P. Bercier, A. Schwarz, S. Loidant and H. H. Girault, *Topography, Crystallinity and Wettability of Photoablated PET surfaces*, Langmuir, **15**, (1999), 5173 - 5178.
- [6] P. D. Grossman in *Capillary Electrophoresis: Theory and Practice*, edited by Paul D. Grossman and Joel C. Colburn (Academic Press, San Diego, 1992), pp. 3-43.
- [7] F. Wagner and P. Hoffmann, *Structure formation in excimer laser ablation of stretched poly(ethylene terephthalate) (PET): the influence of scanning ablation*, Applied Physics A, **69**, (1999), S841-S844.
- [8] F. Wagner and P. Hoffmann, *Novel structure formation in poly(ethylene terephthalate) by scanning excimer laser ablation*, Applied Surface Science, **154-155**, (2000), 627-632.
- [9] F. Wagner and P. Hoffmann, *The angle dependence of structure formation on excimer laser ablated ramps in stretched poly(ethylene terephthalate)*, Applied Surface Science, (2000), accepted.
- [10] F. Wagner and P. Hoffmann, *Electro-osmotic flow control in microchannels produced by scanning excimer laser ablation*, First International Symposium on Laser Precision Microfabrication, Omiya, Japan, (2000), SPIE **4088**, 322-325.
- [11] F. Bianchi, F. Wagner, P. Hoffmann and H. H. Girault, *Electroosmotic flow in composite micro-channels and implication in micro flow injection analysis*, Analytical Chemistry, (2000), submitted.
- [12] F. Wagner and P. Hoffmann, *Zeta potential variations in micro channels produced by scanning excimer laser ablation*, to be published, (2000).
- [13] D. Bäuerle, *Laser processing and chemistry*, 2. ed. (Springer, Berlin, 1996).
- [14] H. Schmidt, J. Ihlemann, B. Wolff-Rottke, K. Luther and J. Troe, *Ultraviolet laser ablation of polymers: spot size, pulse duration, and plume attenuation effects explained.*, Journal of Applied Physics, **83**, (1998), 5458-5468.
- [15] F. C. Burns and S. R. Cain, *The effect of pulse repetition rate on laser ablation of polyimide and polymethylmethacrylate-based polymers*, Journal of Physics D: Applied Physics, **29**, (1996), 1349-1355.
- [16] R. Srinivasan, *Ablation of polymethyl methacrylate films by pulsed (ns) ultraviolet and infrared (9.17 μ) lasers: A comparative study by ultrafast imaging*, Journal of Applied Physics, **73**, (1992), 2743--2750.

- [17] L. V. Zhigilei, P. B. S. Kodali and B. J. Garrison, *A Microscopic View of Laser Ablation*, Journal of Physical Chemistry B, **102**, (1998), 2845-2853.
- [18] P. E. Dyer, G. A. Oldershaw and J. Sidhu, *Ultraviolet-Laser-Induced Ablation of Poly(ethylene terephthalate)*, Journal of Physical Chemistry, **95**, (1991), 10004-10009.
- [19] D. Knittel and E. Schollmeyer, *Surface Structuring of Synthetic Fibres by UV Laser Irradiation. Part III. Surface Functionality Changes Resulting from Excimer-Laser Irradiation*, Polymer International, **45**, (1998), 103-109.
- [20] T. Bahners and E. Schollmeyer, *Oberflächenstrukturierung polymerer Fasern durch UV-Laserbestrahlung 2. Phänomenologische Untersuchung der durch Laserbestrahlung erzeugten Oberflächenstrukturen.*, Angewandte Makromolekulare Chemie, **151**, (1987), 19-37.
- [21] S. Lazare, J. Lopez and F. Weisbuch, *High-aspect-ratio microdrilling in polymeric materials with intense KrF laser radiation*, Applied Physics A, **69**, (1999), S1-S6.
- [22] A. Braun, K. Zimmer and F. Bigl, *Advances in contour and half tone mask laser ablation*, Applied Surface Science, (2000), accepted.
- [23] K. Zimmer, A. Braun and F. Bigl, *Combination of different processing methods for the fabrication of 3D polymer structures by excimer laser machining*, Applied Surface Science, **154**, (2000), 601-604.
- [24] V. N. Tokarev and A. F. H. Kaplan, *Suppression of melt flows in laser ablation: application to clean laser processing*, Journal of Physics D: Applied Physics, **32**, (1999), 1526-1538.
- [25] S. Lazare, P. Benet, M. Bolle, P. De Donato and E. Bernardy, *New surface modifications of polymer films with the excimer laser radiation*, Gas Flow and Chemical Lasers, Crete, Greece, (1992), SPIE **1810**, 546-553.
- [26] H. Watanabe, T. Takata and M. Tsuge, *Polymer Surface Modification due to Excimer Laser Radiation - Chemical and Physical Changes in the Surface Structure of Poly (ethylene terephthalate)*, Polymer International, **31**, (1993), 247-254.
- [27] T. Bahners, D. Knittel, F. Hillenkamp, U. Bahr, C. Benndorf and E. Schollmeyer, *Chemical and physical properties of laser-treated poly(ethyleneterephthalate)*, Journal of Applied Physics, **68**, (1990), 1854-1858.
- [28] S. Lazare and R. Srinivasan, *Surface Properties of Poly (ethylene terephthalate) Films Modified by Far-Ultraviolet Radiation at 193 nm (Laser) and 185 nm (Low intensity)*, Journal of Physical Chemistry, **90**, (1986), 2124-2131.
- [29] M. Chtaib, E. M. Roberfroid, Y. Novis, J. J. Pireaux, R. Caudano, P. Lutgen and G. Feyder, *Polymer surface reactivity enhancement by ultraviolet ArF laser irradiation: An x-ray photoelectron spectroscopy study of polytetrafluoroethylene and polyethyleneterephthalate ultraviolet treated surfaces*, Journal of Vacuum Science and Technology A, **7**, (1989), 3233-3237.
- [30] H. Watanabe and M. Yamamoto, *Laser Ablation of Poly (ethylene terephthalate)*, Journal of Applied Polymer Science, **64**, (1997), 1203-1209.
- [31] R. Srinivasan and S. Lazare, *Modification of polymer surfaces by far-ultraviolet radiation of low and high (laser) intensities*, Polymer, **26**, (1985), 1297-1300.
- [32] S. Lazare, P. D. Hoh, M. Baker and R. Srinivasan, *Controlled Modification of Organic Polymer Surfaces by Continuous Wave Far Ultraviolet (185 nm) and Pulsed Laser*

- (193nm) Radiation: XPS studies, *Journal of the American Chemical Society*, **106**, (1984), 4288-4290.
- [33] T. Lippert, F. Zimmermann and A. Wokaun, *Surface Analysis of Excimer-Laser-Treated Polyethylene-Terephthalate by Surface-Enhanced Raman Scattering and X-Ray Photoelectron Spectroscopy*, *Applied Spectroscopy*, **47**, (1993), 1931-1942.
- [34] F. Kokai, H. Saito and T. Fujioka, *Characterization of Polymer Surfaces after KrF Laser Ablation by Infrared Spectroscopy*, *Macromolecules*, **23**, (1990), 674-676.
- [35] P. W. Hoffmann, M. Stelzle and J. F. Rabolt, *Vapor Phase Self-Assembly of Fluorinated Monolayers on Silicon and Germanium Oxide*, *Langmuir*, **13**, (1997), 1877-1880.
- [36] S. Lazare, V. Granier, P. Lutgen and G. Feyder, *Controlled roughening of poly(ethylene terephthalate) by photoablation: study of wetting and contact angle hysteresis*, *Revue de Physique Appliquée*, **23**, (1988), 1065-1070.
- [37] J. Heitz, E. Arenholz, T. Kefer, D. Bäuerle, H. Hibst and A. Hagemeyer, *Enhanced Adhesion of Metal Films on PET after UV-Laser Treatment.*, *Applied Physics A*, **55**, (1992), 391-392.
- [38] H. Niino and A. Yabe, *Surface modification and metallization of fluorocarbon polymers by excimer laser processing*, *Applied Physics Letters*, **63**, (1993), 3527-3529.
- [39] H. Niino, H. Okano, K. Inui and A. Yabe, *Surface modification of poly(tetrafluoroethylene) by excimer laser processing: enhancement of adhesion*, *Applied Surface Science*, **109/110**, (1997), 259-263.
- [40] H. Niino, A. Yabe, S. Nagano and T. Miki, *Surface morphological microstructures of poly(ethylene 2,6-naphthalate)*, *Applied Physics Letters*, **54**, (1989), 2159-2161.
- [41] T. Lippert, E. Ortelli, J.-C. Panitz, F. Raimondi, J. Wambach, J. Wei and W. A., *Imaging-XPS/Raman investigation on the carbonization of polyimide after irradiation at 308 nm*, *Applied Physics A*, **69**, (1999), S651-S654.
- [42] E. Arenholz, J. Heitz, M. Wagner, D. Bäuerle, H. Hibst and A. Hagemeyer, *Laser-induced surface modification and structure formation of polymers*, *Applied Surface Science*, **69**, (1993), 16-19.
- [43] R. Srinivasan, R. R. Hall, W. D. Wilson, W. D. Loehle and D. C. Allbee, *Ultraviolet laser irradiation of the polyimide, PMDA-ODA (KaptonTM), to yield a patternable, porous, electrically conducting carbon network*, *Synthetic Metals*, **66**, (1994), 301-307.
- [44] M. Strobel, C. S. Lyons, J. M. Strobel and R. S. Kapaun, *Analysis of air-corona-treated polypropylene and poly(ethylene terephthalate) films by contact-angle measurements and X-ray photoelectron spectroscopy*, *Journal of Adhesion Science and Technology*, **6**, (1992), 429-443.
- [45] F. Bianchi, Laboratory of Electrochemistry, Physical Chemistry, Chemistry Department, Swiss Federal Institute of Technology Lausanne, *personal communication*.
- [46] J. E. Andrew, P. E. Dyer, D. Forster and P. H. Key, *Direct etching of polymeric materials using a XeCl laser*, *Applied Physics Letters*, **43**, (1983), 717-719.
- [47] M. Csete and Z. Bor, *Laser-induced periodic surface structure formation on polyethylene-terephthalate*, *Applied Surface Science*, **133**, (1998), 5-16.
- [48] P. E. Dyer and R. J. Farley, *Periodic surface structures in the excimer laser ablative etching of polymers*, *Applied Physics Letters*, **57**, (1990), 765-767.

- [49] J. Heitz, E. Arenholz, D. Bäuerle, R. Sauerbrey and H. M. Phillips, *Femtosecond excimer-laser-induced structure formation on polymers*, Applied Physics A, **59**, (1994), 289-293.
- [50] J. Heitz, E. Arenholz, D. Bäuerle, H. Hibst, A. Hagemeyer and G. Cox, *Dendritic Surface Structures on Excimer-Laser Irradiated PET Foils*, Applied Physics A, **56**, (1993), 329-333.
- [51] J. Heitz, E. Arenholz, D. Bäuerle and K. Schilcher, *Growth of excimer-laser-induced dendritic surface structures on PET*, Applied Surface Science, **81**, (1994), 103-106.
- [52] S. Klose, E. Arenholz, H. J. and D. Bäuerle, *Laser-induced dendritic structures on PET (polyethylene terephthalate): the importance of redeposited ablation products*, Applied Physics A, **69**, (1999), S487-S490.
- [53] R. S. Taylor, K. E. Leopold, D. L. Singleton, G. Paraskevopoulos and R. S. Irwin, *The effect of debris formation on the morphology of excimer laser ablated polymers*, Journal of Applied Physics, **64**, (1988), 2815-2818.
- [54] P. E. Dyer, S. D. Jenkins and J. Sidhu, *Development and origin of conical structures on XeCl laser ablated polyimide*, Applied Physics Letters, **49**, (1986), 453-455.
- [55] T. Bahnert, W. Kesting and E. Schollmeyer, *Controlled structuring of polymer surfaces by uv-laser irradiation*, Excimer Lasers and Applications III, The Hague, Netherlands, (1991), SPIE **1503**, 206-214.
- [56] E. Arenholz, V. Svorcik, T. Kefer, J. Heitz and D. Bäuerle, *Structure Formation in UV-laser Ablated Poly-Ethylene-Terephthalate (PET)*, Applied Physics A, **53**, (1991), 330-331.
- [57] T. Bahnert, W. Kesting and E. Schollmeyer, *Designing surface properties of textile fibers by UV-laser irradiation*, Applied Surface Science, **69**, (1993), 12-15.
- [58] B. Hopp, M. Csete, K. Révész, J. Vinko and Z. Bor, *Formation of the surface structure of polyethylene terephthalate (PET) due to ArF excimer laser ablation*, Applied Surface Science, **96-98**, (1996), 611-616.
- [59] E. Arenholz, J. Heitz, V. Svorcik and D. Bäuerle in *Excimer Lasers*, edited by L. D. Laude (Kluwer Academic Publishers, 1994), pp. 237-243.
- [60] E. Arenholz, M. Wagner, J. Heitz and D. Bäuerle, *Structure Formation in UV-Laser-Ablated Polyimide Foils*, Applied Physics A, **55**, (1992), 119-120.
- [61] V. I. Emel'yanov and K. I. Eriomin, *The Formation of Periodic Structures under Pulsed UV-Laser Ablation of Stretched Polymers*, High-Power Laser Ablation, Santa Fe, New Mexico, (1998), SPIE **3343**, 1056-1067.
- [62] S. Lazare, P. Benet, W. Guan, M. Bolle and S. Mihailov in *Excimer Lasers*, edited by L. D. Laude (Kluwer Academic Publishers, 1994), pp. 201-219.
- [63] A. Brezini, *Surface Properties of Polyethylene Terephthalate Films Modified by Far UV Radiation at 193 nm.*, physica statua solidi A, **135**, (1993), 589-596.
- [64] Y. Novis, J. J. Pireaux, A. Brezini, E. Petit, R. Caudano, P. Lutgen, G. Feyder and S. Lazare, *Structural origin of surface morphological modifications developed on poly(ethylene terephthalate) by excimer laser photoablation*, Journal of Applied Physics, **64**, (1988), 365 - 370.
- [65] W. Kesting, D. Knittel, T. Bahnert and E. Schollmeyer, *Oberflächenstrukturierung von Hochleistungsfasern*, Angewandte Makromolekulare Chemie, **196**, (1992), 179-194.

- [66] T. Bahners and E. Schollmeyer, *Morphological changes of the surface structure of polymers due to excimer laser radiation: A synergetic effect?*, Journal of Applied Physics, **66**, (1989), 1884-1886.
- [67] V. I. Emel'yanov, *Self-organisation of ordered defect - deformation microstructures and nanostructures on the surfaces of solids under the action of laser radiation*, Quantum Electronics, **29**, (1999), 561-577.
- [68] M. Himmelbauer, E. Arenholz, D. Bäuerle and K. Schilcher, *UV-Laser-induced surface topology changes in polyimide*, Applied Physics A, **63**, (1996), 337-339.
- [69] F. Sánchez, J. L. Morenza and V. Trtik, *Characterization of the progressive growth of columns by excimer laser irradiation of silicon*, Applied Physics Letters, **75**, (1999), 3303 - 3305.
- [70] T.-H. Her, R. J. Finlay, C. Wu, S. Deliwala and E. Mazur, *Microstructuring of silicon with femtosecond laser pulses*, Applied Physics Letters, **73**, (1998), 1673 - 1675.
- [71] P. E. Dyer and J. Sidhu, *Spectroscopic and fast photographic studies of excimer laser polymer ablation*, Journal of Applied Physics, **64**, (1988), 4657-4663.
- [72] D. L. Singleton, G. Paraskevopoulos and R. S. Irwin, *XeCl laser ablation of polyimide: Influence of ambient atmosphere on particulate and gaseous products*, Journal of Applied Physics, **66**, (1989), 3324-3328.
- [73] R. Srinivasan, B. Braren and R. W. Dreyfus, *Ultraviolet laser ablation of polyimide films*, Journal of Applied Physics, **61**, (1987), 372-376.
- [74] S. Lazare and V. Granier, *Ultraviolet laser ablation of polymers: Yield and spatial distribution of products deposition*, Chemical Physics Letters, **168**, (1990), 593-597.
- [75] A. Mele, A. Giardani Guidoni, R. Kelly, A. Miotello, S. Orlando and R. Teghil, *Spatial distribution of laser-ablated material by probing a plasma plume in three dimensions*, Applied Surface Science, **96-98**, (1996), 102-111.
- [76] A. Mele, A. Giardini Guidoni, R. Kelly, A. Miotello, S. Orlando, R. Teghil and C. Flamini, *Angular distribution and expansion of laser ablation plumes measured by fast intensified charge coupled device photographs*, Nuclear Instruments and Methods in Physics Research B, **116**, (1996), 257-261.
- [77] S. G. Hansen, *Velocity profiles of species ejected in UV laser ablation of several polymers examined by time-of-flight mass spectroscopy*, Journal of Applied Physics, **66**, (1989), 3329-3336.
- [78] L. V. Zhigilei and B. J. Garrison, *Velocity distributions of molecules ejected in laser ablation*, Applied Physics Letters, **71**, (1997), 551-553.
- [79] Z. Bor, B. Hopp, Z. Marton, Z. Gogolak and F. Ignacz, *Ultrafast photography of shock waves originating from UV photoablated surface*, Optics as a Key to High Technology, (1993), SPIE **1983**, 748-750.
- [80] H. Callies, P. Berger and H. Hügel, *Time-resolved observation of gas-dynamic discontinuities arising during excimer laser ablation and their interpretation*, Journal of Physics D: Applied Physics, **28**, (1995), 794-806.
- [81] S. Küper and J. Brannon, *Ambient gas effects on debris formed during KrF laser ablation of PI*, Applied Physics Letters, **60**, (1992), 1633-1635.

- [82] R. Kelly, A. Miotello, B. Braren and C. E. Otis, *On the debris phenomenon with laser-sputtered polymers*, Applied Physics Letters, **60**, (1992), 2980-2982.
- [83] G. Koren and U. P. Oppenheim, *Laser Ablation of Polymers in Pressurized Gas Ambients*, Applied Physics B, **42**, (1986), 41-43.
- [84] R. Kelly and A. Miotello, *Laser-pulse sputtering of atoms and molecules Part II. Recondensation effects*, Nuclear Instruments and Methods in Physics Research B, **91**, (1994), 682-691.
- [85] A. Miotello, R. Kelly, B. Braren and C. E. Otis, *Novel geometrical effects observed in debris when polymers are laser sputtered*, Applied Physics Letters, **61**, (1992), 2784-2786.
- [86] S. Küper and J. Brannon, *KrF-Laser Ablation of Polyurethane*, Applied Physics A, **57**, (1993), 255-259.
- [87] H. Hiraoka and S. Lazare, *Surface modifications of Kapton and cured polyimide films by ArF excimer laser: applications to imagewise wetting and metallization*, Applied Surface Science, **46**, (1990), 264-271.
- [88] G. Koren and J. J. Donelon, *CO₂ Laser Cleaning of Black Deposits Formed During the Excimer Laser Etching of Polyimide in Air*, Applied Physics B, **45**, (1987), 45-46.
- [89] R. J. von Gutfeld and R. Srinivasan, *Electrostatic collection of debris resulting from 193 nm laser etching of polyimide*, Applied Physics Letters, **51**, (1987), 15-17.
- [90] J. S. Rossier and H. H. Griault, *Nanocrystalline carbon film electrodes generated and patterned by UV-laser ablation of polystyrene*, Physical Chemistry Chemical Physics, **1**, (1999), 3647-3652.
- [91] H. Niino and A. Yabe, *Positively charged surface potential of polymer films after excimer laser ablation: Application to selective-area electroless plating on the ablated films*, Applied Physics Letters, **60**, (1992), 2697-2699.
- [92] H. Niino and A. Yabe, *Excimer laser polymer ablation: formation of positively charged surfaces and its application into the metallization of polymer films*, Applied Surface Science, **69**, (1993), 1-6.
- [93] G. Beamson and D. Briggs, *High resolution XPS of organic polymers* (Wiley, Chichester, 1992).
- [94] H. Watanabe and M. Yamamoto, *Chemical Structure Change of a KrF-Laser Irradiated PET fiber surface*, Journal of Applied Polymer Science, **71**, (1999), 2027-2031.
- [95] A. Schwarz, *New protein separation and analysis techniques*, PhD-thesis No. 2225, Swiss Federal Institute of Technology Lausanne, 2000.
- [96] C. Gerthsen, H. O. Kneser and H. Vogel, *Physik*, 16 ed. (Springer, Berlin, 1989).
- [97] P. G. de Gennes, *Wetting: statics and dynamics*, Reviews of Modern Physics, **57**, (1985), 827-863.
- [98] W. A. Zisman in *Contact Angle, Wettability, and Adhesion*, edited by Frederick M. Fowkes (American Chemical Society, Washington D.C., 1964), Vol. 43, pp. 1-51.
- [99] F. M. Fowkes in *Contact Angle, Wettability, and Adhesion*, edited by Frederick M. Fowkes (American Chemical Society, Washington D.C., 1964), Vol. 43, pp. 99-111.

- [100] R. E. Johnson and R. H. Dettre in *Contact Angle, Wettability, and Adhesion*, edited by Frederick M. Fowkes (American Chemical Society, Washington D.C., 1964), Vol. 43, pp. 112-135.
- [101] F. M. Fowkes, *Contact Angle, Wettability, and Adhesion* (American Chemical Society, Washington D.C., 1964).
- [102] R. H. Dettre and R. E. Johnson in *Contact Angle, Wettability, and Adhesion*, edited by Frederick M. Fowkes (American Chemical Society, Washington D.C., 1964), Vol. 43, pp. 136-144.
- [103] W. Chen, A. Y. Fadeev, M. C. Hsieh, D. Oener, J. Youngblood and T. J. McCarthy, *Ultrahydrophobic and Ultralyophobic Surfaces: Some Comments and Examples*, *Langmuir*, **15**, (1999), 3395 - 3399.
- [104] C. H. Hamann and W. Vielstich, *Elektrochemie I* (VCH, Weinheim, 1985).
- [105] F. Hinze, S. Ripperger and M. Stintz, *Praxisrelevante Zetapotentialmessung mit unterschiedlichen Messtechniken*, *Chemie Ingenieur Technik*, **71**, (1999), 338 - 347.
- [106] V. P. Andreev, S. G. Dubrovsky and Y. V. Stepanov, *Mathematical Modeling of Capillary Electrophoresis in Rectangular Channels*, *Journal of Microcolumn Separations*, **9**, (1997), 443 - 450.
- [107] P. D. Grossman and J. C. Colburn, *Capillary Electrophoresis: Theory and Practice* (Academic Press, San Diego, 1992).
- [108] D. J. Harrison, K. Fluri, K. Seiler, Z. Fan, C. S. Effenhauser and A. Manz, *Micromachining a Miniaturized Capillary Electrophoresis-Based Chemical Analysis System on a Chip*, *Science*, **261**, (1993), 895-897.
- [109] J. S. Rossier, M. A. Roberts, R. Ferrigno and H. H. Girault, *Electrochemical Detection in Polymer Microchannels*, *Analytical Chemistry*, **71**, (1999), 4294-4299.
- [110] A. E. Herr, J. I. Molho, J. G. Santiago, M. G. Mungal and T. W. Kenny, *Electroosmotic Capillary Flow with Nonuniform Zeta Potential*, *Analytical Chemistry*, **72**, (2000), 1053-1057.
- [111] T. Sidler, Institute of Applied Optics, Micro-Engineering Department, Swiss Federal Institute of Technology Lausanne, *personal communication*.
- [112] M. C. Gower, *Excimer laser microfabrication and micromachining*, Laser Precision Microfabrication, Omiya, Japan, (2000), SPIE in press.
- [113] "MELINEX polyester film, Film type: S", (DuPont (UK) Limited,).
- [114] T. Pakula and E. W. Fischer, *Instabilities of the Deformation Process in Cold Drawing of Poly(ethylene Terephthalate) and Other Polymers*, *Journal of Polymer Science: Polymer Physics Edition*, **19**, (1981), 1705-1726.
- [115] S. V. Vlasov and V. N. Kuleznev, *Some Relationships for the Orientational Drawing of Polymers*, *Polymer Engineering and Science*, **35**, (1995), 173 - 179.
- [116] R. Roseen, *Temperature effect at self-oscillating necking during extension of polyethylene terephthalate (PETP)*, *Journal of Materials Science*, **9**, (1974), 929 - 933.
- [117] C. L. Chang, W. Y. Chiu, K. H. Hsieh and C.-C. M. Ma, *The Molecular Orientation and Mechanical Properties of Poly(ethylene terephthalate) Under Uniaxial Extension*, *Journal of Applied Polymer Science*, **50**, (1993), 855-862.

BIBLIOGRAPHY

- [118] X. Huang, M. J. Gordon and R. N. Zare, *Current-Monitoring Method for Measuring the Electroosmotic Flow Rate in Capillary Zone Electrophoresis*, *Analytical Chemistry*, **60**, (1988), 1837-1838.
- [119] J. L. Halary, Laboratoire de Physicochimie Structurale et Macromoléculaire (UMR 7615), ESPCI, Paris, *personal communication*.
- [120] G. Kämpf, *Geordnete Ueberstrukturen in ein- und mehrphasigen amorphen Hochpolymeren*, *Progress in Colloid and Polymer Science*, **57**, (1975), 249-261.
- [121] H. J. Mathieu, Laboratory of Metallurgical Chemistry, Materials Science and Engineering Department, Swiss Federal Institute of Technology Lausanne, *personal communication*.
- [122] W. Chen and T. J. McCarthy, *Chemical Surface Modification of Poly(ethylene terephthalate)*, *Macromolecules*, **31**, (1998), 3648-3655.

Acknowledgements, Remerciements, Danksagung

Mein Dank geht zuallererst an Patrik Hoffmann, meinen “Doktorvater”, der mir die Möglichkeit zur Durchführung dieser Arbeit gegeben hat. Für die Freiheit, die er mir gelassen hat, seine Verfügbarkeit für Diskussionen, und auch die praktischen Ratschläge. Für seine wissenschaftlichen und menschlichen Qualitäten, die in den letzten drei Jahren wichtig für mich waren. Ich habe den Eindruck alle Aktivitäten, die mich an einer Dissertation gereizt hatten, ausprobiert zu haben, und dabei einiges gelernt zu haben.

Un grand merci ensuite à tous ceux qui ont collaboré d’une manière ou d’une autre à ce projet:

- Au Laboratoire d’Electrochimie: François Bianchi, avec qui les derniers mois de travail ont conduit à une collaboration très fructueuse. Alexandra Schwarz, pour les discussions intéressantes, et pour l’introduction à l’électrosmose qu’elle m’a donnée avec Joël Rossier au début de ma thèse lors de nos rencontres hebdomadaires.
- Au département de Matériaux: Nicolas Xantopoulos et H. J. Mathieu pour les analyses XPS, Chris Plumer pour les analyses TEM. Sans eux, des données essentielles m’auraient manqué dans ce travail.
- Au centre Interdépartementale de Microscopie Electronique: Brian Senior, M. Buffat, François Cléton et Jalil Sayah (IMS), qui m’ont appris et permis d’utiliser le SEM, ainsi que l’équipe qui a organisé la visite à l’EMPA.
- L’équipe de Micro-Usinage Laser pour toutes les découpes de masques: Sebastian Favre, Lucas Mumentaler, Antonio Lopez, Simon Benjamin.
- Pour les mesures AFM, Benjamin Dwir (Institut de Micro et Opto Electronique) pour les premiers essais, et Gerit Jänchen pour les mesures de débris.
- Pour les fabrications d’échantillons de PET avec des stress différents: Sandrine Mariot et Jean-Louis Halary (Laboratoire de Physico-Chimie Structurale et Macromoléculaire à l’ESPCI, Paris), ainsi que Michel Studer du (Laboratoire de Mécanique Appliquée et d’Analyse de Fiabilité).
- Sans oublier l’EPFL pour son financement...

Mes remerciements vont aussi à ceux qui m’ont aidé avec les “difficultés techniques”:

- Pour tout le service avec les ordinateurs: Claude Philipona et Philippe Giaccari pour leur aide.
- L’atelier mécanique du DMT, particulièrement Claude Amendola.
- Pour l’électronique: Ronald Gianotti pour ses conseils.
- Au Laboratoire d’Electrochimie: Valérie Devaud et M. Bercier.
- Le secrétariat de l’IOA, pour la gestion des difficultés administratives.

Je voudrais aussi remercier les étudiants et stagiaires qui sont venus travailler avec moi:

Tristan Bret, Phouong Quyen Pham et Natascha Lindenmeyer. Des collaborations intéressantes et très sympathiques.

Un grand merci aux collaborateurs de l’IOA, actuels ou passés, pour l’ambiance de travail chaleureuse, les discussions intéressantes et les bons moments passés ensemble. En particulier, Anne Isabelle, Didier, Klaus, Laurent, Mustapha, Pia, Sebastian, Taisuke, Thomas Sidler, ...

Je n’oublierai pas bien sur mes collègues de bureau, Fabio et Giacomo... et tout le reste du groupe MAD, pour son ambiance très amicale.

Vielen Dank auch meiner Familie, auf deren vielfältige Unterstützung ich immer zählen kann.

Und auch Peter Simon vom LLG möchte ich hier nochmal danken für die Geduld, die er während meiner Diplom-Arbeit mit mir gehabt hat.

Et évidemment un grand, grand merci à la personne qui a dû le plus souffrir pendant les mois de rédaction, et qui m’a soutenu avec toute son énergie: Estelle. Ainsi qu’à Léa, le bébé le plus chouette du monde!

ACKNOWLEDGEMENTS

Curriculum Vitae

Frank Rüdiger WAGNER

Born in Saarbrücken (Germany), on August 19th 1970
German nationality
Married

Education

- | | |
|---------------------------------|---|
| April 28 th 1989 | High School Graduation Diploma: “Abitur”
(Otto-Hahn-Gymnasium, Böblingen, Germany) |
| June 1989 -
August 1990 | Compulsory military service |
| September 1990 -
July 1993 | First Part of University Studies in Physics
(Georg-August-University, Göttingen, Germany) |
| August 1993 -
July 1994 | High School Teacher (Peace Corps)
(Efok, Cameroun) |
| August 1994 -
June 1995 | Second Part of University Studies: Specialization in Optics and Physical Chemistry
(Georg-August-University, Göttingen, Germany) |
| June 1995 -
December 1996 | Diploma Thesis: “Generation of tunable femto-second-pulses with a GVD-compensated OPA”
(Laser Laboratorium Gottingen e.V., Germany) |
| March 1997 -
May 1997 | Scientific Collaborator
(Laser Laboratorium Gottingen e.V., Germany) |
| August 1997 -
September 2000 | Assistant - PhD student
(Institute of Applied Optics, Swiss Federal Institute of Technology, Lausanne, Switzerland) |

Publications

- [1] F. Wagner, M. Feuerhake and P. Simon, *Group-velocity-dispersion-compensated femtosecond optical parametric amplifier*, *Optical and Quantum Electronics*, **29**, (1997), 811-818.
- [2] F. Wagner and P. Hoffmann, *Novel structure formation in poly(ethylene terephthalate) by scanning excimer laser ablation*, *Applied Surface Science*, **154-155**, (2000), 627-632.
- [3] E. Halary, G. Benvenuti, F. Wagner and P. Hoffmann, *Light induced chemical vapour deposition of titanium oxide thin films at room temperature*, *Applied Surface Science*, **154-155**, (2000), 146-151.
- [4] F. Wagner and P. Hoffmann, *Structure formation in excimer laser ablation of stretched poly(ethylene terephthalate) (PET): the influence of scanning ablation*, *Applied Physics A*, **69**, (1999), S841-S844.
- [5] F. Wagner and P. Hoffmann, *The angle dependence of structure formation on excimer laser ablated ramps in stretched poly(ethylene terephthalate)*, *Applied Surface Science*, (2000), in press.
- [6] F. Wagner and P. Hoffmann, *Electroosmotic Flow Control in Micro Channels Produced by Scanning Excimer Laser Ablation*, *Laser Precision Microfabrication*, Omiya, Japan, (2000), SPIE in press.
- [7] F. Bianchi, F. Wagner, P. Hoffmann and H. H. Girault, *Electroosmotic flow in composite micro-channels and implication in micro flow injection analysis*, *Analytical Chemistry*, (2000), submitted.
- [8] F. Wagner and P. Hoffmann, *Zeta potential variations in micro channels produced by scanning excimer laser ablation*, to be published, (2000).

Participations to Conferences

- [1] F. Wagner and P. Hoffmann, “Tailoring of wetting properties of microchannels in poly(ethylene terephthalate) PET by scanning uv excimer laser ablation”, *14th conference of the SAOG*, oral contribution, (Fribourg, Switzerland, 1998).
- [2] F. Wagner and P. Hoffmann, “Novel structure formation in poly(ethylene therephthalate) (PET) by scanning excimer laser ablation”, *E-MRS spring meeting*, oral contribution, (Strasbourg, France, 1999).
- [3] F. Wagner and P. Hoffmann, “Structure formation in excimer laser ablation of stretched poly(ethylene therephthalate) (PET): the influence of scanning ablation”, *COLA*, poster, (Göttingen, Germany, 1999).
- [4] F. Wagner and P. Hoffmann, “Electroosmotic flow control in micro channels produced by scanning excimer laser ablation”, in *16th conference of the SAOG*, oral contribution, (Fribourg, Switzerland, 2000).
- [5] F. Wagner and P. Hoffmann, “The angle dependence of structure formation on excimer laser ablated ramps in stretched poly(ethylene terephthalate)”, *E-MRS spring meeting*, oral contribution, (Strasbourg, France, 2000).
- [6] F. Wagner and P. Hoffmann, “Electroosmotic Flow Control in Micro Channels Produced by Scanning Excimer Laser Ablation”, *LPM 2000 (The First International Symposium on Laser Precision Microfabrication)*, oral contribution, (Omiya, Japan, 2000).